Institut für Energiewirtschaft und Anwendungstechnik
Technische Universität München

Characterizing Spatial Conditions Within A Hydrogen and Direct Methanol Polymer Electrolyte Fuel Cell Using The Segmented Electrode Approach

Guido Bender

Vollständiger Abdruck der von der Fakultät für Elektrotechnik und Informationstechnik der Technischen Universität München zur Erlangung des akademischen Grades eines

Doktor-Ingenieurs (Dr.-Ing.)

genehmigten Dissertation.

Vorsitzender: Univ.-Prof. Dr.-Ing. Fernando Puente León

Prüfer der Dissertation:

1. Univ.-Prof. Dr.-Ing. Ulrich Wagner
2. Univ.-Prof. Dr. rer. nat. Ulrich Stimming

Die Dissertation wurde am 21.06.2005 bei der Technischen Universität München eingereicht und durch die Fakultät für Elektrotechnik und Informationstechnik am 05.04.2006 angenommen.

Table of Contents

Table of Figures

Table of Tables

Symbols and Abbreviations

Symbols

a	Material Parameter
A	Cross Sectional Area
b	Tafel Slope
b_{fc}	Reciprocal Adsorption for Carbon Monoxide
b_{fh}	Reciprocal Adsorption for Hydrogen
C	Concentration
C_B	Bulk Concentration
C_S	Surface Concentration
D	Diffusion Coefficient
d	Thickness
D_h	Hydraulic Diameter
E	Electrode Potential
E_o	Reversible Cell Voltage
E_{oc}	Open Circuit Voltage
$f_{in,anode}$	Anode Inlet Flux
i	Current Density
i_L	Limiting Current Density
i_o	Exchange Current Density
k_{fc}	Rate Constant for Carbon Monoxide Adsorption
k_{fh}	Rate Constant for Hydrogen Adsorption
n_e	Number of Exchanged Electrons
$n_{Ptsites}$	Amount of Active Platinum Catalyst Sites
P_A	Total Anode Pressure
P_{CO}	Partial Pressure of Carbon Monoxide
P_h	Partial Pressure of Hydrogen
Q_{CO}	CO Stripping Charge
R	Resistance
R_{electr}	Electronic Resistance
$R_{membrane}$	Protonic Membrane Resistance
R_s	Serial Resistance
$R_{\square}$	Membrane Resistance Independent of Membrane Area
T	Temperature
t	Time
v	Scan Rate
V_{Cell}	Cell Voltage

X_{CO}	Mole Fraction of Carbon Monoxide
X_h	Mole Fraction of Hydrogen
α	Electron Transfer Coefficient
ΔE	Potential Difference
η_{act}	Activation Polarization
η_{conc}	Concentration Polarization
η_{oc}	Open Circuit Polarization
η_{xover}	Overpotential by Methanol Crossover
η_{Ω}	Ohmic Polarization
Θ_{CO}	Fractional Coverage by Carbon Monoxide
Θ_h	Fractional Coverage by Hydrogen
λ	Stoichiometric Flow Rate
μ	Viscosity
ρ_{fl}	Fluid Density
ρ	Resistivity
ρ_{Pt}	Molar Area Density of Catalyst Sites times the Faraday Constant

Abbreviations

AFC	Alkaline Fuel Cell
CFD	Computational Fluid Dynamics
CL	Catalyst Layer
CV	Cyclic Voltammetry
DMFC	Direct Methanol Fuel Cell
FC	Fuel cell
FRA	Frequency Response Analyzer
G-III	Generation Three
G-IV	Generation Four
GC	Gas Chromatography
GDL	Gas Diffusion Layers
HFR	High Frequency Resistance
LANL	Los Alamos National Laboratory
MCFC	Molten Carbonate Fuel Cell
MEA	Membrane Electrode Assembly
MeOH	Methanol
ORR	Oxygen Reduction Reaction
PAFC	Phosphoric Acid Fuel Cell
PBI	Polybenzimidazole
PCB	Printed Circuit Board
PEEK	Poly Ether Ether Ketones
PEFC	Polymer Electrolyte Fuel Cell
PEMFC	Proton Exchange Membrane Fuel Cell
PES	Poly Ether Sulfones
PPZ	Poly Phosphazene
SOFC	Solid Oxide Fuel Cell
TBA	Tetrabutylammonium
TBA-OH	Tetrabutylammonium Hydroxide
XRMF	X-ray microfluorescence spectroscopy

Chemical Symbols

C	Carbon
CH_3OH	Methanol
CO_3^{2-}	Carbonate
CO	Carbon Monoxide
CO_2	Carbon Dioxide
e^-	Electron
H	Hydrogen
H^+	Proton
H_2O	Water
N	Nitrogen
O	Oxygen
OH^-	Hydroxide
TBA	Tetrabutylammonium

Constants

F	Faraday Constant
R	General Gas Constant

Abstract

This thesis was performed to study spatial effects in hydrogen and methanol powered fuel cells that employ solid polymer electrolyte membranes. Diagnostic tools were a generation three (G-III) and a, during the course of this work, redesigned and continuously refined generation four (G-IV) segmented cell system. The segmented cell system allowed spatial resolution of standard fuel cell measurements, such as polarization curves, high frequency resistance, cyclic voltammetry, transients, life tests, AC spectroscopy, fuel crossover measurements, and anode polarization. It was found to be an effective tool for investigating spatial and temporal effects on PEFC and DMFC operation.

The first part of this work gave exceptional insight into the time and space distribution of surface CO and its impact on PEFC performance. Studies focused on non-steady-state states of the fuel cell due to exposure to CO, the time-dependent distribution of the CO in the segmented anode, and anode recovery processes. It was found that initial catalyst poisoning and saturation of the catalyst layer with CO occurs first at catalyst areas closest to the anode inlet. CO adsorption continuously progresses along the flow-field as a function of exposure time and operating conditions. At standard operating conditions 80-85% of an entire monolayer of CO was completed on the accessible platinum surface. Recovery from CO exposure was the fastest and most complete for the inlet segment. It became gradually slower and less complete for the segments located further down the anode flow field. The cell was capable of recovering up to 95% of the initial current once the flow of pure hydrogen was regained. Comparison of the experimental data to a model gained additional insight into processes occurring during cell exposure to CO.

The second part of the work effectively demonstrated the ability of the segmented cell approach to investigate the effects of critical direct methanol fuel cell (DMFC) parameters such as methanol concentration, cathode humidification, and anode and cathode flow rates on performance. The data suggested the existence of a trade-off between flooding and drying processes in DMFCs that requires a carefully balanced water management to achieve maximum performance. Also, a transition between methanol crossover and mass transport effects as the dominant loss mechanism in the DMFC was observed with increasing current density. This transition changes as a function of methanol concentration. To optimize DMFC operating conditions, the typical operation of the system and its typical operation point is a key parameter.

The results presented led to a deeper fundamental understanding of fuel cell systems and demonstrate the utility of a segmented cell as a research tool.

1 Fundamentals

Fuel cells (FCs) are electrochemical devices that convert the chemical energy of a fuel directly into electrical energy. A fuel cell may be described as a battery to which the reactants are continuously fed and reaction products removed. The fuel cell is therefore able to maintain continuous operation as long as the fuel and oxidant are supplied to the electrodes. In reality, degradation (primarily corrosion) or malfunction of components limits the practical operating life of fuel cells.

The interest of scientists in fuel cells dates back to C. F. Schoenbein, who in 1838 discovered the so called “fuel cell effect” and to Sir W. R. Grove, who in 1939 developed the gas battery, as he called the first fuel cell [1]. Later on W. Oswald provided the basic thermodynamic equations showing the definite advantages of ‘Low Temperature Electrochemical Oxidation’ over ‘High Temperature Combustion’ of fuels [2]. Nonetheless over 100 years passed since the discovery before F.T. Bacon’s prototype of an alkaline fuel cell system became the first major application with its employment by the NASA Apollo and Gemini space programs in the 1960’s to produce water and electrical energy on board [3], [4]. At the same time fuel cells were first introduced to vehicle propulsion since their efficiency is not limited by the Carnot Cycle that constrains combustion engines [5]. In 1959 W. Mitchell built the Allis Chalmers fuel cell powered tractor, Varta AG and Siemens AG presented a fuel cell driven motorboat, GM equipped a six passenger “Electrovan” with a UCC fuel cell in 1967, and in the 1970’s, a fuel cell passenger car was built by Kordesch combining a lead-acid battery with an alkaline fuel cell system [6].

With thermal co-generation very high efficiencies can be obtained with fuel cells [6]. Thus fuel cells constitute an attractive alternative for energy conversion, in addition to very low noise and gas emissions. Due to their modular construction fuel cells have high efficiencies even for small units and can be applied in a wide power range from W to MW [7], [8]. As a result of this versatility, fuel cell projects focus on applications in cell phones, and automobiles as well as in power plants.

Today, only a few commercial fuel cell products are sold. For example a well established 200 kW stationary power plant implementing a phosphoric acid fuel cell (PAFC) is sold by ONSI/UTC. All major car companies have significant research efforts in polymer electrolyte fuel cells (PEFCs). Though announcements for upcoming production of PEFC powered cars have been made, the appearance of PEFC in small portable power applications is more likely to occur first. Current progress in PEFC research has resulted in just a few PEFCs that are currently commercially available. Nuvera / DeNora, for example, offers 1 – 6 kW PEFC stacks, and Ballard sells PEFC stacks that deliver up to 1.2 kW electrical power. Ballard also offers a portable PEFC unit of the same output which serves as an uninterruptible power supply. The lack of PEFC products on the market shows the need for further PEFC research and development.

1.1 Fuel Cell Types

Fuel cells not only exhibit wide power ranges, they also cover a wide range of fuels, electrolytes, and operating temperatures. The most common classification of fuel cells is by the type of electrolyte employed in the cells [8]-[11]. The resulting fuel cell types, their operating temperatures, and their electrolytes are listed in **Table 1**.

A liquid electrolyte is used in the Alkaline Fuel Cell (AFC). The OH^- conductive AFC electrolyte consists of 30% - 85% potash lye; the concentration depends on the operating temperature, which varies between 60 - 230°C. Another fuel cell with a liquid electrolyte is the Phosphoric Acid Fuel Cell (PAFC). This acid fuel cell contains concentrated proton conductive phosphoric acid. It operates at temperatures around 200 °C. Possible fuels of the PAFC are hydrogen, reformed natural gas or other reformed hydrocarbons.

Table 1: Fuel Cell Types

FC Type	abbr.	Cell Temp.	Mobile Ion	Electrolyte
Alkaline FC	AFC	60-230°C	OH^-	30%-85% Potash Lye (KOH)
Polymer Electrolyte FC	PEFC	50-80°C	H^+	Ion Exchange Membrane (Nafion, Dow)
Direct Methanol FC	DMFC	80-130°C	H^+	Ion Exchange Membrane (Nafion, Dow)
Phosphoric Acid FC	PAFC	150-220°C	H^+	Phosphoric Acid (H_3PO_4)
Molten Carbonate FC	MCFC	620-650°C	CO_3^{2-}	Molten Carbonate (Li_2CO_3, KCO_3)
Solid Oxide FC	SOFC	800-1000°C	O^{2-}	Ceramic (ZrO_2/YO_3)

Proton conductive membranes are used in the Polymer Electrolyte Fuel Cell (PEFC), also identified as Proton Exchange Membrane Fuel Cell (PEMFC). In the literature the term PEFC is typically used for a hydrogen powered fuel cell, while a state of the art methanol (MeOH) powered fuel cell that also employs a solid electrolyte membrane is referred to as Direct Methanol Fuel Cell (DMFC). When well humidified, the solid polymer membrane used in these cells achieves excellent proton conductivity. Unlike the PEFC, which uses hydrogen and oxygen (air) as fuel and oxidant, methanol and oxygen (air) are employed in the DMFC. PEFC and DMFC are very similar, but their fuels require different catalysts and the use of methanol adds further challenges.

Temperatures of about 650 °C are necessary for the Molten Carbonate Fuel Cell (MCFC) to operate. In this environment the carbonate has passed a phase transition and the highly viscous liquid provides ionic conductivity. The electrolyte of this fuel cell type is able to transport CO_3^{2-} ions. In addition to oxygen, carbon dioxide must be used at the cathode to operate the cell. Another fuel cell that operates at high temperatures (up to 1000 °C) is the Solid Oxide Fuel Cell (SOFC). Negatively charged oxygen ions (O^{2-}) are transported through the solid electrolyte from cathode to anode. The SOFC has the highest operating temperatures of all fuel cell types. The MCFC, and SOFC provide the highest efficiencies of all the fuel cell types when the produced electrical energy and the thermal energy are both utilized.

1.2 Polymer Electrolyte Fuel Cell

PEFCs can potentially provide high power density at a reasonably low cost. They operate at low temperatures, allow fast start-ups and quickly respond to changes in the demand for power. Therefore the PEFC system has potential use for transportation and portable applications as well as for smaller stationary power plants [12].

The low operating temperatures of a PEFC result in both advantages and disadvantages. The cell can for example start quickly from ambient conditions, especially when pure hydrogen fuel is available. Unfortunately, expensive platinum catalysts are required to promote the desired electrochemical reaction at these temperatures. Currently, only Pt or Pt-alloy based catalysts are able to sustain both hydrogen oxidation reaction (HOR) and oxygen reduction reaction (ORR) at sufficiently high rates for providing practical electrical power [13].

The following sections introduce the working principle and key structures and components of a PEFC. Furthermore, the main power loss mechanisms will be described and the importance of water management explained.

1.2.1 Working Principle

A schematic representation of a PEFC with the involved chemical components and the ion and electron flow directions is shown in **Figure 1**. The basic cell consists of a proton conducting membrane (white) sandwiched between two platinum impregnated porous electrodes (black) and two electron conductive gas diffusion layers (gray).

The chemical energy is supplied as gaseous hydrogen, which is, by means of oxygen (usually from the air), converted into electrical energy by the system. The reactants are fed to the gas diffusion layers: hydrogen to the anode, oxygen to the cathode. There they diffuse to the electrode, where the reactions take place.

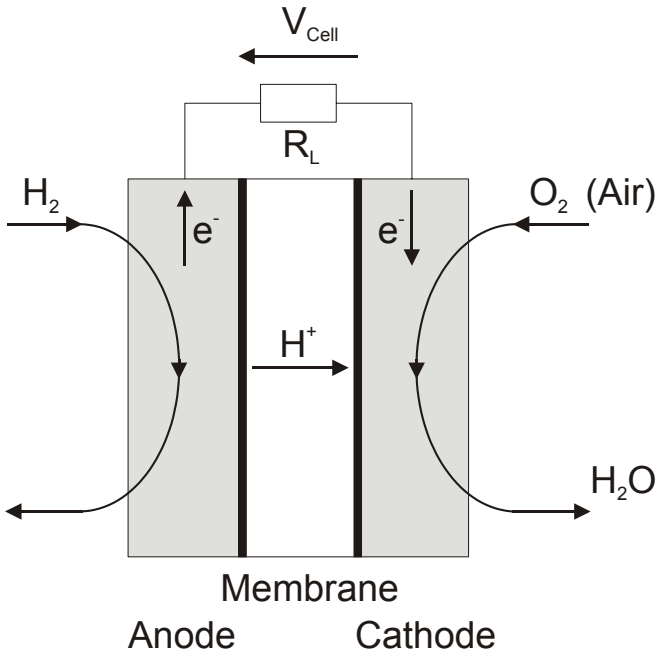

Figure 1: Basic cell and working principle of a PEFC.

The net reaction of a hydrogen (H_2) and oxygen (O_2) powered fuel cell is shown in equation (1). The membrane, by physically separating fuel and oxidant, induces the reactants to proceed through electrochemical independent pathways: the oxidation reaction of H_2 at the anode (HOR) (2) and the reduction reaction of O_2 at the cathode (ORR) (3). This reactant separation facilitates the conversion of the chemical energy of the fuel into exploitable electrical energy. At the anode H_2 dissociates into protons (H^+) and electrons (e^-). The electrons are attracted to the cathode where they complete partial reaction (3). Since the membrane can only conduct cations (e.g. H^+), the electrons are forced to travel through the external electrical circuit and the electrical load to reach the cathode, thus generating an electrical current. The electrical charge is balanced by transport of the protons across the membrane to the cathode. At this electrode they take part in reaction (3) generating water as the only product. The electrical energy produced is obtained at and can be controlled with the electrical load. The process itself is driven by the electrochemical potential difference between partial reactions (2) and (3) that occur at the electrodes of the cell.

PEFC Reaction:

$$2H_2 + O_2 \rightarrow 2H_2O + \text{energy} \quad (1)$$

Anode Reaction:

$$2H_2 \rightarrow 4H^+ + 4e^- \quad (2)$$

Cathode Reaction:

$$4H^+ + 4e^- + O_2 \rightarrow 2H_2O \quad (3)$$

1.2.2 Electrode Structure

The electrodes are key structures of a fuel cell system. In the electrode, electrolyte, catalyst, and fuel or air come in contact with each other and create the reaction zone. An unrestrained reaction requires a couple of preconditions, such as high proton conductivity of the electrolyte, high electron conductivity, and well functioning reactant transport to and from the reaction site. All these requirements may be fulfilled at the interface between dispersed platinum particles and recast ionomeric electrolyte, which provides the potentially active reaction sites of the electrode.

Figure 2 shows a schematic of the electrode structure using the anode as an example. The cathode electrode structure is identical. Carbon particles (Vulcan XC-72) with reported primary particle size of 30 nm [14] form a convoluted structure that provides the electron conductivity to the current collectors and the external electrical circuit. The catalysts used are typically nanocrystalline (< 4 nm) platinum particles (black spheres) supported on the high-surface-area carbon blacks (gray) [15]. The polymer electrolyte of the catalyst layer (yellow/green) wets the surface of the carbon particles and partly fills the spaces between them. This establishes an electrolyte network that enables protonic transport to the membrane. Proton transport requires a well-humidified electrode and membrane, because the ionic conductivity of polymer electrolyte is highly dependent of the water content [16]. Sufficient hydration levels of the electrode and the membrane are attained by proper humidification of the gas streams. Water and fuel diffuse into the void spaces of the highly porous structure of the electrode. The water keeps the polymer electrolyte hydrated and thus highly proton conductive.

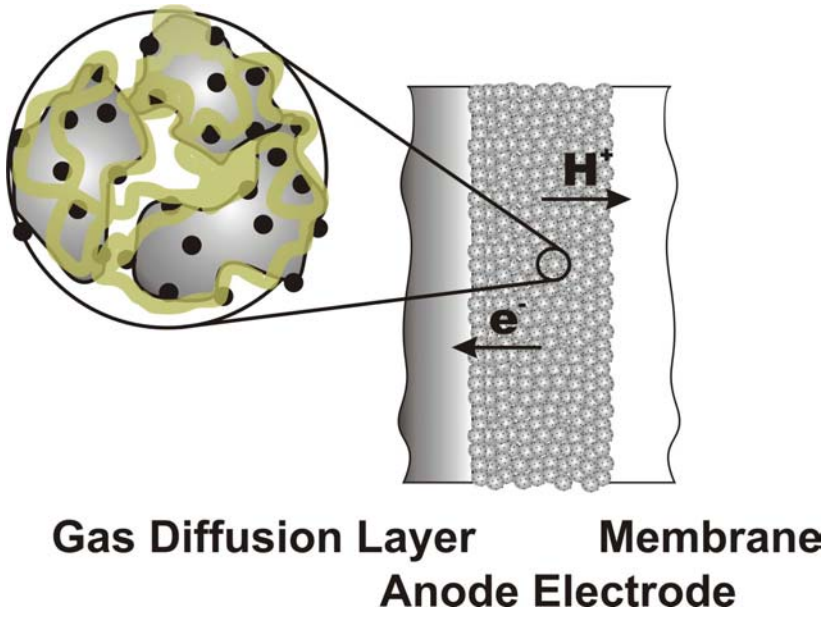

Figure 2: Schematic of a three phase interface structure of a PEFC electrode.

When suitable catalysts are used, PEFCs are, even at low operating temperatures, highly reactive. The HOR requires an overpotential of only 20-30 mV to reach a reaction rate of 1mA/cm^2 at a smooth platinum ionomer interface, whereas the ORR requires an overpotential of around 400 mV to reach the same current density at the same type of interface [17]. Thus, the processes at the anode are generally faster compared to the cathode processes. AC impedance investigations by Raistrick et. al. [18] and by Springer et. al. [19] have shown that the total impedance associated with the interfacial hydrogen oxidation process at the Pt/hydrated membrane interface is indeed much smaller than that of the ORR process in the same electrolyte. As a result of the high rate of the hydrogen oxidation reaction at platinum in contact with this ionomeric medium, the voltage drop contribution of a well-humidified hydrogen anode in a PEFC operating at 80 °C at 1 A/cm^2 is usually considered negligible. This is not the case when the anode side of the membrane becomes dehydrated and/or the hydrogen feed stream to the cell is less than perfectly pure [20].

Similar to the anode reaction, the cathode reaction also occurs at the interface between dispersed platinum particles and ionomeric electrolyte. The latter is the medium of solvation for both reactants at the cathode, dioxygen molecules and protons [21]. Oxygen diffuses into the electrolyte to this interface, where it may dissociate and take up protons and electrons following a rather complex and not-well understood mechanism. ORR kinetics is a very important factor in PEFC operation and has been a subject of great interest within the scientific community [22], [23].

1.2.3 The Polymer Electrolyte Membrane

The polymer electrolyte membrane of a PEFC is another key component of fuel cell performance. Requirements of the polymer electrolyte membrane are high proton conductivity, good insulation of electronic currents, good separation of fuel and oxidant, chemical and thermal stability of the material, and low cost [24].

Nafion is the standard polymer electrolyte membrane employed in fuel cells, but a substantial portion of the total fuel cell system cost arises from the fluoro-chemistry involved in the production of Nafion. Because polyaromatic membrane production costs are lower, they offer an economically interesting alternative to Nafion provided their properties are similar for use in PEFCs. Research groups all over the world are investigating the development of alternative electrolyte materials for use in fuel cells [25]-[26]. However, in all the studies presented here the standard material Nafion was used, since it is a well-characterized and widely used proton conductor.

Nafion consists of a hydrophobic Teflon backbone with randomly attached long pendant chains terminated with fluoromethane sulfonic acid groups. These groups are sites of very high hydrophilicity and hence, in the presence of water, the place of preferential hydration [27]. The combination of high acidity of the sulfonic acid groups and flexibility of the side chains in Nafion is the major cause for high proton conductivities. The sulfonic acid groups build continuous strings or channels through the entire membrane, the precondition of an efficient protonic transfer. A fully hydrated Nafion membrane is expected to have a distance of 7-8 Å between the sulfonic acid groups inside of the channels [28]. While the sulfonic groups are not able to move within the membrane structure, their protons dissociate in an aqueous environment [29]. The presence of water is also essential to facilitate proton mobility. If fully saturated with water, Nafion attains conductivities up to 0.1 S/cm for 22 water molecules per sulfonic acid group at 30°C [30]-[31].

1.2.4 Water Management

It is a critical requirement when operating PEFCs to maintain a high water content in the electrolyte to ensure high protonic conductivity. Sufficient hydration of the membrane offers a low resistance to current flow and increases overall efficiency. But without adequate water management, an imbalance will occur between water uptake and water loss of the cell. Adverse effects of water imbalances are flooding of the electrodes, dehydration of the solid polymer membrane, dilution of reactant gases by water vapor, and membrane-electrode delamination [32].

The water content in the cell is determined by the balance of water or its transport during operation [32]. Contributing factors to the water transport are the electro-osmotic drag through the cell, back diffusion from the cathode, and the diffusion of water in the fuel stream through the electrodes. Protons carry between 1 and 2.5 molecules of water with them through the electrolyte membrane, depending on the characteristics of the

electrolyte and the electrodes [33]. The amount of water transported is a function of the cell current. At high current density electro-osmotic drag increases and the water balance of the system changes. But during operation additional water is produced at the cathode interface as a function of current density. Part of this water diffuses back into the membrane and internally hydrates it. This process limits the net water transport to nearly zero at proper humidification of the membrane [30]. Surplus water however may flood the pores of the cathode and thus create a gas diffusion barrier to the platinum reaction sites.

All in all, a delicate water balance must be maintained among the electrode, electrolyte, and gaseous phase in the porous electrode structure to achieve the highest possible performance. Ideally, the incoming gases are humidified just enough at a given current density, to maintain optimal membrane and electrode hydration while preventing flooding of the gas diffusion layer.

1.2.5 Polarization Curve and Losses

Fuel cell performance is typically presented in the form of polarization curves. A characteristic polarization curve of a fuel cell is shown in **Figure 3**. Even without current flowing, because of the sluggish ORR at the cathode and hydrogen crossing through the electrolyte from anode to cathode, the open circuit voltage (which is usually measured close to E_{oc} = 1.0 V) is not nearly as high as the ideal reversible cell voltage of 1.16 V at 80°C operating on H_2/air [34]. In general, losses at the PEFC cathode are the single most important source of loss in the PEFC, as is the case in all other low temperature cells [21]. Next to the aforementioned overpotential at open circuit η_{oc} several other sources contribute to losses in a practical operating fuel cell. They originate primarily from the activation polarization η_{act}, the ohmic polarization η_{Ω}, and the concentration polarization η_{conc}. As shown in Figure 3, the relative importance of these overpotentials on the polarization curve depends on the operating current densities. The following sections shall introduce these three current dependent major loss mechanisms.

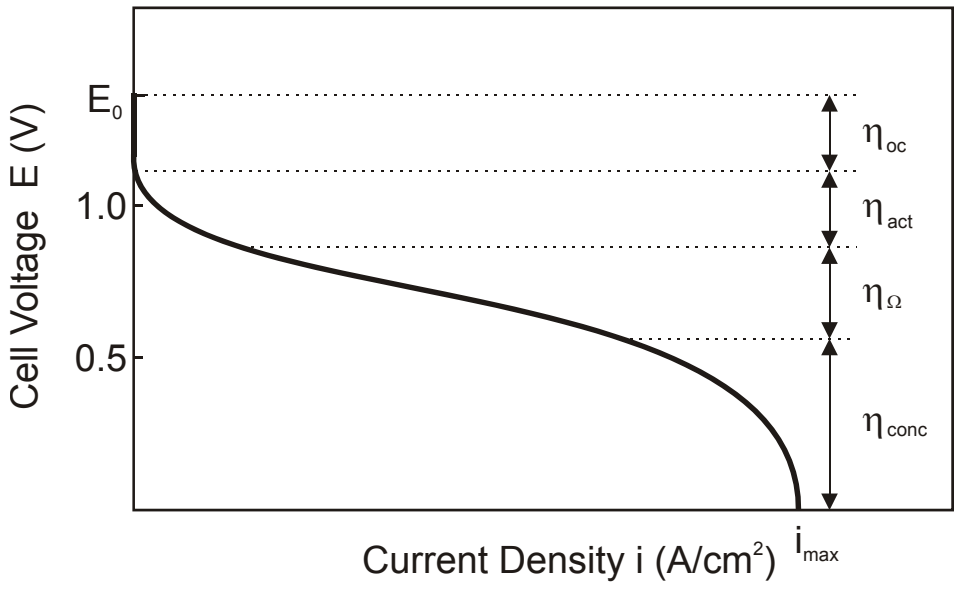

Figure 3: Polarization curve of a PEFC. The cell voltage plotted as a function of the current density is shaped by fuel cell losses.

Activation Polarization η_{act}

At low currents the activation polarization loss η_{act} is dominant. Electronic barriers resulting from the double layer capacity of the electrolyte-electrode interface have to be overcome. The electrical potential that drops at the double layer capacity disturbs the equilibrium state, accelerates the reaction in one direction and reduces it in the other. Thus a current is obtained [34]-[35]. The current density i of the reaction is described by the Butler-Volmer-equation (4) as a function of the exchange current density i_0, the electron transfer coefficients α, the amount of exchanged electrons n_e, the Faraday constant F, the activation polarization η_{act}, the general gas constant R, and the temperature T.

$$i = i_0 \left\{ \exp\left(\frac{\alpha n_e F \eta_{act}}{RT} \right) - \exp\left(-\frac{(1-\alpha) n_e F \eta_{act}}{RT} \right) \right\} \qquad (4)$$

Assuming a small fuel cell current, with an activation polarization that exceeds the limit given by equation (5), a significant shift of the reaction equilibrium can be observed and the reverse reaction can be neglected. Solving of equation (4) towards the activation polarization derives the Tafel equation (6), which describes the activation polarization as a function of the cell current. The parameter *a* depends on electrode materials. It includes the exchange current density i_0. Factor *b* is called the Tafel slope. It includes the electron transfer coefficient α.

$$\left|\eta_{act}\right| >> \frac{RT}{n_e F} = \frac{25.7}{n_e}\,mV \text{ (at 25°C)} \tag{5}$$

$$\eta_{act} = b \cdot \ln\left(\frac{i}{i_0}\right) = a + b \cdot \ln(i) \tag{6}$$

One focus of this work is the contamination of the catalyst layer by carbon monoxide (CO), which impacts the activation polarization of the anode. If CO is present in the anode feed stream, it adsorbs on the platinum catalyst and decreases the exchange current density of the electrode. Consequently, activation polarization increases and cell performance drops.

Ohmic Polarization η_Ω

The well-known Ohmic Law describes the resistance a charged particle experiences while traveling through a medium. In the fuel cell, electrons and protons move through material and hence cause ohmic losses η_Ω that increase linearly with the cell current as expressed in equation (7). The serial resistance R_S, that is valid for the single fuel cell, can be divided into the protonic membrane resistance, $R_{membrane}$, and the electronic resistance of the electrodes and the electrical circuit, R_{electr}. The membrane resistance is dependent on the chosen electrolyte, its state of hydration, and its thickness, while the electronic resistance is dependent on the chosen materials of the wires and the gas diffusion layer, and the contact resistance of the assembled hardware.

$$\eta_\Omega = R_S \cdot i = \left(R_{membrane} + R_{electr}\right) \cdot i \tag{7}$$

The serial resistance of a fuel cell can be determined during fuel cell operation using either AC impedance spectroscopy at a predetermined frequency or the current interruption technique. Both techniques do not allow identification of the individual ohmic polarizations. But in a well assembled hardware the membrane resistance is significantly higher than the electronic resistant and valuable information about the hydration state of the membrane can be obtained.

Concentration Polarization η_{conc}

The consumption of a reactant at an electrode generates a loss of potential since the environment is unable to maintain the initial concentration of the reaction participant by diffusion. As a result a concentration gradient is formed. Several processes may contribute to concentration polarization: slow diffusion in the gas phase in the electrode pores, solution/dissolution of reactants and products into and out of the electrolyte, or diffusion of reactants and products through the electrolyte to and from the electrochemical reaction site. At high fuel cell current densities, slow transport of reactants and products to and from the electrochemical reaction site is a major contributor to concentration polarization.

The rate of mass transport to an electrode surface in many cases can be described by equation (8), Fick's first law of diffusion [36]. The electrode current density i is described by the number of exchanged electrons n_e, the Faraday constant F, the diffusion coefficient of the reacting species D, its bulk concentration C_B, its surface concentration C_S, and the thickness of the diffusion layer d.

$$i = \frac{n_e F D (C_B - C_S)}{d} \tag{8}$$

The limiting current i_L is a measure of the maximum rate at which a reactant can be supplied to an electrode. It occurs when $C_S = 0$. Manipulation of equation (6) and employment of i_L delivers equation (9).

$$\frac{C_S}{C_B} = 1 - \frac{i}{i_L} \tag{9}$$

The Nernst equation for the reactant species of concentration C is given by equation (10). For the "zero-current" case the surface concentration at the electrode equals the bulk concentration, and $C = C_B$. When a current is flowing, the surface concentration becomes less than the bulk concentration, and $C = C_S$.

$$E = E^o + \frac{RT}{n_e F} \ln C \tag{10}$$

The potential difference produced by a concentration change at the electrode is called concentration polarization and is given by equation (11) [36]. Concentration polarization significantly increases when the surface concentration of the reactant approaches zero. Under this condition, the electrochemical reactions are very fast, and the losses are dominated by the diffusion processes. In that case, the current density i approaches the current density limit i_L.

$$\Delta E = \eta_{conc} = -\frac{RT}{n_e F} \cdot \ln \frac{C_S}{C_B} = -\frac{RT}{n_e F} \cdot \ln\left(1 - \frac{i}{i_L}\right) \tag{11}$$

Activation and concentration polarization can exist at both electrodes in fuel cells, while ohmic polarization is dominated by the membrane resistance. To visualize the three major loss mechanisms of the PEFC, **Figure 4** illustrates their current dependence in principle. The combination of these losses produces the shape of the characteristic fuel cell polarization curve (compare Figure 3).

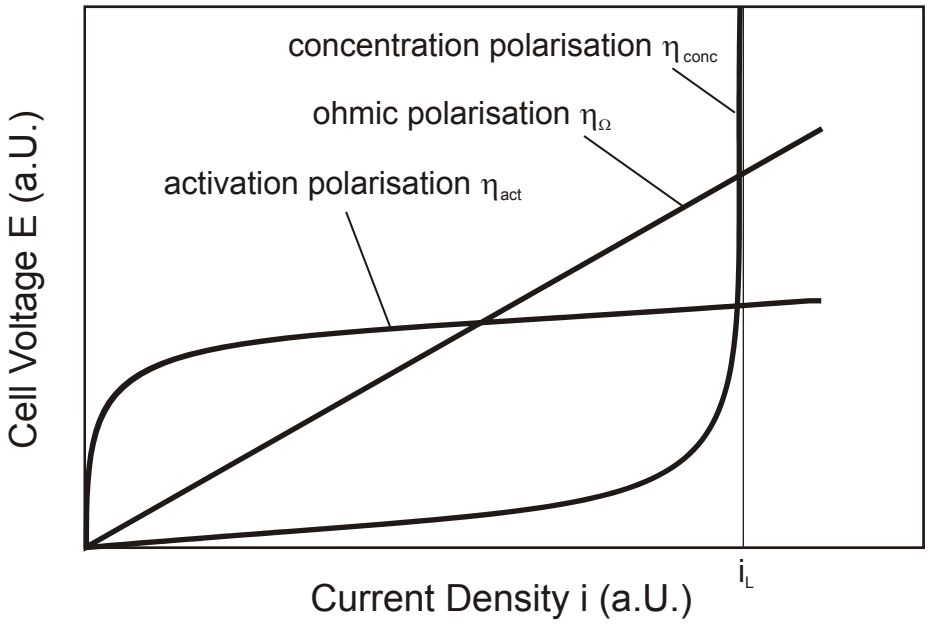

Figure 4: Qualitative current dependence of the major PEFC loss mechanisms.

1.3 Direct Methanol Fuel Cell

Methanol, after hydrogen, is the second most attractive fuel for fuel cell applications that employ polymer electrolytes. The demands are high to identify a fuel that is easily transportable and simple to convert into energy from liquid state. Methanol is liquid at ambient temperatures and has high energy density. It can be stored unpressurized, offers simple storage systems, and can be distributed via the available infrastructure if minor adjustments are made. Methanol offers a high energy density, and can be produced on a large scale from natural gas with efficiencies of around 65-70%. If produced from biomass, methanol could participate in a closed carbon dioxide cycle, and thus help preventing global warming [37].

Two different concepts were followed by research and development groups for use of methanol in fuel cells.

(i) Harnessing the advantage of methanol as an energy carrier for storage purposes, but reforming it into hydrogen prior to energy conversion. This strategy avoids dealing with the electrochemical activity of methanol, which is orders of magnitude less than that of hydrogen, but it has to deal with the increased complexity and losses of the reforming system. Also, reformation of methanol or other hydrocarbon fuel produces hydrogen containing at least trace amounts of carbon monoxide, which is highly detrimental to cell performance.

(ii) Direct electrochemical oxidation of methanol within the fuel cell, creating a DMFC system. The idea of a DMFC system is attractive compared to a hydrogen reformate based system, due to its inherent simplicity. The methanol can be fed as an

aqueous solution into the cell anode. The fuel vaporizer system including its heat source and controls becomes unnecessary. Humidification of the membrane is already provided by the aqueous solution and consequently gas humidifiers are not needed. Furthermore, the methanol-water mixture will serve a dual purpose in a DMFC stack system. It simultaneously operates as fuel and stack coolant. Overall, the DMFC system can be designed significantly simpler than a methanol reforming system, with smaller system size, less weight, and less parasitic peripherals. These advantages generate significant interest in DMFC systems, especially for portable power applications.

Today, research on fuel cell systems that operate on methanol solutions employ polymer membranes rather than liquid electrolytes. The solid state acid polymer electrolyte of the DMFC rejects carbon dioxide produced during the electro-oxidation of methanol and thus eliminates problems with carbonation [38]. It also minimizes corrosion in the cell and avoids shunt currents, both common problems in liquid electrolyte fuel cells. Finally, the polymer membrane functions as a separator of fuel and oxidant and allows for compact cell geometry. Unfortunately, the selectivity of polymer electrolyte membranes is significantly lower for methanol than for hydrogen. This generates individual losses particular to the DMFC system.

1.3.1 Working Principle

Significant similarities exist between state of the art DMFCs and PEFCs. **Figure 5** shows the schematic of a DMFC including supplied reactants and exhausts. The liquid fuel, usually a 0.3 - 0.5 M methanol solution, requires different diffusion materials that account for the aqueous nature of the reductant. The fuel is typically recycled to achieve optimized utilization.

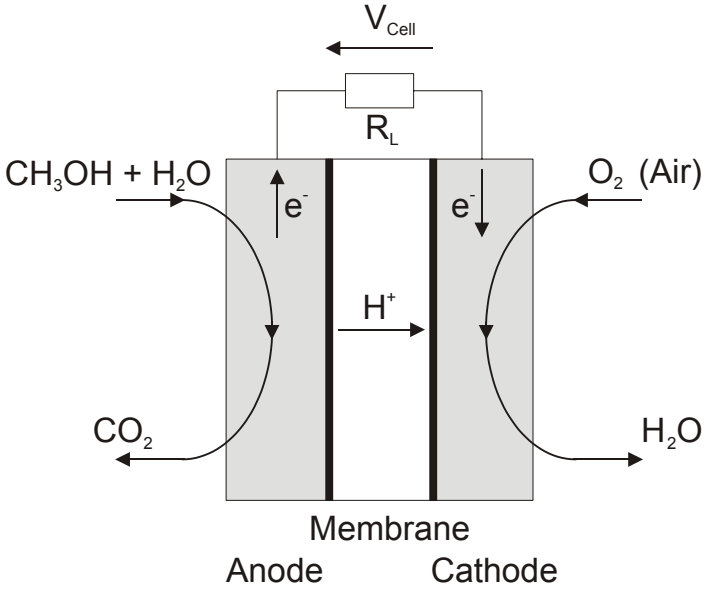

Figure 5: Basic cell and working principle of a DMFC.

The net reaction of a DMFC is shown in equation (12). Unlike the reaction of a hydrogen fueled cell, water is needed as a reactant for anodic reaction and carbon dioxide is produced as a reaction product. The electrochemical open circuit potential of the reaction is with E°=1.186V, very close to that of a hydrogen cell (E°=1.229V), but nonetheless the losses within the cell are significantly higher, especially at the anode. The anode reaction consists of the electro-oxidation of methanol as shown in equation (13). This reaction delivers six electrons. The cathode reaction shown in equation (14) is identical to the cathodic reaction of the PEFC. Water is produced from oxygen, protons and electrons.

DMFC Reaction:

$$CH_3OH + {}^{3}\!/\!_{2}\, O_2 \rightarrow CO_2 + 2H_2O \tag{12}$$

Anode Reaction:

$$CH_3OH + H_2O \rightarrow CO_2 + 6H^+ + 6e^- \tag{13}$$

Cathode Reaction:

$${}^{3}\!/\!_{2}\, O_2 + 6H^+ + 6e^- \rightarrow 3H_2O \tag{14}$$

1.3.2 Methanol crossover

One concern of DMFC applications with polymer electrolyte membranes is the permeation of methanol across the membrane. The methanol molecule is of small size and polarized by the presence of its oxygen atom. As a consequence, methanol and water are miscible at all concentrations. The permeability of hydrogen, carbon monoxide or oxygen is dominated and limited by their solubility in water and selectivity of the membrane is high. This limitation does not exist with methanol, which is rapidly transported across Nafion, and is chemically oxidized to CO_2 and H_2O at the cathode. There is a significant decrease in coulombic efficiency for methanol consumption, by as much as 20% under practical operation conditions [39]. Also, crossover methanol lowers cathode potential and consequently impacts fuel cell efficiency further.

Methanol crossover is a significant source of irreversible power and fuel losses in a DMFC and one important subject of DMFC research efforts. Its overpotential, η_{xover}, is proportional to the methanol flux through the membrane [40]. The phenomenon of fuel crossover is linked to the thickness of the membrane: if an excess of methanol is present at the anode side, the membrane acts as a diffusion barrier according to Fick's law, meaning that the methanol flux becomes proportional to the membrane thickness. Consequently researchers are reluctant to employ thin commercial membranes like

Nafion 112, which is 50 μm thick, in DMFC applications [41]. The most commonly used membrane employed for DMFC applications is Nafion 117, whose thickness is 178 μm.

Two approaches are pursued by the research community to overcome the high methanol crossover disadvantage of Nafion:

(i) Substitution of Nafion with membrane materials that show increased methanol selectivity and solve other challenges of the DMFC, such as production cost and operation temperature limits. Research efforts are currently performed by numerous research groups world wide to develop membrane materials based on aromatic compounds, like Poly Ether Ether Ketones (PEEK), Poly Ether Sulfones (PES). Polybenzimidazole (PBI), or Poly Phoshazene (PPZ) [25]-[26]. Some of these materials show promising results. S. Wasmus et. al. reports in his review a tenfold decrease of methanol crossover and very satisfactory thermal stability of basic polymers (polybenzimidazole and polyacrylamide) doped with inorganic acids [41]. The chosen electrolyte material for fuel cell applications should have high ionic conductivity (>0.05 S/cm) under working conditions and low permeability to methanol ($<10^{-6}$ moles/(min cm^2)). Furthermore it must be chemically and electrochemically stable under operating conditions.

(ii) Development of methanol tolerant catalyst alternatives to Pt for oxygen reduction. The increasing interest in this approach, however, should take into account that if the methanol which permeates through the membrane is not completely oxidized at the cathode surface to CO_2, it would contaminate the water at the outlet of the cathode compartment. This could cause environmental problems in the absence of a proper technical solution [39].

1.4 Hardware and Measurement System

Having presented the fundamentals of fuel cells in the previous sections, the following section will focus on the equipment needed to control and operate a fuel cell in a laboratory. Fuel cell research often employs single cells for testing and design development. The hardware and system needed for a single cell are described using the example of a PEFC system. The differences between a PEFC and a DMFC system are then discussed separately.

1.4.1 Fuel Cell Hardware

As shown in **Figure 6**, the membrane electrode assembly (MEA) (gray-black) is sandwiched between two electron conductive gas diffusion layers (GDLs) (black), also referred to as backings, and the anode and cathode flow-fields (yellow). Please note, that the figure omits some essential components needed to achieve functionality. Gasket material surrounds the backings and is compressed between the graphite flow-fields and MEA. This provides sealing to the environment and allows pressurization of the system to improve the reaction [42]. Current collector plates connect the electron conductive

flow-fields to the external electrical circuit. Compression of the hardware is typically realized employing 'endplates'. These solid metal plates are electrically isolated from the rest of the fuel cell.

For operation, the fuel and oxidant are fed through the flow-field from inlet to outlet, along machined flow channels. Flow channel design can vary widely from single channel serpentine flow-fields, and multiple channel flow-fields, to parallel flow fields or interdigitated flow-fields. Standard single cells at Los Alamos National Laboratory usually employ single or multiple channel serpentine flow-fields which are operated in co-flow arrangement and have electrode areas of 5 cm^2 and 50 cm^2. The gases travel along the flow channels of the flow-fields. From here, they diffuse perpendicular into the GDL and into the electrode where the electrochemical reaction occurs.

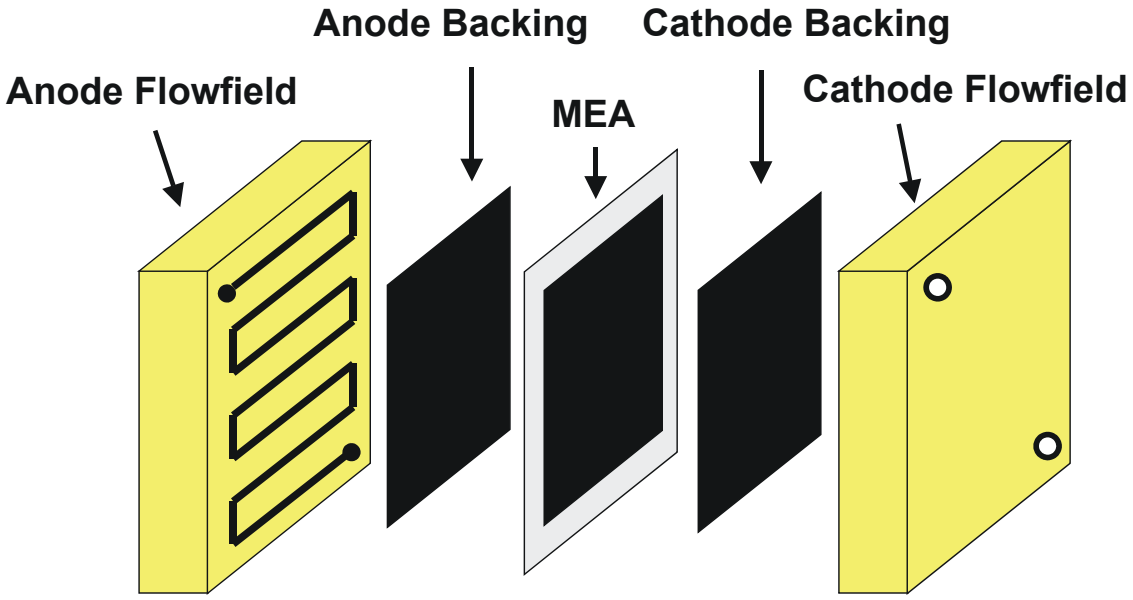

Figure 6: Basic fuel cell hardware.

1.4.2 Single Cell Measurement System

Basic research demands a controlled environment for accurate interpretation of experimental data. Fuel cell research and development efforts often employ single fuel cells for testing and design development. A set of peripherals is used to control the environmental parameters of the cell. **Figure 7** shows the schematic of a typical single cell measurement setup. All controls involving the two gas flows are operated identically, but kept separate for both electrodes. The gas flows can either be adjusted manually with flow meters (Roto meters) or electronically via mass flow controllers (MKS Inc.) The latter allow accurate gas mixing and flow tracking of reactant and/or oxidant. These mass

flow controllers require calibration to compensate for pressure and temperature of their location, e.g. ambient pressure at Los Alamos National Laboratory is about 780 mbar instead of the standard 1 bar, due to its altitude of 2200m above sea level.

Before fuel and oxidant are injected into the PEFC hardware, they are humidified using a humidifier unit. Inside this unit, the gas passes through a long and thin Nafion tube, which is immersed in temperature controlled water. Water vapor diffuses through the Nafion tube to the gas stream, where it is absorbed. The gas subsequently bubbles through the water reservoir to achieve saturation. The temperature of the water and the flow rate of the gas determine the amount of water uptake. Typically humidification close to 100% saturation for a given temperature can be achieved with small gas flows. However, for high gas flows, the saturation can decrease to as low as 70% [58].

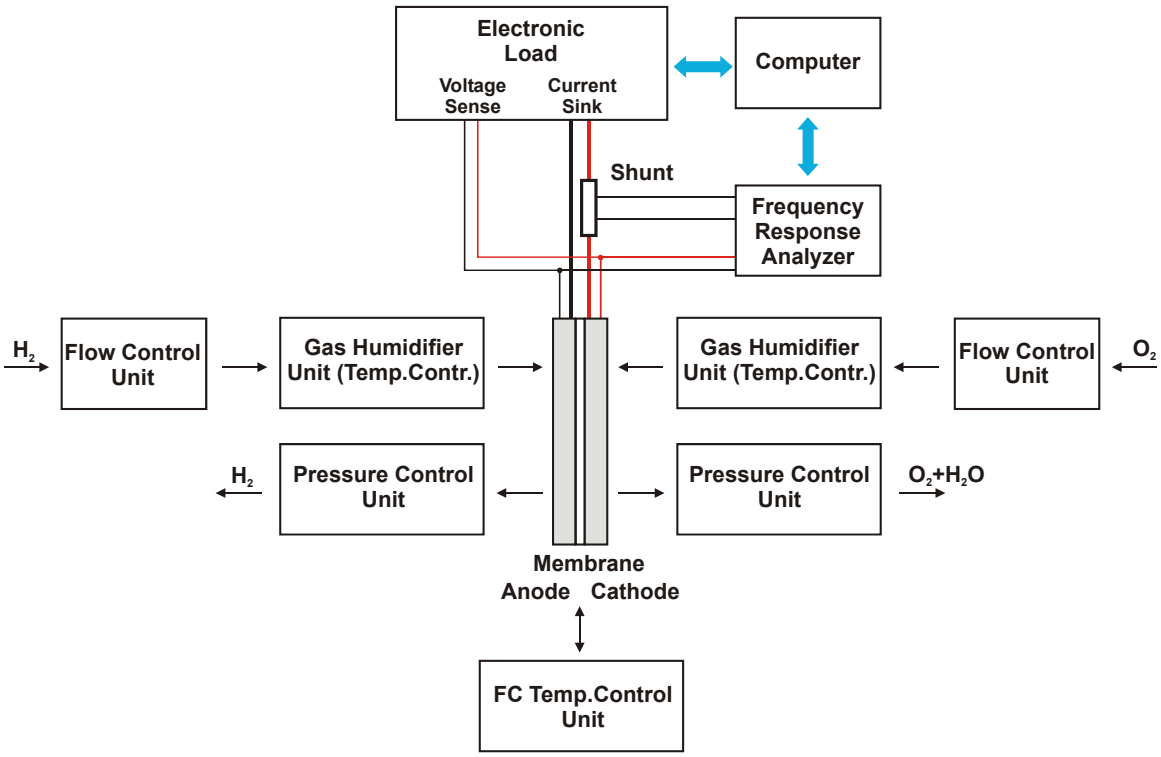

Figure 7: System components of single fuel cell test station.

The pressure inside the fuel cell can be adjusted and controlled by back pressure valves located at the exhaust lines of the fuel cell. Typical operating pressures vary between ambient and 2 bar gauge pressure. Unlike practical fuel cells, single cell units possess a large ratio of hardware surface area to electrode area. To accomplish uniform heat distribution and standard operating temperatures of 80°C or more, externally controlled heat cartridges are operated inside the endplates of the single cell hardware.

Once the gases are flowing, and the temperatures and pressures are set and stabilized, the fuel cell is operated using an electronic load. This instrument continuously measures voltage and current of the cell and adjusts either the voltage of the cell (voltage mode), or the current through the cell (current mode). The measured data is transmitted to a computer that controls the measurement and the interaction of the electronic devices.

To obtain information about the hydration of the fuel cell membrane, the fuel cell's high frequency resistance (HFR) is measured by a Frequency Response Analyzer (FRA). This is done by applying a sinusoidal perturbation to the cell current and monitoring the cell voltage response. This is done at a predetermined frequency, to minimize capacitive contributions, and at a predetermined amplitude, large enough for good signal to noise response and small enough to be a good approximation of the set point current. The resulting real part (in phase component) of the complex cell resistance represents the high frequency resistance of the cell and is affected by electronic components and the hydration state of the MEA. Performed at varying frequencies, this measurement records the AC impedance spectrum of the cell, a powerful tool for fuel cell analysis. For storage and further use the measured data is transmitted to a computer that also controls other measurements and interactions of the electronic devices.

1.4.3 DMFC Fuel Cell System

Minor differences exist between methanol and hydrogen fueled systems that arise from the property differences of the fuel. Gaskets, diffusion layers, and catalyst loading and type need to be adjusted to the chemical and physical properties of the cell. The fuel feed system is additionally adjusted with respect to the liquid nature of methanol. Pumps are needed to propel the methanol solution through the fuel cell. The anode and cathode of the DMFC are typically operated without backpressure and humidification on the cathode. Thus, pressure control and gas humidifier units are not needed for DMFC testing. The methanol solution is typically recirculated in an operating fuel cell, which brings the temperature of the fuel close to cell temperature. To simulate this behavior in DMFC testing, the methanol fed to the cell is preheated by a continuous-flow heater to maintain a uniform temperature distribution within the fuel cell.

All other fuel cell peripherals are identical to the hydrogen fuel cell system. They depend not on the fuel type, but on the size and power output of the cell only.

2 Research Objectives

This thesis studies effects in hydrogen and methanol powered fuel cells that employ solid polymer electrolyte membranes. The research was performed to detect and understand spatial variations in these fuel cells by exploiting the segmented cell approach, a research tool redesigned and continuously refined during the project. The diagnostic information obtained by this method was expected to hold the potential for system improvements.

Hydrogen is the best fuel for fuel cells that employ solid electrolyte membranes, but because of unsolved H_2 storage challenges alternative fuels, such as hydrocarbons (e.g. gasoline, natural gas) and alcohols (e.g. methanol) are also considered [43]-[44]. Initial reformation of these fuels to hydrogen-rich synthetic mixtures produces significant amounts of carbon monoxide (CO). Subsequent cleaning by a water gas shift reactor and a preferential oxidizer (prox) reduces the CO content to below 100 ppm, depending on the design and operating conditions of the cleaning stages [6], [17]. Given that PEFCs operate at relatively low temperature, even these trace amounts of CO impurity are detrimental to their operation [17]. Considerable research effort has been focused on CO adsorption on platinum surfaces [45]-[53]. Fundamental studies include CO chemisorption on small and well-defined single-crystal Pt-surfaces in contact with aqueous electrolytes of well-defined composition. Carbon-supported polycrystalline catalyst composites, such as those used in hydrogen/air fuel cells do not provide such an ideal environment, steps and kinks on the catalyst surface structure lead to differences in CO adsorption-desorption behavior [54]. The effect of CO adsorption on fuel cell performance at steady-state poisoning conditions has been extensively studied [17], [55]-[57], but seldom in a practical fuel cell system.

CO adsorption on a fuel cell electrode is a temporally and spatially inhomogeneous process that depends on local operating conditions. The operating conditions gradually vary along the flow-field due to concentration gradients developing as a result of fuel and oxidant consumption, and water generation at the cathode. Optimizing fuel cell performance requires a good understanding of variations in current distribution in the fuel cell as a function of fuel impurities and operating conditions. Standard single cell measurements, such as current density, represent only average values of processes occurring at the entire electrode area. A successful approach to acquiring local spatial information is through the use of a segmented fuel cell [58]-[60]. The most recent segmented cell at Los Alamos National Laboratory (LANL), developed for and during this work, is designed similar to an ordinary fuel cell. The key difference is that one of the electrodes (anode or cathode) is divided into several segments resulting in an array of smaller electrodes. Each one of these electrodes can be independently probed for current,

voltage, and resistance [61]. This configuration allows for mapping of the current distribution across the surface of the electrode, in addition to studying local effects, such as CO adsorption.

The first part of this thesis focuses on the time and space distribution of surface CO and its impact on PEFC performance, measured *in situ* in a fuel cell system. Unlike most reports published to date, this section of the thesis part concentrates on non-steady-state states of the fuel cell and time-dependent distribution of the CO in the segmented anode. The study's goal was to provide direct insight into the CO poisoning processes in a real fuel cell. These findings were expected to improve understanding of the mechanism of CO poisoning and, consequently, to support the development of more CO tolerant fuel cell systems.

Operating on a liquid fuel rather than hydrogen or reformate, offers unique advantages and new challenges for system simplicity and efficiency. The most attractive liquid fuel is methanol, fed as an aqueous solution to the anode of a DMFC, where it is electrochemically oxidized. This oxidation is one of the main challenges faced extensively by the DMFC research community [6], [41], [62]-[64]. It is believed to take place by a multi-step reaction scheme, which involves a sum of parallel and sequential reactions [65]-[66]. Carbon monoxide is one of the intermediate species from methanol oxidation [67]. CO adsorbs onto Pt causing catalyst poisoning in the same way as it happens with CO impurity in hydrogen fuel cells. By using Pt-alloys, such as Pt-Ru, is possible to promote the electro-oxidation of CO to CO_2. Ru is able to form Ru-OH from water at significantly lower potentials than Pt. These Ru-OH species react with adjacent Pt-CO species generating CO_2 and thus reactivating Pt sites for continuing methanol oxidation. Another serious challenge for DMFC operation is methanol crossover through the membrane from anode to cathode [68]-[71]. Typical DMFC cathode catalysts consist of unsupported platinum black, a material more prone to detrimental effects of CO than Pt-Ru. The presence of methanol at the cathode lowers the cathode's potentials and it also reacts chemically with O_2. This reaction competes with the ORR of the cathode and significantly decelerates the cathodic reaction [40], [72]-[73]. For this reason, in order to reach practical power outputs, DMFC's require large Pt loadings. The methanol permeating the electrolyte membrane is permanently lost to the generation of electrical energy, thus lowering the overall fuel efficiency.

Other factors have been reported to affect DMFC performance [74]-[82], but to date, little research has been reported that concentrates on spatial measurements of DMFCs [83]-[84]. While these reports demonstrate the viability of using a segmented cell under DMFC conditions, the existing works did not relate DMFC performance to operating conditions. The segmented cell approach developed during this study constitutes a powerful tool for investigating how various factors affect fuel cell performances and for helping optimization of cell design.

The second part of this work focuses on segmented cell studies to investigate a number of operating parameters important for DMFCs: (i) methanol concentration, (ii) methanol flow rate, (iii) cathode humidification, and (iv) cathode flow rate. The objective was to qualitatively and quantitatively determine effects along the flow-field as a function of the listed operating conditions and evaluate their importance with respect to DMFC efficiency. Understanding these effects was expected to help develop strategies beneficial for DMFC performance.

3 Experimental

Experiments were performed using segmented cells of two different generations. LANL's generation III (G-III) segmented fuel cell is based on the printed circuit board (PCB) approach by Cleghorn *et. al.* [58]; Generation IV (G-IV) was developed during the course of this work after analyzing the advantages and disadvantages of its predecessor and other systems known from the literature [59]-[60]. The new G-IV design contains more sophisticated hardware and measurement capabilities that allow for measurement of current, voltage and high frequency resistance (HFR) from each electrode element simultaneously. This greatly reduced data acquisition time and increased measurement accuracy [61].

3.1 Segmented Cell Hardware

The G-III segmented cell employed a four-fold serpentine channel anode flow-field that consisted of 18 graphite blocks embedded in a non-conducting epoxy resin. Each segment was externally connected *via* four wires that allowed independent measurements of segment's current and voltage. The anode catalyst layer, gas diffusion layer and current collector were also segmented. Each segment had an area of 4.45 cm^2, for a total anode active area of 80 cm^2. The single-piece cathode had an active area of 100 cm^2. Its outer dimensions closely matched the outer dimensions of the segmented anode.

The most recent G-IV segmented cell is shown in **Figure 8**. It contained a one-piece cathode with an active surface area of 104 cm^2. The G-IV anode was divided into 10 segments with 7.71 cm^2 active surface area each, matching the outer dimensions of the cathode. G-IV segments were manufactured of graphite blocks, which were inserted in an Ultem® (polyetherimide) frame using a two-component epoxy for sealing and attachment. To form a G-IV standard flow-field, six fold serpentine channels were machined into the surface as shown on the left side of **Figure 9**. Fuel was fed to the segments in consecutive order from gas inlet to gas outlet located in the upper right and lower left corner, respectively. Individual current collector plates for the segments, as shown on the right side of **Figure 9**, allowed low contact resistance per segment and resulted in higher measurement accuracy. The plates were kept aligned by another Ultem® framework, which also electronically insulated the segments to each other and to the endplate.

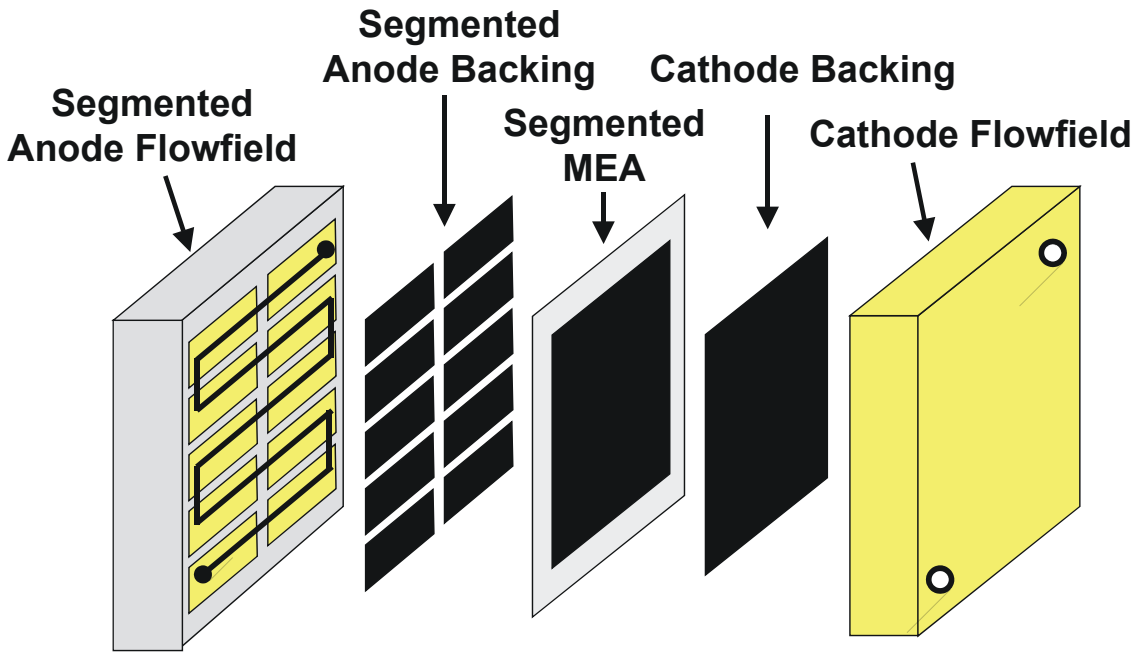

Figure 8: Basic G-IV segmented fuel cell hardware at Los Alamos National Laboratory.

The segmentation of the MEA, backings, and current collection was necessary to establish the potential for spatial anode polarization measurements, crossover measurements, and cyclic voltammetry measurements, the latter being one main focus of this work. The resolution of the presented system is limited by the edge effects of the necessary sealing areas that prevent cross flows of fuel, gas and electrons between the segments. The resolution has to be kept low enough, so that edge effects do not dominate the performance of the individual segments and influence the cell response. At the chosen low resolution of the presented setup, the gasket areas can be considered inert to the cell response and the system feasable to accurately record performance trends and spatial processes inside the fuel cell. It should be kept in mind, however, that higher spatial resolution may be needed to optimize and fine tune commercial fuel cell systems. If that is the case, a different approach is necessary to measure the current distribution of the fuel cell.

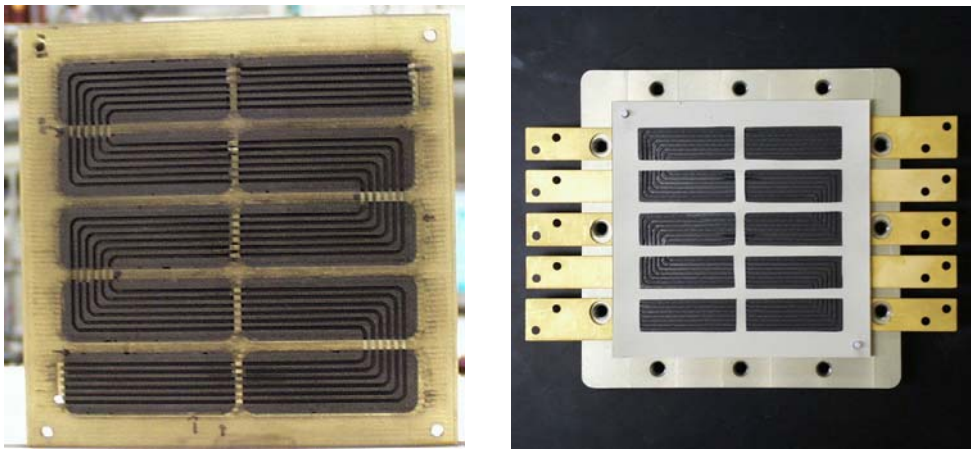

Figure 9: G-IV segmented six channel serpentine flow-field (left side) and segmented anode hardware including gasket and current collector plates.

During operation, the G-IV segmented hardware was part of the G-IV segmented cell setup as shown in **Figure 10**. Segment currents were individually measured by Hall sensor devices, which were physically separated from the fuel cell hardware. The sensors were calibrated and operated in a temperature controlled chamber at 50°C. Voltage followers amplified each of the signals for the AC impedance measurement of the HFR and for the segment current measurement. The output signals, well shielded and terminated close to the receivers, showed an average noise level less than 1 mV, equivalent to a current of ≤ 3.25 mA/cm^2. An additional set of wires sensed the segment voltages between the cathode and each anode segment, creating a four-wire measurement system to avoid offsets caused by contact resistance. A computer-controlled electronic load (Hewlett Packard, Model 6050) regulated either the total cell current or the cell voltage, by referencing to one segment voltage. The reference segment could be selected freely without influencing the measurement. The G-IV measurement system was able to simultaneously perform rapid measurements of total cell and segment voltages and currents. It recorded up to 18 complete data sets per second.

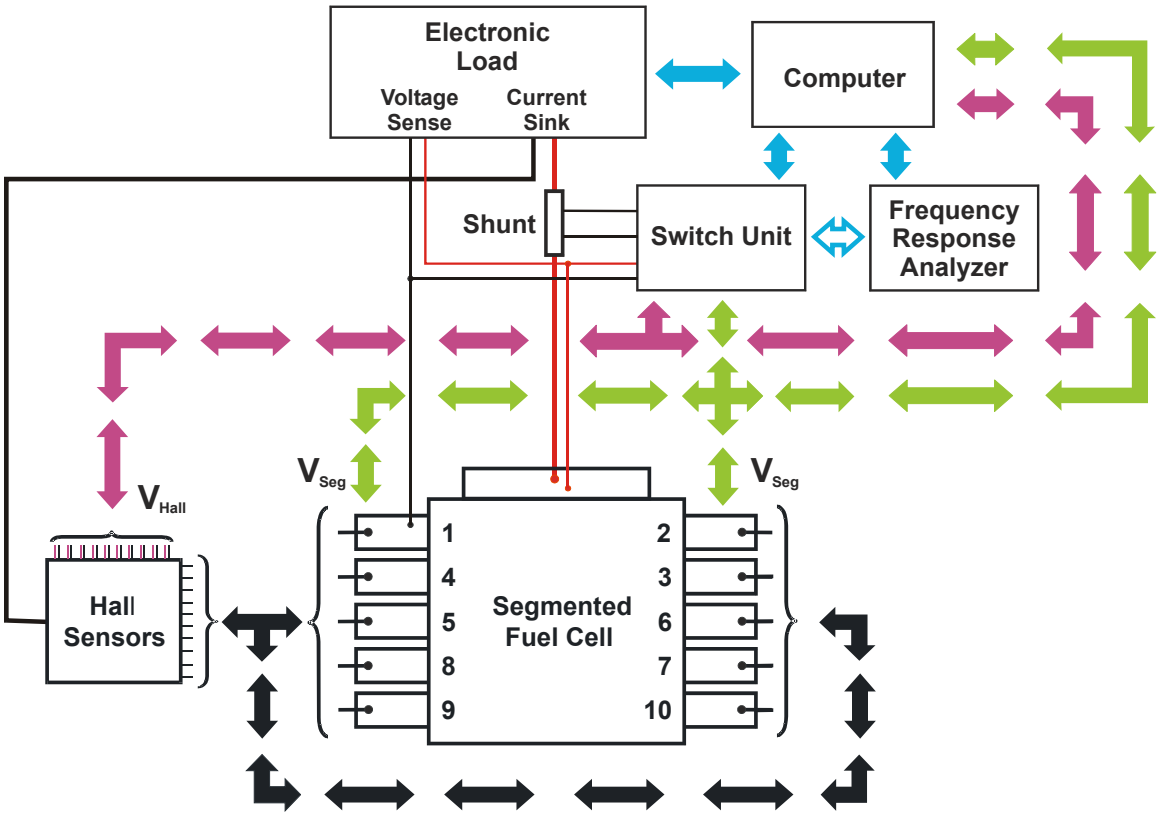

Figure 10: Schematic of G-IV segmented cell measurement setup.

The G-IV segmented cell system was capable of AC impedance spectroscopy, which has been proven to be a useful diagnostic tool for fuel cell research [19], [85]-[86] and is routinely used at LANL to determine HFR of fuel cells during operation. The G-IV segmented cell system employed both a shunt resistor and a Hall sensor in combination with a frequency response analyzer ((FRA); Solartron, Model 1260) to measure the high frequency resistance of the total cell during operation. To allow enhancement of the signal to noise ratio, low noise preamplifiers (SR560, Stanford Research Systems) filtered and amplified the signals before they were analyzed by the FRA [87]. A Switch/Control Unit (HP 3488A) allowed measurement of the HFR of all individual segments during operation. But the mechanical switching from segment to segment and the measurement itself required a minimum of one minute. Consequently, the HFRs of fast processes, such as CO transient measurements with high CO partial pressures (100 ppm) could not be recorded. Total cell HFRs were measured at 2 kHz perturbation frequency, segment HFRs at 5 kHz [61].

3.2 Membrane Electrode Assemblies

The described G-III and G-IV segmented cell setups were used to perform experiments with three different types of MEAs: (i) hydrogen operated MEAs of generation III and IV, referred to as G-III, PEFC and G-IV PEFC; (ii) methanol operated MEAs of generation IV, referred to as G-IV, DMFC.

G-III, PEFC

MEAs were manufactured using thin-film technique developed in house [88]-[90]. The standard ink composition used for PEFC applications contained 20% platinum on carbon (Vulcan XC-72, E-Tek) and 5% Nafion solution (1100 EW, Solution Technology, Inc.) in a weight ratio of 5:2, and tetrabutylammonium hydroxide (TBA-OH). To form G-III segmented MEAs the catalyst ink was hand painted onto Teflon supports ('decals'), sized to exactly match either the anode segments or the entire single-piece cathode. The anode and cathode blanks were repeatedly painted, oven-dried and weighed until the desired catalyst loading of 0.2 mg Pt/cm^2 was obtained. They were then aligned in a frame and hot-pressed onto a Nafion 1135 membrane (1100 EW, sodium form) at 210°C. After hot pressing, the MEA was boiled in 0.5 molar sulphuric acid to exchange sodium and TBA^+ ions for protons, rinsed in water, and dried on a vacuum hot plate at 60°C. This production process is very time intensive, though even the most painstaking preparation does neither result in uniform catalyst layers, nor in standard deviations of platinum loading of less than 12 or 13% [91].

G-IV, PEFC

There are faster means of catalyst coating than hand painting, such as screen printing [92]-[93], rolling techniques [94]-[96], and spraying methods [97]-[98]. Careful adjustment of catalyst ink properties while increasing transfer efficiency of ink and decal material can additionally increase the reproducibility of rapidly manufactured electrode layers [91]. To manufacture G-IV cathodes of 0.3 mg Pt/cm^2, Kapton decals were coated with a recently described machine spreader [99], hot pressed onto Nafion 1135, and proton exchanged. Coating ink differed from the standard ink described above by substituting 75% of the alcohol contained in the 5% Nafion solution by water. The resulting half-cells had a very homogeneous electrode and very good platinum loading precision of ±5% [91]. For MEA completion, the uncoated membrane side was spray coated to create ten anode segments of 0.2 mg Pt/cm^2 using the spray setup of LANL, which was developed in house and is described in detail in the Appendix. Spray ink was proton form standard catalyst/ionomer mix diluted by weight ratio of 1:2 with an isopropanol/water mixture of 1:1 by weight. Since no proton exchange step was needed after spray coating, geometry of the segmented anode remained exactly defined and allowed precise and easy alignment of the MEA into the setup. **Figure 11** shows a two-dimensional elemental map of platinum of such a sprayed segmented anode, taken with

X-ray microfluorescence spectroscopy (XRMF). The uniform color distribution of the image reveals the highly homogeneous platinum distribution on the individual segments. Platinum loading precision was determined to ±3%.

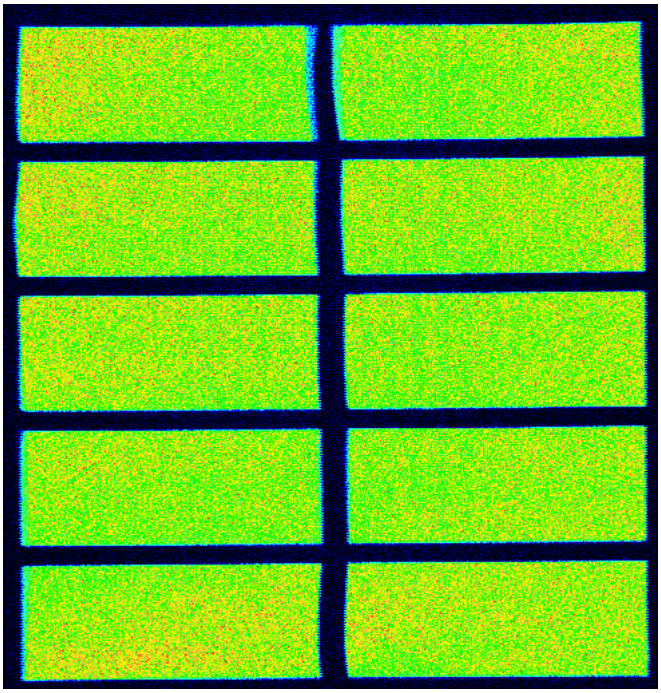

Figure 11: M-line XRF image of Pt in segmented PEFC anode produced by spray coating.

During the proton exchange step of the standard production method impurities are removed off the catalyst surface. Spray coating MEAs without performing a proton exchange step leaves these impurities on the catalyst surface. Carbon black typically consists of 90 to 99 wt% elemental carbon. Various surface groups containing oxygen, hydrogen, nitrogen, sulfur, halogens, and other elements can be introduced into the carbon sample during the manufacturing process [100]. Kangasniemi et. al. identified ether, carbonyl, and carboxyl surface oxide species, with a minor fraction of electroactive hydroquinone/quinone species on Vulcan XC-72 [101], the catalyst support employed in this work. Sulfur, organic compounds and most other contaminations, can be completely removed from platinum catalyst with cyclic voltammetry [102]. Prior to operating G-IV segmented MEAs the anode surface was cleansed by means of cyclic voltammetry subsequent to cell break-in. Cycling was done in a potential range of either 0.1 to 1.1 V or 0.1 to 1.4 V until all contaminants were removed. **Figure 12** compares cyclic voltammograms of a proton exchanged catalyst layer of 5 cm^2 and 0.22 mg Pt/cm^2 at 25°C (left) with a sprayed catalyst layer of 7.71 cm^2 and 0.36 mg Pt/cm^2 at 80°C (right). Clearly, cycling removed the contaminating surface species that inhibited performance for hydrogen oxidation.

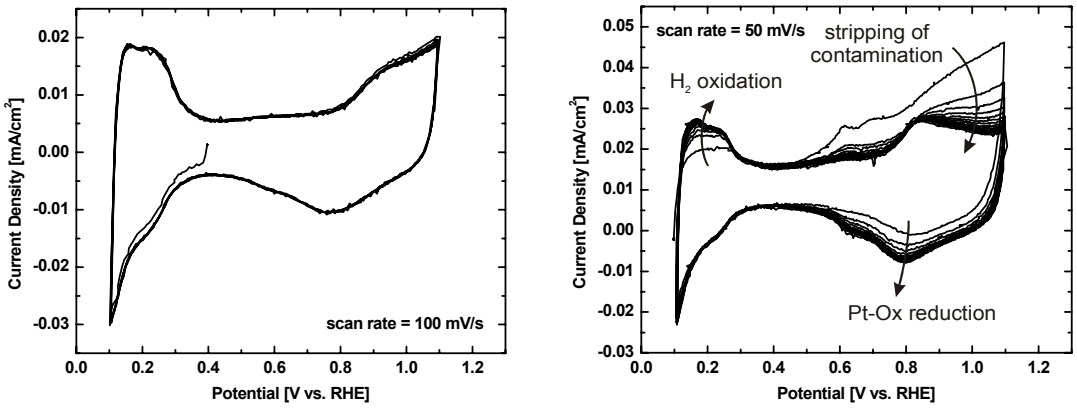

Figure 12: Cyclic voltammograms; left: Electrode produced by standard hand painting with subsequent hot-pressing and proton exchange step; right: proton form sprayed ink without subsequent steps.

The TBA form ink was introduced by Wilson et. al to render the catalyst layers more durable [90]. Since the strategy to fabricate G-IV segmented anodes employed catalyst inks in proton form, rather than TBA form, endurance tests at fairly aggressive operating conditions were performed. Constant current densities ranged from 0.75 A/cm^2 to 1.0 A/cm^2 to obtain an initial cell voltage of 0.5 V, and to challenge the electrodes with high current throughputs and high reaction water production. Strong differences in endurance behavior were observed for proton form sprayed electrodes when operated as cathode or anode, indicating that performance degradation mainly occurred at the cathode. This might have been related to presence and production of water and vulnerability of the crystallinity of the ionomer in the catalyst layer with respect to water [103]. The MEA configuration as used in the hydrogen powered G-IV segmented cells lost only 26 mV cell voltage over the course of 710 hours (~4 weeks). MEAs of this type can consequently be operated at high current densities for several weeks or at less challenging operating conditions even longer, without the need to be concerned about significant impact of aging processes on the spatial information measured.

G-IV, DMFC

Segmented MEAs for DMFC operation were manufactured with G-IV geometry using the standard production method for DMFCs at LANL. Catalyst inks contain 5% Nafion solution (1100 EW, Solution Technology, Inc.) and unsupported catalyst material (Johnson Matthey). Anode ink composition was 85 wt% 1:1 platinum-ruthenium catalyst and 15 wt% Nafion solution. Cathode ink composition was 90 wt% platinum catalyst and 10 wt% Nafion solution. After sonicating the ink components for about 90 seconds, the produced catalyst ink was directly hand painted on a Nafion 117 membrane of 75°C. The painted electrode was then dried for at least 20 min at the same temperature. The geometries for hand painting were transferred using templates cut of fiber glass

reinforced silicon, in the G-IV pattern described earlier. The cathode was loaded with 6 mg Pt/cm^2, while the ten segments of the anode were coated to a loading of 10 mg Pt-Ru/cm^2. Modest reproducibility was achieved with segments deviating in average 9% from the mean catalyst loading.

Standard testing of unsupported Pt and Pt-Ru DMFC electrodes at LANL revealed that the catalysts are free of contaminants after MEA production and do not require cleaning prior to operation [104]. Pivovar et. al. performed endurance tests of such MEAs in a DMFC stack and quantified the average anode performance loss via anode polarization measurements [105]. The current density at 0.3 V dropped 14% after 120 hours and 19% after 339 hours, respectively. Supplement cyclic voltammetry (CV) experiments suggested that one possible loss mechanism in the system was loss of active catalyst surface area on the anode as a function of time. To counteract any changes of the catalyst surface area and its performance, operating time of segmented DMFCs was kept minimal.

3.3 PEFC Operation

Unless mentioned, segmented PEFCs were operated at the following standard G-IV (G-III) hydrogen conditions. Water temperature of the humidifier and gas flow rate determine the amount of water uptake in the humidifier. Typically humidification close to 100% saturation for a given temperature can be achieved with small gas flows. However, for high gas flows, the saturation can decrease to as low as 70% [58]. Standard humidifier temperatures for the anode and the cathode were 105°C (80°C) and 90°C, respectively. The operating temperature of the cell was maintained at 80°C. Back pressures for both the anode and the cathode were set at 2 bar. Gas flows were controlled by electronic mass flow controllers (MKS, RS 485), which were adjusted for the atmospheric pressure and the temperature at the laboratory. The anode was operated on hydrogen at a fixed gas flow of 810 sccm (800 sccm). The cathode was typically operated with a fixed air flow of 4000 sccm (4400 sccm).

The pressure drop per segment was 0.015 psi and 0.05 psi for anode and cathode, respectively. Taking the pressure dependence of the anode and cathode reaction into account, both values were considered negligible and the pressures along the flow-fields were regarded as constant.

Four way valves were connected to the piping system of anode and cathode in such a way, that they allowed reversal of the gas flows of one or both electrodes during operation. Standard flow direction was co-flow configuration, downwards from flow inlet to flow outlet.

Between measurements, the fuel cell was operated at a constant cell voltage of 0.6 V. Prior to polarization and transient experiments platinum oxides that may have developed on the platinum catalyst surface were removed by pulsing the cell voltage to 0.3 V for 5

seconds. Transient measurements were recorded by averaging about 300 data points every 0.055 seconds, while polarization measurements averaged 1000 data points after keeping the cell voltage constant for 30 seconds.

3.3.1 Polarization Measurements

The homogeneity of the performance potential of each G-IV segmented MEA was verified, after break-in and cleaning, by performing polarization measurements with only one segment connected at a time. **Figure 13** shows a typical set of polarization curves of individually operated segments measured after operating each segment at 0.5 V for 30 minutes. The performances and HFRs of the single segments were nearly identical confirming the reproducibility of the MEA fabrication process. The HFR values were close to $R_{\square} = 0.120\ \Omega cm^2$, which is a typical HFR value for well-humidified Nafion N1135 MEAs.

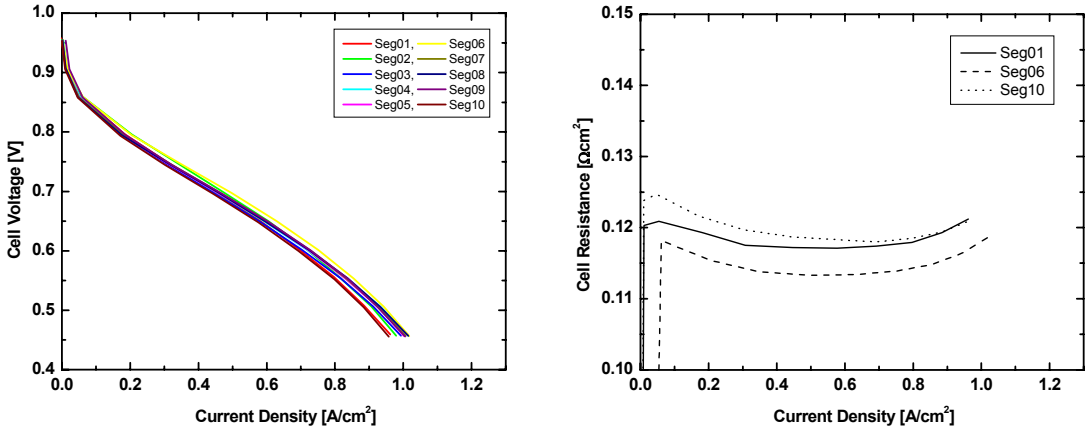

Figure 13: Polarization curves and HFRs of PEFC segments operated individually at identical operation conditions. While one segment is operating, the other segments are disconnected.

Figure 14 shows the performance characteristics of each segment of the segmented cell when all segments are in operation. The left part of Figure 14 shows the current distributions of the segments beginning with Seg01 at the rear of the plot and moving forward sequentially. The polarization curves are different for each segment, because the local operating conditions vary along the flow-field. This effect is especially notable in the high current density region of the cell where the performance decreased with each successive downstream segment. This was caused by increasing mass transport limitations along the flow channel due to the decreased concentration of oxygen and increased concentration of water in the flow stream, resulting from the upstream electrode reactions.

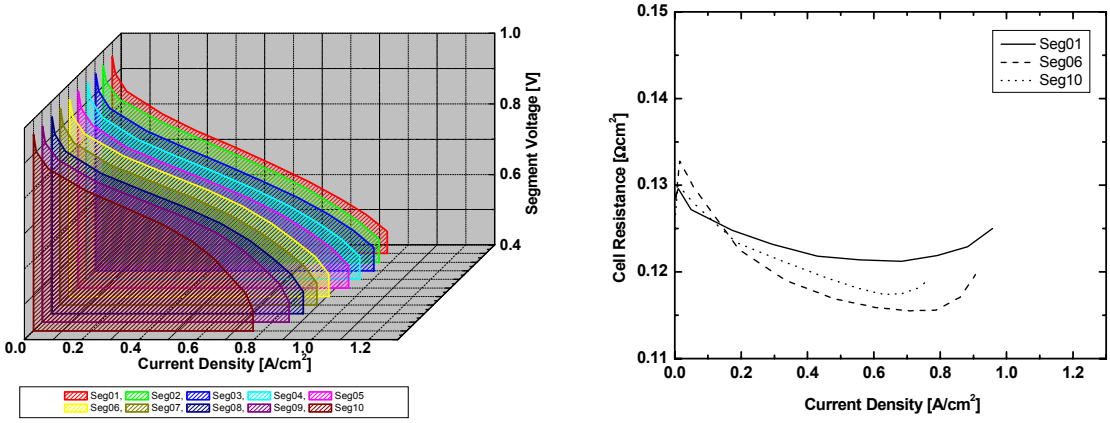

Figure 14: Left: Waterfall graph of the segmented PEFC showing the current distribution along the flow-field. Right: HFRs of the segmented cell recorded during measurement of the polarization curves.

During cell operation HFRs were also recorded for every segment and operating point. The HFRs values for Seg01, Seg06, and Seg10 are shown in the right part of Figure 14. The HFR of the segments was higher in the kinetic region of the polarization curves. Since the cell was operated with very high gas flows, the gas saturation level with water was less than 100% and the cell operated under somewhat dry conditions. At intermediate current densities, between 300 to 800 mA, internal hydration resulting from electrode reactions compensated for the lack of external humidification causing the HFR to decrease to about $R_{\square} = 0.120\ \Omega cm^2$, the expected value. At high current densities, above 800 mA, the HFRs of the segments increased again, probably due to an increasing water drag through the membrane causing the anode catalyst layer to dry out slightly. Note that Seg01 showed the highest stability of the HFRs. In the kinetic region Seg01 had a HFR of $R_{\square} = 0.127\ \Omega cm^2$ that decreased to $R_{\square} = 0.121\ \Omega cm^2$, and at high currents finally increased again to $R_{\square} = 0.125\ \Omega cm^2$. This segment was exposed to the most constant level of gas humidification due to its position closest to the gas inlet of the fuel cell hardware. Hence, the resistance only changed with the production and transport of water within its own active area. The subsequent segments, e.g. Seg06, present larger HFR changes. The HFR of Seg06 decreased from a higher resistance of $R_{\square} = 0.133\ \Omega cm^2$ to a smaller resistance of $R_{\square} = 0.116\ \Omega cm^2$ due to the production of reaction water in the upstream segments. The increase of the HFR to $R_{\square} = 0.120\ \Omega cm^2$ at high current densities was identical to the increase of the inlet segment Seg01, indicating that the anode was insufficiently humidified at high current densities.

Figure 15 shows the comparison of segments Seg01, Seg04, Seg07, and Seg10 to their baseline curves. While segment Seg01 shows no changes with respect to the reference curve, the segments further downstream deviated from their baseline performance. At higher current densities the segments started to pay a performance

penalty. The more segments preceding a given segment, the higher the penalty due to fuel utilization and mass transport limitations. At small current densities below about 500 mA/cm^2, the performance of segment Seg10 benefited from the reaction water produced upstream. This increase was rather small and may as well have been within the range of measurement accuracy.

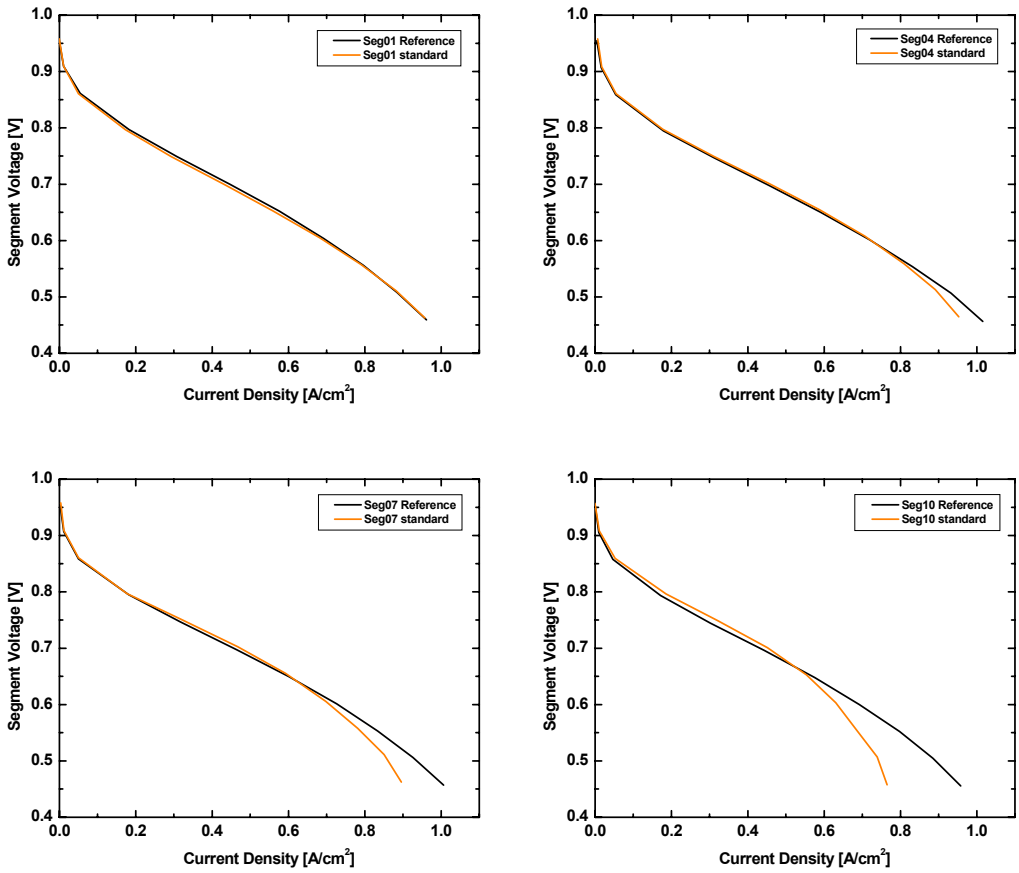

Figure 15: Comparison of reference measurements (only one segment operating) with standard operation measurements (all segments operating) for PEFC Seg01, Seg04, Seg07, and Seg10.

Figure 16 shows the same data set from a different perspective. It presents the current densities of the cell for the reference and standard operation modes at different cell voltages. This presentation visualized the shift of the onset of mass transport limitation with increasing current density. At low current densities in the kinetic region and the beginning of the ohmic region below about 500 mA/cm^2, reference and standard measurement values were identical. At higher current densities the measurements values deviated due to the onset of flooding of the gas diffusion layers. The higher the current density was, the earlier the deviation occurred and the stronger it developed downstream.

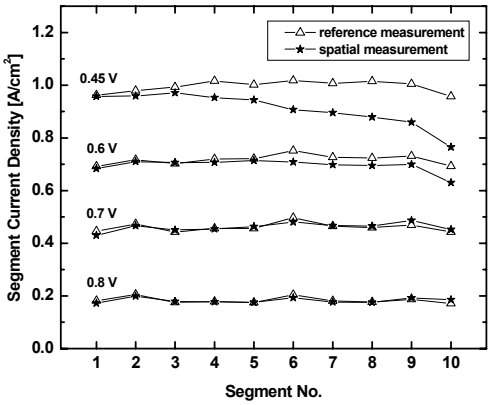

Figure 16: Comparison of performance distribution of reference measurements and standard operation.

Other spatial polarization measurements focused on the break-in process and the impact of cell operating conditions on PEFC performance, such as anode and cathode humidifier temperatures, anode stoich, cathode flow rate, and co- or counter flow configuration. These measurements, which are presented in the Appendix and whose results are summarized in the following paragraphs, helped to develop strategies to distinguish between (i) anode and cathode processes, and (ii) cause and effect of processes. They were further helpful in determining the standard operating conditions used in this work.

The spatial break-in measurements revealed that the time needed for initial start up of a fuel cell hydration was accelerated with the amount of water present. The expected resistance changes in the catalyst layers could not be observed *in situ*, they were negligible with respect to total cell resistance.

Variation of anode and cathode humidification parameters showed strong impact on local cell performance and resistance. Both anode and cathode hydration interacted, and cannot be separated easily. It appeared necessary to optimize both parameters with respect to each other, the cell temperature, and the chosen operating point or range of operating points. The segmented cell allowed furthermore insight in processes, which would be very difficult to detect with single cell technology. A long-term operated test cell suggested that the magnitude of ripening of a fuel cell catalyst depended on its exposure to water.

Variation of hydrogen stoichiometric flow rates showed little impact on performance distribution. The observed performance changes were caused by changing the humidification of the gas stream due to increased anode flow rates. High cathode flow rates changed the performance distribution in the kinetic region and in the region of concentration polarization. Performance drops were observed that were identical to those of an improperly humidified cell. At low current densities the cell failed to compensate

for the decreasing saturation of the gas at large flow rates. This resulted in dehydration of the anode catalyst along the flow-field. High cathode flow rates also decreased mass transport limitations of the cell.

Counter-flow measurements with the segmented system refuted predictions in the literature that this configuration was capable to better preserve water within the cell. The reversal of the flow was found to be a very valuable instrument to separate and identify anode and cathode effects and improved insight into fuel cell processes.

3.3.2 Transient Measurements

Transient measurements were performed using G-III and G-IV segmented setup. The G-III setup was used in a single set of measurements to record total cell response to exposure to CO as a function of CO partial pressure. Spatial CO transient measurements were performed with the G-IV system to investigate cell response to exposure to and withdrawal of CO as a function of time and position along the flow-field. Anode piping was extended as shown in the schematic of **Figure 17** to allow effortless switching from pure to contaminated fuel. The inlet consisted of two individual gas feeds, one for the pure hydrogen gas, the other for hydrogen contaminated with CO (H_2/CO). It contained inlet pressure gauges and pressure release valves for each feed line.

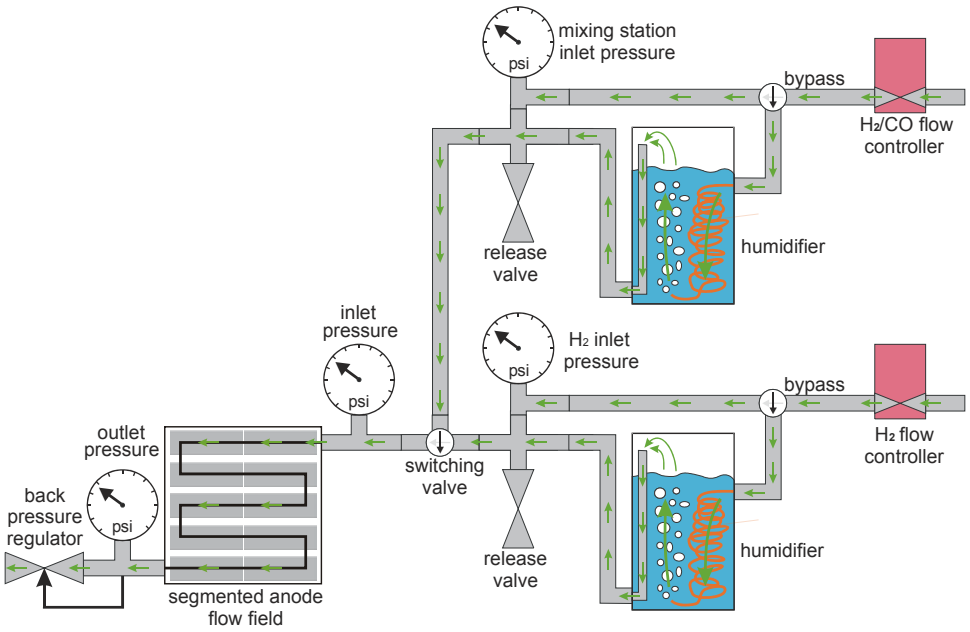

Figure 17: Schematic of CO transient measurements setup for fixed CO partial pressures.

At the beginning of each transient measurement, the cell was operated with humidified pure hydrogen for 1 minute at a constant cell voltage of 0.6V. In the meantime, the H_2/CO line was first purged, and then pressurized to the hydrogen inlet

pressure. Poisoning of the cell was initiated by switching the gas source from the H_2 line to the H_2/CO line. The release valves were used for avoiding over-pressurization of the inlet lines. They allowed switching back to pure hydrogen in the same manner, for testing cell recovery with neat H_2.

Transient measurements were performed with the G-III segmented setup employing G-III standard operating conditions. G-IV standard operating conditions applied to all experimental variables of the spatial transient measurements, except for the anode flow rate. The anode was operated on hydrogen at a fixed initial stoichiometric ratio (λ) of 1.1, and 1.5, calculated for the total cell current of the uncontaminated G-IV cell at 0.6 V. Operating conditions other than standard are explicitly defined in the text.

Transient data is presented either as measured or in normalized form. For normalization, cell current and segment currents were individually averaged over the course of the first minute during operation on pure hydrogen. Subsequently, the measured cell current and segment currents were divided by their averaged value, generating a normalized current value independent of local segment performance.

3.3.3 Cyclic Voltammetry of the Segmented Anode

Cyclic voltammetry was performed to probe anode activity and to detect potential presence of surface contaminants [106]-[107]. Prior to voltammetric experiments, the standard fuel cell operation was interrupted and inert gas (argon or nitrogen) instead of hydrogen was fed into the fuel cell anode. From then on the cell was operated in an externally driven mode, with fuel cell anode operated as a working electrode. Hydrogen was injected to the original fuel cell cathode to be used simultaneously as the counter and reference electrode for potentiostatic control. For that purpose, the cathode was first carefully purged with the inert gas to remove possible traces of the air, and then fed with hydrogen-gas at 600 sccm to maintain humidification and constant H_2 activity. This helped to limit variations in the reference potential of the electrode to those associated with, however small, kinetic overpotential of hydrogen evolution or hydrogen oxidation.

Cyclic voltammetry was recorded with a PAR Model 172 potentiostat/galvanostat and an EG&G PARC Model 175 universal programmer. The data was stored on a MacIntosh G3 computer using acquisition procedure written in LabView.

Cyclic voltammetry was routinely used to determine the degree of anode poisoning with gaseous CO. In these experiments, trace amounts of CO were added to either hydrogen or nitrogen feed stream to the anode and allowed to interact with the Pt catalyst for between 1 - 60 minutes. The amount of chemisorbed CO was then determined in a single voltammetric stripping scan, typically carried out in the potential range from 0.1 to 0.9 V. The effect of CO on the fuel cell performance was determined by recording cell polarization plots and transient response plots under various operating conditions of the cell. A complete recovery of the CO-exposed anode was assured by performing a 10% air bleed into the hydrogen feed in between experiments [108].

Figure 18 shows the first two CV cycles of a cell segment after the exposure to 100 ppm CO for two minutes. As a result of the specific test conditions used in this work, the CV scan shown in Figure 18 was shifted positive of the zero-current line in the entire applied potential range. This current offset originated from molecular hydrogen diffusing (H_2 crossover) from the counter-reference electrode across the membrane to the test electrode and undergoing an immediate oxidation at the anode potentials. The offset magnitude depended on the membrane type and thickness, as well as the cell operating conditions, such as relative gas pressures, temperature, and CV scan rate. The described phenomenon, which can be referred to as hydrogen crossover, represented a source of possible error in the CO charge determination to be considered in data analysis.

The CO stripping charge, Q_{CO}, is given by the integral of the peak area divided by the used scan rate, v:

$$Q_{CO} = \frac{1}{v} \int_{peak} I(E)dE \tag{15}$$

Here, I is the measured current, and E the electrode potential.

The "two-baseline" method selected for the determination of the CO stripping charge allowed to account for the change (increase) in the double layer capacity during CO oxidation (Figure 18, grey area). It also allowed to make this measurement independent of the hydrogen crossover, which, as a mass transport controlled process, depended on the scan rate. Finally, the integration method used accounted for that part of the CO-stripping charge that overlapped the oxide layer formation charge at high scan rates (Figure 18, black area).

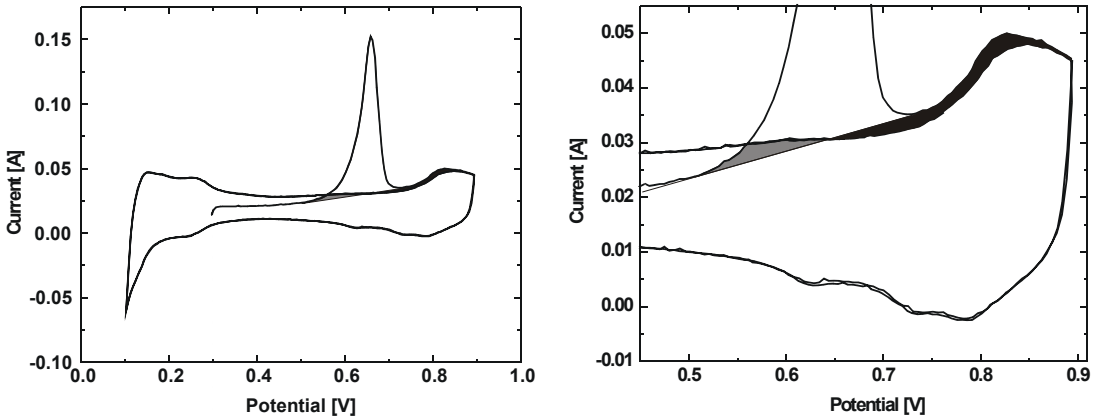

Figure 18: First and second voltammetric scans of an anode segment after the exposure of the cell to 100 ppm CO for 2 min. Figure shows the principle of the "two-baseline" method selected for CO stripping charge determination. Scan rate: 100 mV/s.

The left side of **Figure 19** shows cyclic voltammograms recorded at various scan rates for an anode segment poisoned with 100 ppm CO for 2 min. To determine the optimum scan rate for CO stripping, surface coverage of CO was evaluated as a function of scan rate for the selected integration method. CO coverage was calculated from the stripping charges in Figure 19, assuming linear form of CO at the surface (Pt=CO). The coverage data are shown on the right side of Figure 19 as a function of scan rate ranging from 10 to 500 mV/s. The results showed an increase of the measured CO charge with decreasing scan rate, indicating increasing contribution of hydrogen crossover. This influence of hydrogen crossover on the measurement was negligible for scan rates of 50 mV/s and higher. In the following, all measurements were performed at an intermediate scan rate of 100 mV/s, which offered minimal possible error without underestimating the measured stripping charges.

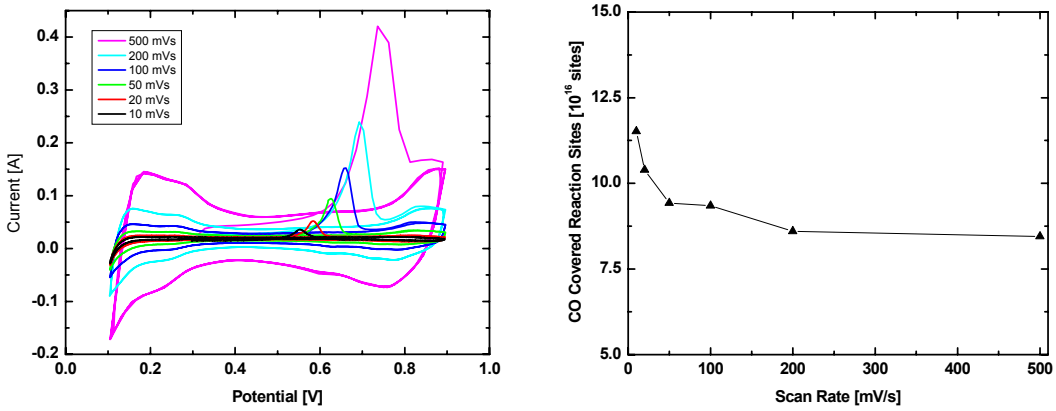

Figure 19: Left: Voltammetric stripping of CO from a single cell segment at different scan rates. The cell was exposed to 100 ppm CO for two minutes. Right: Number of sites covered by chemisorbed CO as a function of scan rate.

Cyclic voltammetry of the inlet, middle and outlet segments of the anode (Seg01, Seg09, Seg18, respectively) after the exposure to 100 ppm CO for 10 minutes, in the presence of 100 ppm CO in the feed stream is shown in **Figure 20.** Because of the continuous presence of CO in the gas flowing through the cell, a small CO stripping peak was observed in second CV cycles. This was indicative of an immediate partial re-poisoning of the catalyst after the removal of surface CO in the first cycle.

Initial CVs of the CO-poisoned surface showed no hydrogen adsorption (currents close to zero between 0.1-0.4 V on each first scan) and were identical for all three segments up to 0.5 V, i.e. to the onset of CO oxidation. Following CO removal at a potential of about 0.8 V and throughout the remaining part of the scans the magnitude of the current offset due to the hydrogen crossover (see above), depended on the segment location in the flow field.

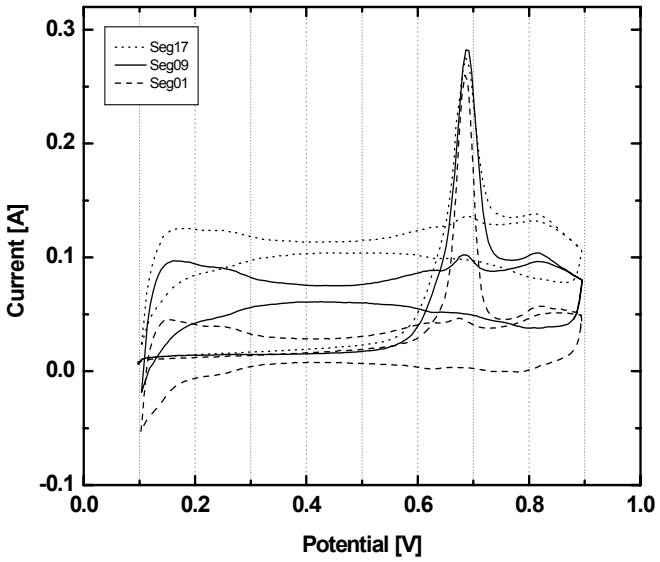

Figure 20: First and second CV scans for Seg01, Seg09, and Seg17. 100 ppm CO present during the experiment.

Plotting hydrogen crossover current as a function of the segment number yielded a straight line, such as the one in **Figure 21**. The linear increase in the crossover current resulted from carryover of hydrogen that had crossed the membrane upstream of a given segment. Hydrogen crossover experiments revealed that about 40% of the hydrogen crossing from the cathode to anode side of the cell, rather than getting immediately oxidized, became carried over into the flow channel and, consequently, may have been oxidized downstream from the crossover point. At a CO saturated surface this hydrogen contributed about 1.4 mA/cm^2 of the surface area upstream of the measured segment to the CV current of the segment under investigation.

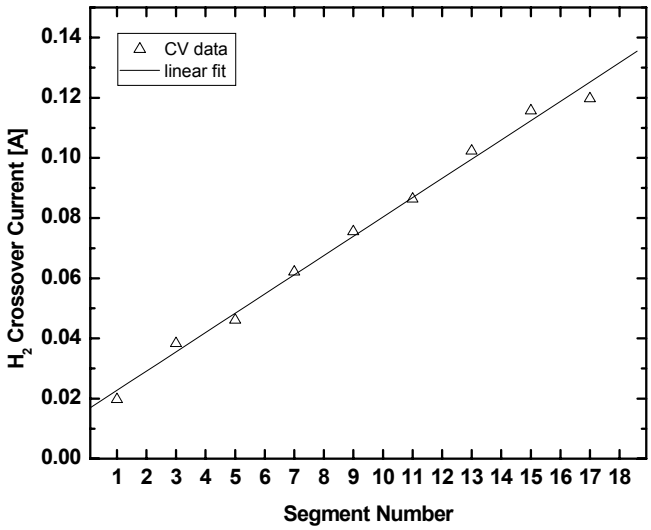

Figure 21: Hydrogen crossover current as a function of segment number. Crossover for every segment estimated by averaging CV current at 0.45 V for the positive- and negative-sweeping scans.

To account for this measurement artifact, the hydrogen had to be dissociated at the crossover point. This required the removal of all surface CO from all segments except the measured segment. This was done by applying a voltage of 0.75 V to the non-measured segments, and stopping the CO flow to the anode. The only remaining contribution of hydrogen crossover to the measured segment's current was due to hydrogen crossover at that segment. The corresponding current density was found to be a consistent 4 mA/cm^2.

Figure 22 shows voltammetric stripping of CO from the inlet, center, and outlet segments of the anode (Seg01, Seg09, Seg18) after the exposure to 100 ppm CO for 6 minutes. Thanks to the approach as described above, virtually all interference from hydrogen crossover was eliminated. In the following, all the presented measurements were performed using this new method.

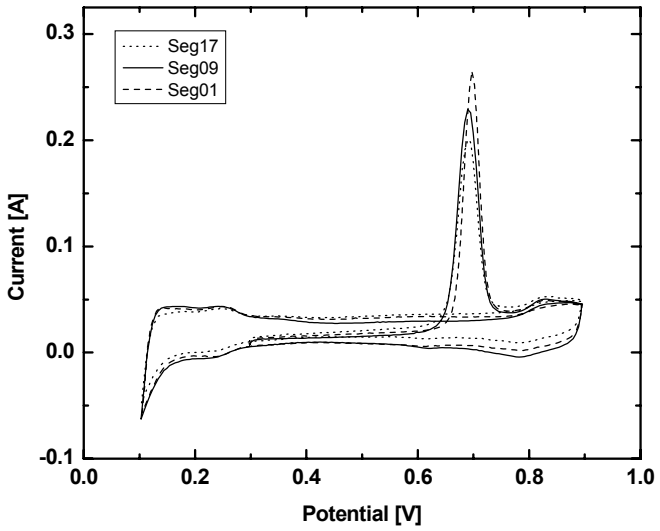

Figure 22: CO stripping from Seg01, Seg09, and Seg17, after poisoning with 100 ppm CO for 6 minutes. The voltammograms show the effect of the experimental approach eliminating the effect of hydrogen crossover on the measured voltammetric currents.

3.4 DMFC Operation

Prior to operating segmented DMFCs with a methanol solution, the cells were broken-in employing hydrogen as a fuel. This allowed for short break-in periods and evaluation of the cathode, which is the dominating loss factor of the cell during hydrogen operation. For break in and testing in hydrogen mode, the anode was operated at 600 sccm hydrogen flow, 2 bar backpressure, and 105°C humidifier temperature. The cathode operated at a fixed air flow which delivered 2 stoich for a current of 64 A, the total cell current observed at a cell voltage of 0.4 V. Backpressure was 2 bar and humidifier temperature 90°C. The cell was operated at 80°C.

Identical to MEA evaluation of segmented PEFC, individual segment polarization curves were performed to study performance homogeneity. This was done in hydrogen and methanol operating mode and compared to regular segmented DMFC operation. After switching to methanol operation DMFC experiments were performed at the following G-IV standard DMFC operating conditions, meant to simulate reasonable operating conditions in a practical device. The anode was fed with 10 mL/min of 0.48 M methanol (MeOH) solution, preheated to 80°C in a continuous-flow heater built in-house. Anode flow was controlled by a high-pressure liquid chromatography pump (Shimadzu LC-8A). Cathode air flow was maintained at a stoichiometric ratio of $\lambda = 2.5$ throughout the entire current density range. Cathode stoich was corrected for consumption due to methanol crossover employing a model introduced by Ren et. al. [109]. Stoichiometry in

this case represents the ratio of air provided to the cell to that necessary to oxidize the crossover methanol and reduce protons. The standard cathode was operated at ambient pressure and non-humidified flow. When humidified, standard humidification occurred at 75°C. Employed cell compression and G-IV flow-field design were used as optimized for hydrogen operation to avoid challenging adjustments and to maintain the integrity of the operation. Occurring difficulties of sealing the cell during DMFC operation were solved by increasing the compression of the hardware.

3.4.1 Anode Polarization Measurements

Once the anode was switched to methanol fuel, the loss mechanisms of methanol oxidation increased to about the magnitude of the cathode losses. Anode performance limitations were isolated and quantified using anode polarization measurements, either performing individual measurements by connecting one segment at a time or measuring all segments together. **Figure 23** shows the principle of such an anode polarization experiment. The cell was operating in driven mode, using the power supply of the segmented cell setup, controlled by the electronic load, as driving power source to create current flows in standard fuel cell direction. Identical to DMFC operation, methanol solution was fed into the anode, while well humidified hydrogen was supplied to the cathode, which will be referred to as counter or reference electrode. This electrode was established with a constant hydrogen flow of 1000 sccm, a humidifier temperature of 85°C, and a pressure of 0.67 bar gauge pressure. If not mentioned otherwise, standard operating conditions were used at the anode.

The application of a potential difference between anode and counter electrode in such a setting activates methanol oxidation according to equation (13). The produced protons are driven through the proton conducting membrane, to recombine with electrons to molecular hydrogen at the counter electrode.

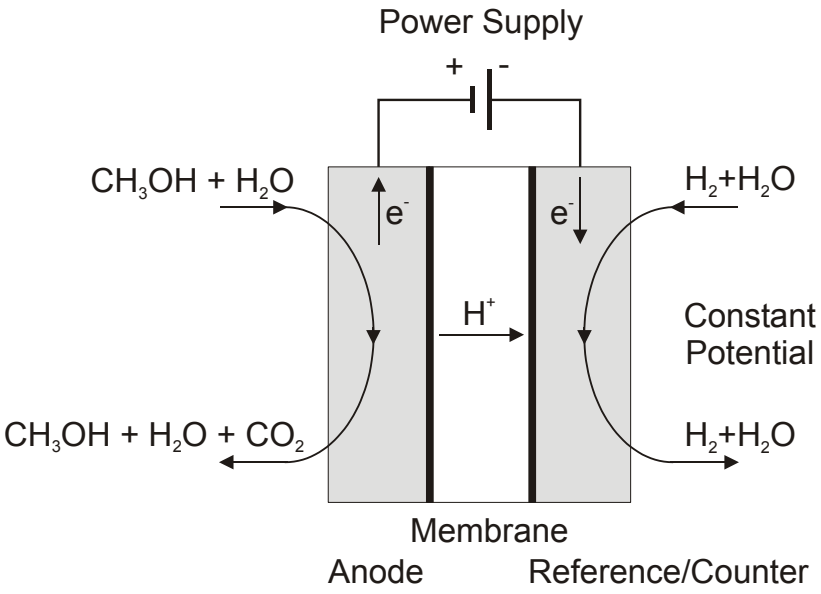

Figure 23: Schematic of anode polarization measurement.

The amount of reacting methanol is dependent on active catalyst area, catalyst composition, applied potential, anode transport processes, etc. Cathode loss mechanisms are decoupled by the fast reactions occurring at the counter electrode and with increasing potential, the recorded current is limited by the maximum achievable anode performance. Measurements create a current plot similar in shape to the one shown in **Figure 24**. The recorded limiting current directly determines the anode limitations of the fuel cell in-situ.

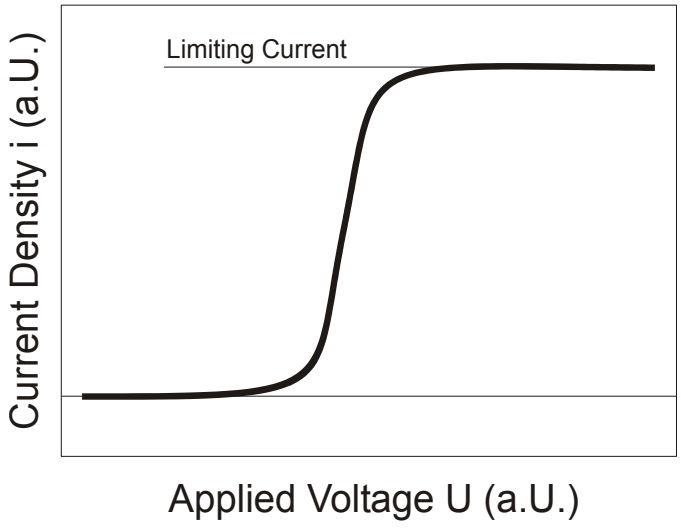

Figure 24: Characteristic trend of an anode polarization measurement plotted as cell current density versus applied potential.

3.4.2 MeOH Crossover

Simultaneous to increasing anode losses by switching from hydrogen to methanol operation, cathode losses significantly increase due to methanol crossover. The quantity of crossing methanol depends on operating conditions and system parameters, e.g. methanol concentration, flow rate, temperature, membrane material, membrane thickness, backing material, cell compression, and flow-field. Investigation of the methanol crossover rate is a viable method for determining the selective properties of the polymer membrane material and the involved electrochemical losses. The measurement strategy employed in this work was introduced by Ren et. al. [109]. It allowed monitoring the methanol permeation across G-IV segmented DMFC MEAs via voltammetry at open circuit configuration. This 'worst case scenario' recorded the maximum methanol flux for the given operating conditions. The methanol crossover rate can be determined from the recorded limiting current by correcting for the effect of fluid convection within the membrane by electro-osmotic drag of the protonic current [109]. At operating conditions other than open circuit, the fuel cell reaction, consuming methanol, decreases the methanol concentration at the membrane surface and hence the crossover rate.

Spatial methanol crossover measurements were performed to detect and quantify methanol crossover as a function of segment location and operating conditions. During the experiments as shown in the schematic of **Figure 25** methanol was fed to the anode using standard operating conditions if not mentioned otherwise. Cathode air flow was substituted by 1000 sccm nitrogen, humidified at 85°C. The cell operated in a driven mode, employing a power supply (Agilent 6033 A) as driving power source, which opposed polarity of regular fuel cell operation[1]. Methanol that crossed from the 'fuel cell anode' to the 'fuel cell cathode' was oxidized according to equation (13) by the applied potential. The potential drove a current through the cell of opposing fuel cell current direction, whose maximum was limited by the methanol diffusion rate through the membrane. For measurement, power output was stepped down from 0.8 to 0 V to assure measurement at steady state conditions. Each voltage (increment of 0.01 V) was held for 5 seconds while recording the cell response. Note that since the polarization was reversed, the current flowing through the previously described Hall sensor setup changed direction also. Prior to investigation of the methanol crossover, Hall sensors were recalibrated for 'reversed' current direction and smaller current range.

[1] By switching the polarization of the electrodes, the fuel cell anode becomes the cathode and the fuel cell cathode turns into the anode of the MeOH-crossover cell. For clarity, the term 'anode' will be applied as in the fuel cell case, while the 'cathode' will be referred to as 'working electrode' for MeOH-crossover measurements.

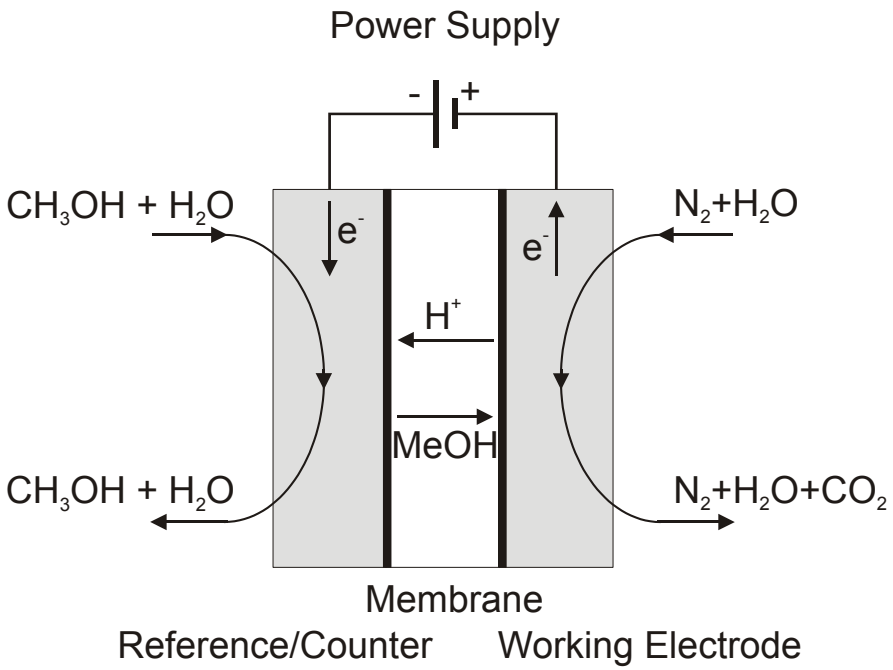

Figure 25: Schematic of methanol crossover measurement.

Although smaller in magnitude, methanol crossover experiment produces a similar plot to that of the anode polarization experiment as shown in **Figure 24**. The maximum current density is limited by methanol diffusion processes through the membrane. It delivers information about the methanol permeability of the membrane material. At lower applied voltage, Methanol is not fully oxidized and the recorded current is no longer mass transport limited. Since no significant information gain was expected from individually performed methanol crossover experiments and segmentation of the cathode electrode would have been necessary, the desired spatial information was exclusively extracted from spatial cell measurements.

4 Results and Discussion

4.1 The Time and Spatial Dependence of CO Poisoning

The performance of a PEFC is strongly affected by the presence of CO in the anode feed. This is particularly problematic when CO partial pressure is transiently increased, such as during a cold-start or in a drive cycle when the reformer/clean-up system is driven away from steady state. To understand in more detail the effects of such transients and to deduce strategies for dealing with them, localized information about the CO poisoning process and the recovery from it is presented and discussed in the next sections.

4.1.1 CO Coverage

Figure 26 shows transient responses of all 18 anode segments of the hydrogen/air fuel cell at 0.6 V to 10, 25, 50 and 100 ppm of CO in the anode feed stream. The CO content in the anode feed stream, rate of current drop, total poisoning time and steady-state current after the poisoning are all listed in **Table 2**. For all four CO contents, the total cell current dropped from an initial value of ca. 54 A to a steady-state value of between 28 and 5.5 A. As expected, higher CO content in the anode feed stream resulted in a faster current drop and lower steady-state current value [110]-[111].

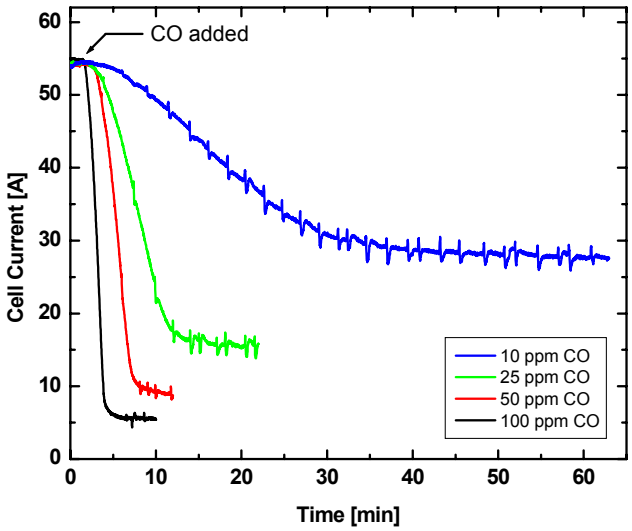

Figure 26: **Fuel cell response to various contents of CO in the anode feed stream. Cell voltage 0.6 V, G-III standard operating conditions.**

Table 2: The effect of CO content in the anode feed stream on cell performance at 0.6 V.

CO Content [ppm]	Average Current Drop Rate [A/min]	Total Poisoning Time [min]	Steady-State Current After Poisoning [A]
10	0.02	50	28
25	0.08	25	16
50	0.19	10	9.0
100	0.39	6	5.5

Under the assumption that CO has a sticking coefficient of one, every CO molecule is adsorbed and trapped on the platinum interface as soon as contact to the catalyst material occurs. For this case, the time period, t, required to develop a monolayer of CO on the surface is given by:

$$t = \frac{n_{Ptsites}}{x_{CO} \cdot f_{in,anode}} \tag{16}$$

Here, $n_{Ptsites}$ is the number of active reaction sites (6.67×10^{18} sites, measured at 25°C), x_{CO} the CO fraction in the anode feed stream (100 ppm), and $f_{in,anode}$ the anode inlet flux (800 sccm). Saturation of the cell was computed to 3.1 minutes for 25°C and 100% coverage, and to 2.6 minutes for 80°C and 85% coverage, respectively. The actual observed saturation time of the cell amounted to 5 min and exceeded the prediction by a factor of two. This indicated a more complex adsorption process at the anode, most probably due to diffusion barriers and/or an average sticking coefficient of less than one.

Voltammetric stripping of carbon monoxide from the surface of Pt nanoparticles in a small 5 cm^2 single cell is shown in **Figure 27**. CO was chemisorbed from two different gases, hydrogen in one case and nitrogen in the other. In both cases, the CO content was 100 ppm and the gas flow was 200 sccm/min. After CO chemisorption, the cell was purged with pure nitrogen for 15 min to remove traces of CO from the gas phase. (No desorption of surface CO during the purging was assumed). Complete CO stripping was achieved in the first scan. A second, consecutive cycle was run to ensure completeness of CO oxidation and to establish a current baseline for the stripping charge determination. The scan rate was 100 mV/s.

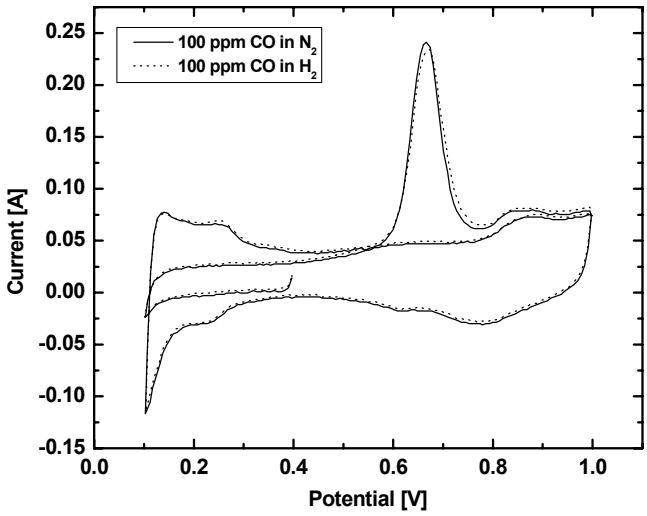

Figure 27: Voltammetric stripping of surface CO in a 5 cm2 cell. CO chemisorbed from 100 ppm CO in nitrogen gas (solid line) and 100 ppm CO in hydrogen gas (dashed line). Scan rate 100 mV/s.

Surface coverage by CO can be estimated based on a model recently proposed by Springer *et al* [111]. According to this model, hydrogen's affinity to platinum is significantly greater than that of nitrogen's. We therefore expected lower CO coverage in hydrogen than in nitrogen, and, consequently, increased electro-oxidation charge of surface CO in nitrogen than hydrogen.

When applied to the conditions of a steady-state CO-poisoning experiment, where hydrogen is present in the anode at open circuit conditions, the current density expressions for hydrogen and CO oxidation become zero (different from the case of an operating fuel cell in [111]), and the model reduces to equations (17) and (18). In order to measure the CO charge of this case, the flow of CO to the anode has to be stopped and the cell purged with humidified nitrogen to remove any traces of hydrogen from the anode side of the cell. The anode potential is assumed to remain low enough to prevent any desorption of CO from the surface. In this case, the CO coverage remains constant, while the hydrogen coverage drops to zero. In other words, after reaching steady state poisoning conditions by CO supplied in hydrogen atmosphere, equations (17) and (18) are valid, while after purging the anode with nitrogen prior to the CO stripping experiment, equations (17) and (19) apply.

When Springer's model is applied to the conditions of a steady-state CO-poisoning experiment where nitrogen is present at the anode, equations (17) and (19) are valid before and after purging.

$$\rho_{Pt}\frac{d\Theta_{CO}}{dt} = k_{fc}x_{CO}P_A(1-\Theta_{CO}-\Theta_h) - b_{fc}k_{fc}\Theta_{CO} = 0 \qquad (17)$$

$$\rho_{Pt}\frac{d\Theta_h}{dt} = k_{fh}x_h P_A(1-\Theta_{CO}-\Theta_h)^2 - b_{fh}k_{fh}\Theta_h^2 = 0 \quad (18)$$

$$\Theta_h = 0 \quad (19)$$

Here, ρ_{Pt} is the molar area density of catalyst sites times the Faraday constant; k_{fh} and k_{fc} the rate constants for hydrogen and CO adsorption, respectively (A/cm^2 atm), b_{fh} and b_{fc} are the reciprocal adsorption constants for hydrogen and CO, respectively (atm), which implicitly represent the desorption rates; Θ_h and Θ_{CO} are fractional coverages by hydrogen and CO, respectively; x_h and x_{co} are mole fractions of hydrogen and CO, respectively; and P_A is the total anode pressure (atm).

An analytical solution for Θ_h and Θ_{CO} can be obtained as shown in equations (20) - (21). These equations are valid during steady-state CO-poisoning. P_{CO} and P_h are the partial pressures of CO and hydrogen, respectively. After purging the anode with nitrogen prior to CO stripping experiment, equation (21) remains valid and equation (20) changes into equation (19).

$$\Theta_h = \frac{b_{fc}\sqrt{P_h}}{\sqrt{b_{fh}}P_{CO} + b_{fc}(\sqrt{b_{fh}} + \sqrt{P_h})} \quad (20)$$

$$\Theta_{CO} = \frac{\sqrt{b_{fh}}P_{CO}}{\sqrt{b_{fh}}P_{CO} + b_{fc}(\sqrt{b_{fh}} + \sqrt{P_h})} \quad (21)$$

In the absence of hydrogen, i.e. nitrogen or argon atmosphere, equation (21) simplifies to:

$$\Theta_{CO} = \frac{P_{CO}}{b_{fc} + P_{CO}} \quad (22)$$

If the rate constants k_{fh} and b_{fc} are independent of Θ_{CO} (no dependence on Θ_h assumed, since the affinity of CO is magnitudes higher), the values for Θ_h and Θ_{CO} can be determined directly from equations (20)-(21), or equation (22), respectively. Otherwise, in case the rate constants are a function of Θ_{CO}, equations (20)-(21) are solved by numerical iteration, under the condition that the function of the rate constants k_{fh} and b_{fc} over Θ_{CO} are satisfied [111]. Surface coverage values for stripping experiments in Figure 27 were calculated employing equations (20)-(21), assuming P_{CO} of 0.3 mbar, P_h of either 3 bar (CO in hydrogen at 3.0 bar$_a$) or 0 bar (CO in inert gas at 3.0 bar$_a$), b_{fh} of 0.5 atm [111]. The adsorption ratio was determined to b_{fc} of $7.75\text{x}10^{-6}$ atm at Θ_{CO} value of 0.92 and $1.03\text{x}10^{-5}$ at 0.97, respectively [111]. Based on that calculation, the CO coverage in the inert gas atmosphere was expected to be higher than in hydrogen (97% vs. 92%, **Table 3**). This result did not agree with the stripping charge measurements in Figure 27. Within the accuracy of charge measurements, which depended among others

on slight, but unavoidable, variations in cell temperature, gas humidification and anode pressure, the actual measured amount of surface CO was found to be independent of the carrier gas used. In other words, under the conditions of the experiment, there was no indication of a lower CO coverage in hydrogen than nitrogen.

Table 3: Percent of CO-covered and free reaction sites in the presence and the absence of hydrogen in the anode feed stream (based on a model by Springer et al. [111])

Anode Feed	CO-Covered Sites [%]	H-Covered Sites [%]	Free Reaction Sites [%]
CO in H_2	92	6	2
CO in N_2 (or Ar)	97	-	3

This indicated that the adsorption rate constant for CO in the hydrogen atmosphere might have been underestimated in the treatment by Springer et. al. [111]. It is also possible that, contrary to what has been assumed in this work, CO desorption occurred during the purging that preceded CV stripping.

The current transient measurements shown in Figure 26 or **Figure 28** represent average poisoning of the anode by CO and do not provide any information on the poisoning of individual segments in the cell. To obtain specific information on the distribution of the CO, I performed CV measurements with individual anode segments at various states of cell poisoning. CO chemisorption was performed using 100 ppm CO in nitrogen or argon. Cyclic voltammograms of individual anode segments were recorded every 60 seconds of the poisoning process, at the times marked by crosses in Figure 28.

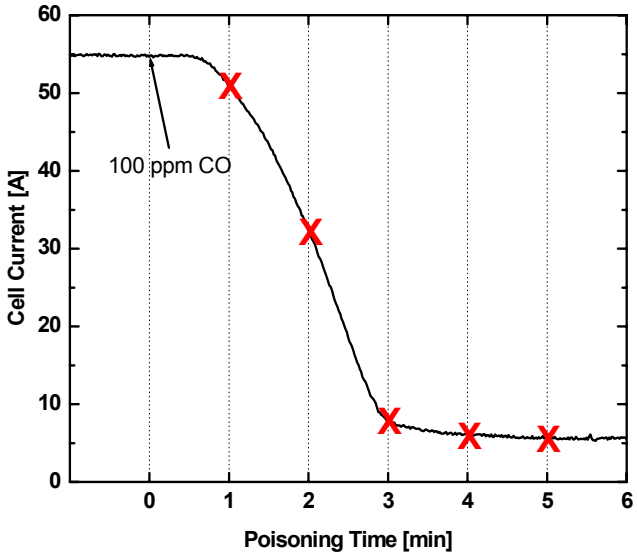

Figure 28: Current time transient with 100 ppm CO injected to the fuel cell anode. CO injected at time t=0. Crosses indicate times at which CVs of individual anode segments were recorded.

Figure 29, **Figure 30**, and **Figure 31** show CO stripping experiments of the odd segments (Seg01, Seg03, ...Seg17) after the exposure to 100 ppm CO for 1, 2, and 6 minutes, respectively. Peak currents and potentials of carbon monoxide stripping from the inlet, center and outlet segments are listed in **Table 4**. After 1 and 2 minutes of exposure to CO, the surface layer of CO was still far from saturation, with CO stripping charges decreasing monotonically from the anode inlet to the anode outlet. CVs recorded after two-minute exposure revealed higher amounts of adsorbed CO. The shift in the peak potential and change in peak current between segments were identical for the two exposure times, indicating similar growth of the CO monolayer during the first and the second minute of exposure to CO. As expected, the amount of surface CO was the highest at the inlet segment and the lowest at the outlet segment.

Low CO stripping charges measured after short poisoning times were accompanied by decreasing CO stripping peak potentials. This indicated that at low coverage CO was less strongly bound to the Pt sites than at higher coverage. Marković et. al. [112] reported two different forms of CO adsorbed on Pt(111) with surface bonds of different energy and oxidizing at different electrode potentials. The oxidative removal of CO_{weak}, which exists at high CO coverage, is accompanied by simultaneous relaxation of the CO catalyst layer. The remaining CO assumes a new bonding state at a CO coverage of ~ 60%, characterized by higher energy of the surface bond. However, infrared data obtained with carbon-supported platinum nanoparticles, by Park et. al. indicate decreasing bonding strength with decreasing CO coverage [113]. The above presented data led to the

conclusion that low- and high-coverage binding on a nanocrystalline fuel cell catalyst reverses the trend typically observed on low-index planes, i.e. (111), (110), and (100). High CO coverage limits the mobility of CO on such a catalyst surface and limits the access of water required for the oxidation reaction to take place. The activation energy consequently increases, resulting in higher CO stripping peak potentials at higher CO coverage.

Further increase in CO exposure times beyond two minutes led to an increase in CO stripping charges until the catalyst surface was completely covered by a monolayer of CO. Based on the transient in Figure 28 complete anode saturation was expected after five-minute exposure to CO. Individual segments became saturated sooner, in a consecutive segment order along the flow-field. CO stripping data recorded after six-minute exposure to CO are shown in Figure 31. The differences in the CO stripping peak area, potential and current for different segments virtually disappeared. Only slight random differences between CVs for various segments could be seen, which were ascribed to variations in catalyst loading, temperature [114], and hydration [115] of individual segments.

Table 4: CO stripping peak potential and current at various anode segment after different poisoning times.

Poisoning Time [min]	Segment	Peak Potential [V]	Peak Current [A]
1	Seg01	0.69	0.18
1	Seg09	0.66	0.10
1	Seg17	0.63	0.04
2	Seg01	0.71	0.24
2	Seg09	0.68	0.17
2	Seg17	0.67	0.08
6	Seg01	0.70	0.27
6	Seg09	0.69	0.23
6	Seg17	0.69	0.20

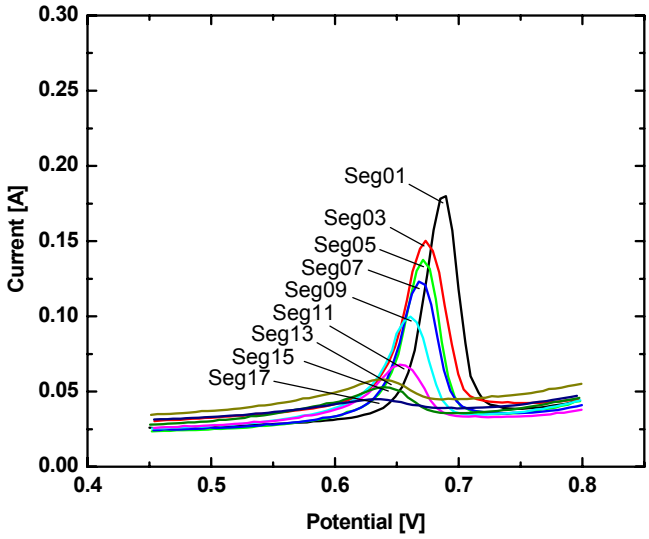

Figure 29: **CO stripping voltammetry from the odd-number segments of the anode following the exposure to 100 ppm CO for one minute.**

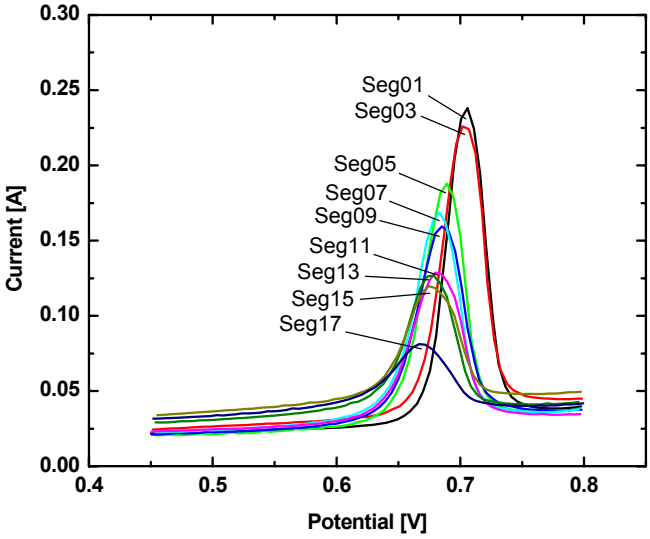

Figure 30: **CO stripping voltammetry from the odd-number segments of the anode following the exposure to 100 ppm CO for two minutes.**

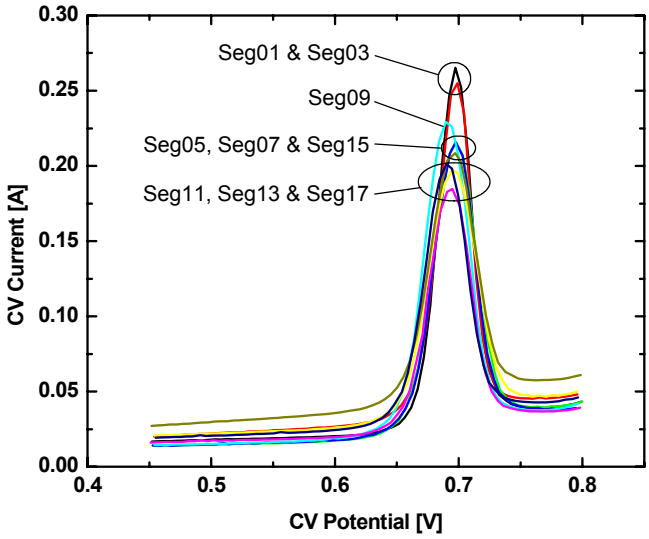

Figure 31: CO stripping voltammetry from the odd-number segments of the anode following the exposure to 100 ppm CO for six minutes.

In order to accurately determine spatial distribution of CO at the anode catalyst, it was necessary to know the number of accessible surface Pt sites. Rotating disc electrode measurements by Igarashi et. al. revealed that 100% coverage with CO at 26°C is reached at CO partial pressures as low as 10 ppm CO, with the desorption of adsorbed CO being entirely negligible [116]. **Table 5** contains CO stripping data obtained using a 5 cm^2 fuel cell setup. In each measurement, the cell was poisoned for 5 minutes at a flow rate of 20 (sccm/min)/cm^2, 2 bar backpressures and ambient cell temperature. The CO stripping charges proved independent of partial pressure in the range from 100 ppm to pure CO, suggesting full saturation of the catalyst with CO irrespective of the partial pressure applied. In the end, the reference charge of the fully CO-saturated segmented anode was measured at ambient cell temperature, 2 bar backpressure, nitrogen flow of 10 (sccm/min)/cm^2, poisoning time of 60 minutes, and CO partial pressure of 250 ppm. These operating parameters exceeded the determined amount of CO required to cover the surface by approximately 15 times. Saturation CO charges were measured for all anode segments and used as reference in the surface coverage measurements.

Table 5: CO stripping charges from a 5 cm^2 anode measured with various CO partial pressures at 25°C and 2 bar backpressure. CO poisoning time: 5minutes.

CO Partial Pressure [ppm]	Poisoning Time [min]	Flow Rate per Unit Area [(sccm/min)/cm^2]	CO Charge [As]
100	5	20	0.35
250	5	20	0.35
1000	5	20	0.34
10^6 (pure CO)	5	20	0.35

Table 6: CO coverage and coverage gradients of the segmented cell and individual segments for various poisoning times.

Poisoning Time [min]	Last Saturated Segment [Seg No.]	CO Coverage of Seg01 [%]	CO Coverage of Seg09 [%]	CO Coverage of Seg17 [%]
1	-	54	30	9
2	3	82	58	35
3	11	76	74	60
4	15	81	79	76
5	17	82	79	86
6	17	86	80	86
60	17	85	85	88

Figure 32 presents the CO coverage of different cell segments after poisoning with 100 ppm CO for different times, including linear fits and standard deviations. The results for three selected segments are summarized in **Table 6**. Poisoning for 5 minutes or longer led to saturation of all segments in the cell at 80°C. The surface CO coverage reached 80 - 85% of the reference values recorded at 25°C. The coverage diminished at shorter exposure time, starting with the segments near the cell outlet. A typical difference between coverage values measured for the adjacent segments was 3-4%, depending on

the anode operating conditions, i.e. velocity of the feed stream, catalyst loading, pressure, etc.. For example, at two-minute CO exposure time the only saturated segments were Seg01-Seg03, with surface coverage by CO dropping along the flow-field from 82% (Seg03) to 35% (Seg17). At even shorter contamination time of one minute no segment was fully saturated. Still, CO coverage decreased along the flow channel by approximately the same per-segment value, from 54-60% at the inlet segment to 9% at the outlet segment.

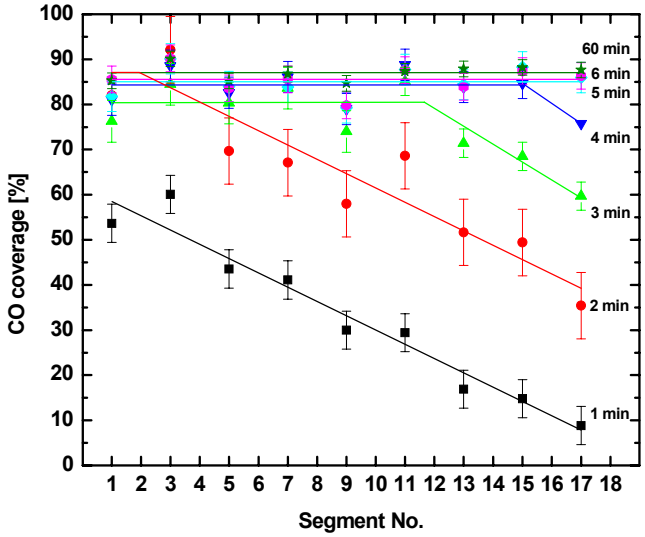

Figure 32: CO coverage as a function of segment position in the cell. Anode catalyst poisoned with 100 ppm CO for seven different times between one and sixty minutes; cell temperature 80°C; and backpressures 2 bar. The symbols represent the data; the lines are linear fits of the data and the error bar the according standard deviations of the fit.

CO poisoning plots for three selected anode segments are shown in **Figure 33.** The graph contains linear fits and standard deviations. The outlet segment (Seg17) showed one minute poisoning delay relative to the center segment (Seg09) and a two minutes delay relative to the inlet segment (Seg01). Parallel poisoning at various segments occurred as a function of segment location rather than sequential saturation of segment catalyst layer after segment catalyst layer.

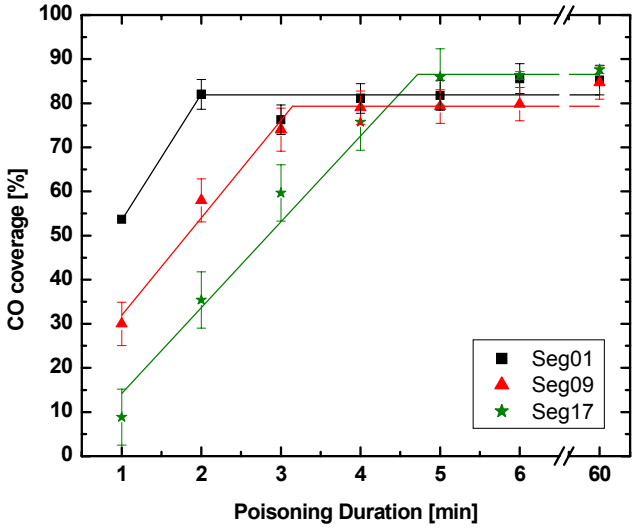

Figure 33: **CO coverage of the inlet, center, and outlet segments as a function of poisoning time. The symbols represent the data; the lines are linear fits of the data and the error bar the according standard deviations of the fit.**

4.1.2 CO Transient Response

Figure 34 shows normalized transient response of G-IV segmented anode at initial stoichs of 1.1 and 1.5. After one minute of cell operation the anode was exposed to 100 ppm CO, which caused the cell current to drop due to CO poisoning of the platinum catalyst. Steady-state conditions were reached after saturation of the catalyst layer with CO. The saturation time for the platinum electrode was dependent on the anode inlet flux and the CO mole fraction, while the current in steady-state conditions was only dependent on the CO mole fraction [110]-[111]. These effects were apparent in the measurements of the cell transients shown in Figure 34. At the initial stoichs of 1.1 and 1.5, the saturation time appeared to be about 10 minutes and 7 minutes, respectively. In both cases, the cell eventually reached the same steady-state current, corresponding to about 23% of the initial cell current.

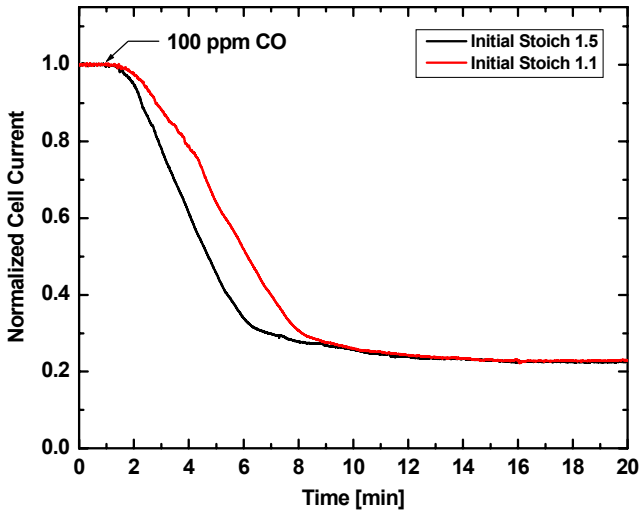

Figure 34: Transient response of a 77.1 cm^2 PEFC to an increase in CO partial pressure from 0 to 100 ppm CO at 1 minute operation time.

Figure 35 and **Figure 36** show, correspondingly, the measured and normalized currents of individual segment currents. Spatial dependence of the CO adsorption process was similar for both anode stoichs. The current of the inlet segment Seg01 dropped first, followed by drops in the other segment currents in consecutive downstream order. The results confirmed the presented CV results, also indicating that gradual poisoning of the fuel cell anode progresses downstream. Lowering the absolute amount of CO supplied to the cell by decreasing the initial anode stoich by 36% from 1.5 to 1.1, lengthened the time interval required for CO saturation of the outlet segment from 12 to 16 minutes; an increase of 33%. As expected, CO adsorption changed linearly with the amount of CO injected into the cell. Smaller amounts of CO resulted in longer time for CO adsorption to progress down the flow-field and delayed segment poisoning downstream.

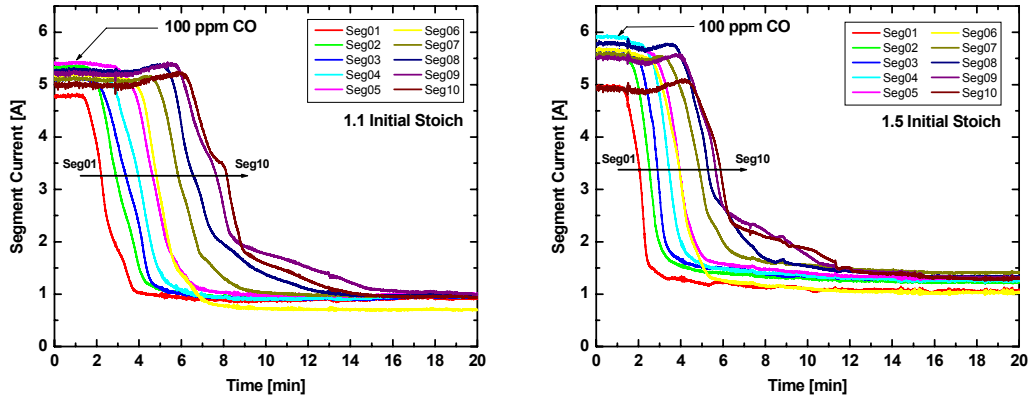

Figure 35: Transient current distribution in response to an increase in CO partial pressure from 0 to 100 ppm CO after one minute of cell operation. Initial stoich 1.1 (left) and 1.5 (right).

Six to eight minutes into the ongoing poisoning process, the performance of segments Seg07 - Seg10 unexpectedly increased. This effect was more pronounced at lower anode flow rates. At the given operating conditions, CO adsorption at the inlet segments caused segment currents to drop and decreased hydrogen and oxygen utilization in the cell. This may have positively impacted operating conditions of the outlet segments for as long as CO adsorption significantly decreased anode performance of the inlet segments only. Simultaneously, production of reaction water decreased and less water diffused across the MEA to the cathode. After onset of cell poisoning, oxygen transport to the reaction sites at the outlet segments may have been facilitated.

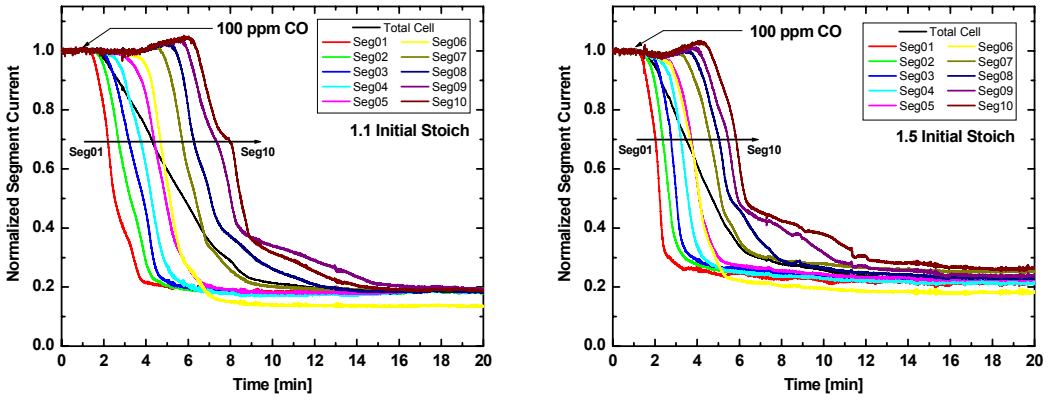

Figure 36: Normalized transient current distribution at initial stoichiometric flows of 1.1 and 1.5.

Figure 37 shows the current distribution at selected times during the CO adsorption process at the initial stoich 1.1. Prior to CO poisoning, all segment currents were fairly identical. After three minutes of exposure to CO, however, large differences in segment

currents developed. Performance was the lowest at the inlet segment Seg01 and increased downstream, up to segment Seg07. Performance of segments Seg07 - Seg10 remained unchanged, indicating that CO molecules had not advanced this far down the flow-field yet. After five-minute exposure to CO, the first four segments were nearly saturated with CO and the differences in segment performance shifted down the flow field. The performance of the outlet segments, still untouched by CO, even slightly increased according to the mechanism discussed earlier. Continuation of the poisoning process eventually led to the saturation of all the segments with surface CO. Total segment current dropped to about 1 A for all segments, indicating steady-state conditions. These data confirmed the results shown in Figure 32 and directly demonstrated the impact of CO coverage on the local current density.

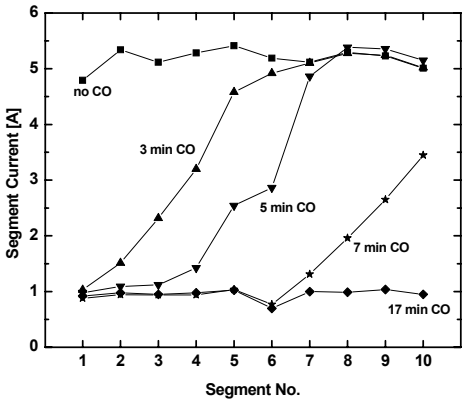

Figure 37: Distribution of segment currents in transient measurement with 100 ppm CO at various poisoning times.

Figure 38 shows measurements of the transient response of all ten segments, performed to identify the origin of the temporary increase in the performance of the outlet segment. During these measurements, the cell operated in standard co-flow air mode, counter-flow air mode, or co-flow oxygen mode. Regardless of cathode conditions, the anode was in all cases exposed to 100 ppm CO after one minute of cell operation. To match the initial current and internal water production occurring with air fed to the cathode, measurements with O_2 were performed at 0.72 V instead of 0.6 V. The cathode feed rate and humidification temperature were kept constant in all three cases. Cell operation in the counter-flow air mode and co-flow oxygen mode affected the transient response in a similar way. The cell responded to CO exposure substantially faster than in standard operating mode, i.e. co-flow air mode. In both "non-standard" cases, the steady-state conditions were reached in about eight minutes, compared to about 14 minutes in the standard operating mode.

Figure 39 shows direct comparison of co-flow and counter-flow configuration at 1.5 stoich. Current distribution (left side) and HFR distribution (right side) are shown for 0.8,

0.6 and 0.4 V, representing operation at small, medium and high current densities, respectively. At 0.8 V increased HFRs were recorded at segments Seg06 – Seg10 during counter-flow configuration. The segments were apparently less hydrated. At medium and high current densities (0.6 and 0.4 V) no differences in HFRs occurred due to internal hydration. In contrary, the HFR distribution in counter-flow configuration became slightly more homogeneous along the flow-field.

Reversing the cathode flow inversed the performance distribution of the cell. At medium and high current densities (0.6 and 0.8 V) performance decreased from cathode inlet (Seg01 in co-flow, Seg10 in counter-flow) to cathode outlet (Seg10 in co-flow, Seg01 in counter-flow) in both flow configurations. This indicated that oxygen and water distribution in the cell dominated cell performance. In other words, concentration polarization was the dominant loss mechanism at the given operating conditions. Operating the transient experiment in counter-flow air mode instead of co-flow air mode, enhanced oxygen access to segments at the cathode inlet (Seg10) and obstructed it to segments at the cathode outlet (Seg01).

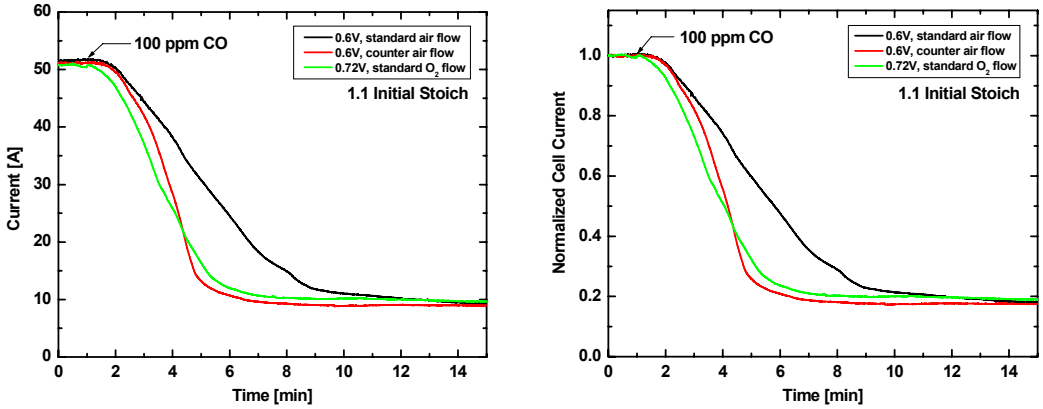

Figure 38: Transient response of the PEFC operated in the standard co-flow air mode, counter-flow air mode and co-flow oxygen mode. The cell operated at an initial stoich of 1.1 prior to exposure to 100 ppm CO. Cell voltage was 0.6 V and 0.72 V during oxygen and air operation, respectively.

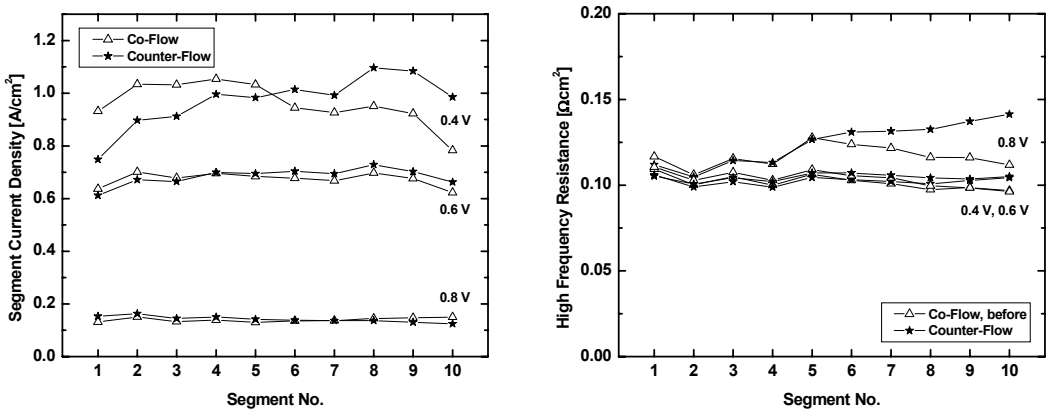

Figure 39: Current density and HFR distribution of segmented cell operated in co- and counter-flow configuration.

Figure 40 shows transient responses of Seg01 and Seg10 as measured (top graphs) and normalized (bottom graphs) in the three cathode operating modes introduced in Figure 38. According to the results shown in Figure 39, the currents of inlet and outlet segments increased and decreased, respectively, by switching from co-flow air mode to counter-flow air mode. The normalized transient response of Seg01 was identical in all three measurements, indicating that the current drop relative to the segment's activity remained unchanged. The normalized current of Seg01 dropped to about 20% of its initial value after five-minute exposure to CO. Unchanging anode operating conditions were consequently dominating the poisoning process of Seg01. Neither oxygen concentration nor water distribution impacted that segment's transient response.

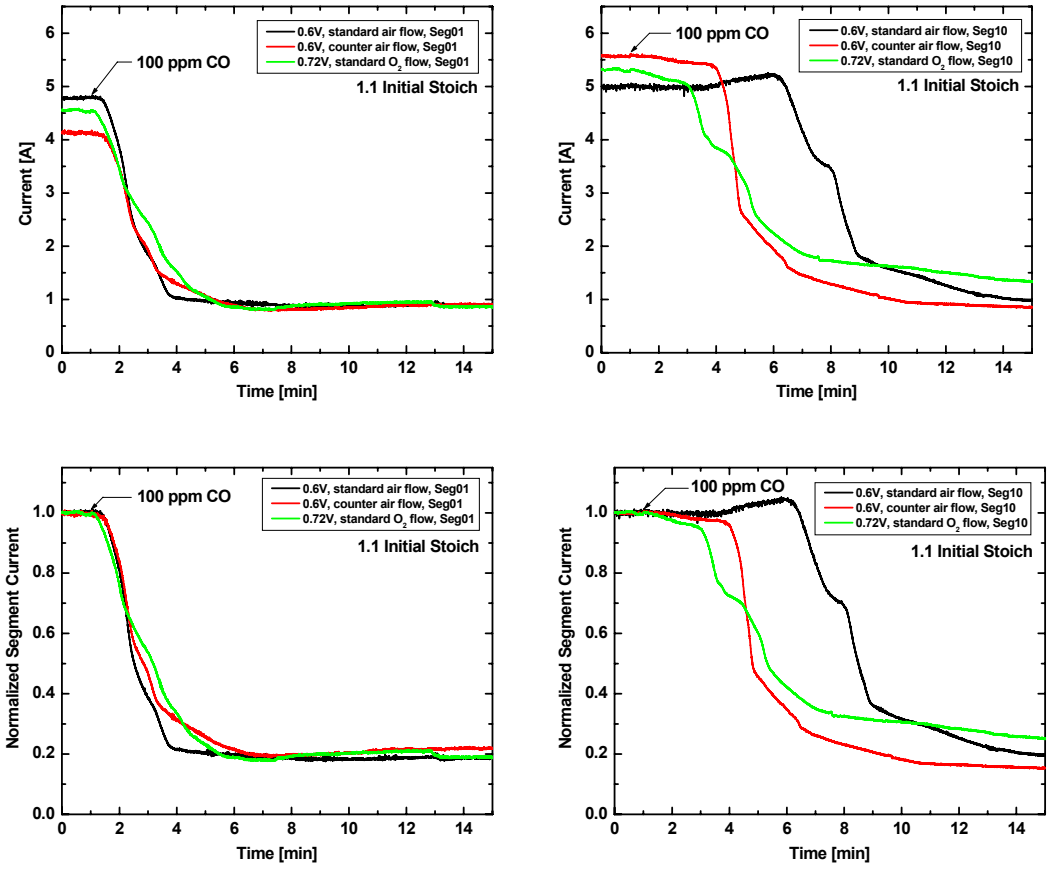

Figure 40: Transient response of Seg01 and Seg10 in the standard co-flow air mode, counter-flow air mode, and co-flow oxygen mode. Poisoning of the anode outlet segment varied as result of altered cathode operating conditions.

In contrast to Seg01, the transient response of segment Seg10 was significantly influenced by "non-standard" cathode operation. The onset of CO adsorption at Seg10 was shifted from about six to about four minutes, indicating accelerated CO adsorption in the preceding anode segments. The current of Seg10 decayed in counter-flow air mode with a one minute delay to, but faster than, the co-flow oxygen mode. A current increase at Seg10 was absent in "non-standard" modes.

The hydration level is identified to influence the CO oxidation process in CO stripping experiments [115]. In this case it was not responsible for the accelerated CO adsorption process. Hydration of Seg10 (and adjacent segments) decreased during the transient measurement in co-flow oxygen mode due to the loss of internal hydration, but at counter-flow air mode cathode hydration at 0.6 V remained constant due to lack of preceding segments (compare Figure 39).

Zhang et al. concluded that the oxygen partial pressure is an important operational parameter that strongly influences the performance of a PEFC involving a Pt anode when

operating with H_2/CO feed [57]. The authors claimed that oxygen diffusing through the membrane contributes to oxidative removal of CO on the anode catalyst surface. Dependence of the anode potential on oxygen partial pressure however, was recorded for operation on pure oxygen only, not for operation on air [57]. Applying Zhang's results to the herein presented transient experiments, the CO adsorption process at the anode should have been delayed when switching cathode gas from air to pure oxygen. It is possible that oxygen crossover to the anode was negligible at the employed operating conditions [117]-[118] and the predicted effect was ineffective. Since Zhang *et al.* did not specify the anode pressure conditions of their experiments, it is also possible that their results were obtained under atypical conditions, such as a high pressure drop across the membrane or insufficiently hydrated membranes. The above presented results did not allow identification of any effect that obstructed CO adsorption on the anode catalyst surface. Instead they suggested, that access of oxygen to cathode reaction sites accelerated CO adsorption rates at the anode.

4.1.3 Steady State Poisoning Conditions

Except for the outlying data points of segment Seg06, **Figure 41** shows normalized current distribution data of all segments obtained in the three measurements introduced in Figure 38. The data corresponded to steady-state poisoning conditions created by exposing the anode to 100 ppm CO for sufficiently long time. The straight lines in the figure represent linear regression fits to the experimental data points, while error bars correspond to the standard deviation of normalized current values.

Switching the cathode air flow from co-flow to counter-flow mode altered current distribution along the flow-field. The segment performance decreased steadily along the flow-field from segment Seg01 to Seg10. Cell hydration at steady-state poisoning conditions resembled cell hydration at small kinetic currents in co- and counter-flow air mode as discussed and shown in Figure 39. Switching the oxidant supply from the co-flow air mode to co-flow oxygen mode showed no impact on the current distribution of the cell at steady-state poisoning conditions. The current distribution remained fairly constant along the flow-field, which confirmed that oxygen crossover was negligible during the performed transient experiments.

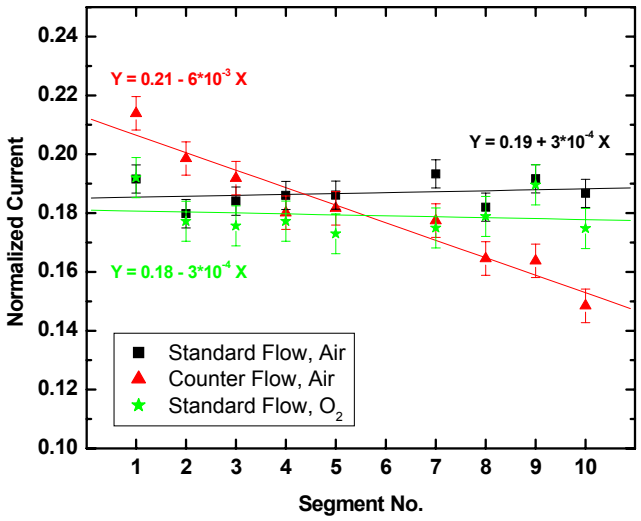

Figure 41: Normalized current distribution under steady-state poisoning of the anode, exposed to 100 ppm CO at various cathode conditions.

4.1.4 CO Recovery

CO adsorption and CO steady state poisoning measurements were accompanied by experiments designed to study anode recovery processes. Recovery was induced by stopping CO injection into the anode feed stream once saturation coverage by chemisorbed CO was reached and continue operating the cell with neat H_2.

Figure 42 shows anode recovery of all ten G-IV segments. The normalized cell currents are displayed for initial stoichs of 1.1 and 1.5. The latter measurement was slightly disturbed by a drop in hydrogen pressure when stopping the CO flow to the cell. At first, cell performance recovery of both measurements was rapid but after approximately two minutes, cell currents started to plateau asymptotically to about 90% of the initial current levels. Performance recovered faster at higher anode flow rates thanks to (i) more efficient purging of bulk CO with hydrogen and (ii) higher supply rate of water to the anode.

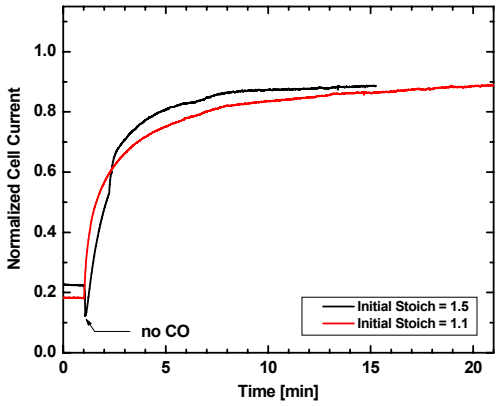

Figure 42: Response of a 77.1 cm^2 cell to a decrease in the CO partial pressure from 100 to 0 ppm at one minute.

Cyclic voltammetry performed at a 50 cm^2 fuel cell indicated that once the current plateau was reached no further performance improvement occurred. **Figure 43** shows cyclic voltammograms recorded with a scan rate of 5 mV/s after one hour (left graph) and 93 hours (right graph) of recovery in H_2/Air configuration. Performance of the cells recovered to 94% and 95% of the initial performance. In both experiments, the measured charge representative for hydrogen oxidation implied lower recovery states.

Two distinct peaks at 0.48 V and 0.52 V were recorded after one-hour anode recovery. At identical experimental conditions, peak potentials down to 0.52 V were observed for oxidative CO removal, performed immediately after exposure to CO in N_2 atmosphere. The second peak potential was lower than typically observed and may not be associated with surface CO. The size of the peaks decreased with longer recovery, i.e. after 93 hours of anode operation without exposure to CO. Irrespective of the recovery time, additional charge was recorded at potentials above 0.6 V. While the amount of that charge appeared to increase with the recovery time, its origin remains unknown. The charge substantially diminished with cycling and did not seem to significantly impact anode activity for hydrogen oxidation. The total CV charge of the peaks and the potential range that corresponds to the oxide formation was 3.3 C/cm^2 and 2.1 C/cm^2, after the anode recovery time of one hour and 93 hours, respectively. These charge values if caused by surface CO only would correspond to 65% and 40% CO coverage, respectively.

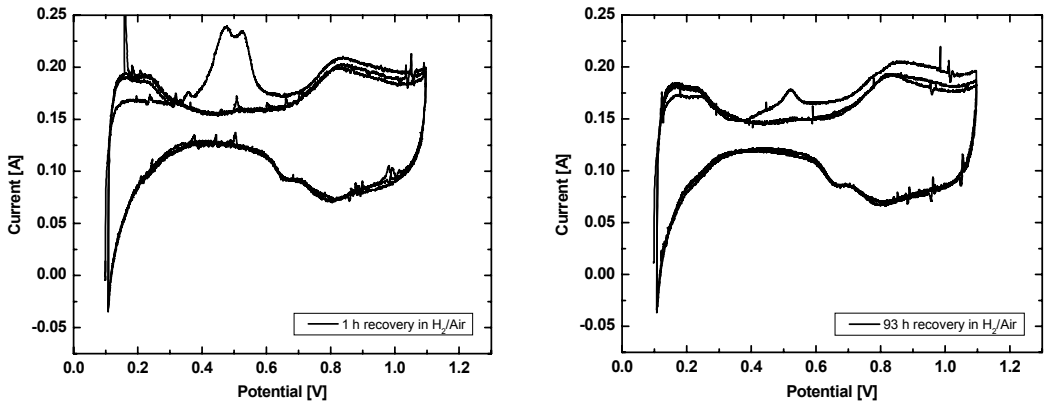

Figure 43: CV measurements of 50 cm^2 fuel cell, after 1 and 93 hours of anode recovery on pure hydrogen.

The normalized current distributions of the presented cell recovery measurements are shown in **Figure 44**. The rate of the recovery process depended on the segment location along the flow-field and, as expected, was faster for the inlet segments than the outlet segments. After 40 minutes of recovery on pure hydrogen feed at the initial stoich of 1.1, the current varied between 95% of its initial value for segment Seg01 and 84% for Seg10. Apparently, simultaneous recovery at upstream segments slowed and limited recovery of downstream segments. It is to expect that downstream segments show increased presence of unknown surface species as discussed, resulting from recovery processes upstream.

Similar recovery pattern was recorded at initial stoich of 1.5, but in a shorter time period of 14 minutes.

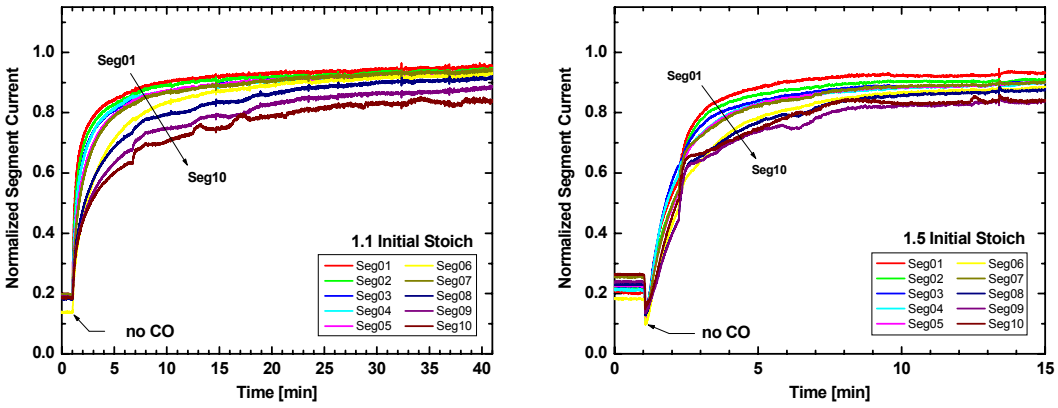

Figure 44: Current response of the segmented cell to a decrease in the CO partial pressure from 100 to 0 ppm at initial stoichs of 1.1 and 1.5.

The progress of the recovery process within the cell is shown in **Figure 45**. The normalized current of the individual segments at the initial stoich of 1.1 is plotted versus the segment number before and during recovery at selected intermediate times. After

five-second recovery on pure hydrogen all segments showed performance improvement. Linear regression fits revealed that the biggest differences in the performance of individual segments occurred after one-minute recovery. On average, performance dropped by 3% per segment on the way from the inlet to the outlet of the cell. The differences tended to lessen at longer recovery times, but did not disappear. After 30 minutes, performance decreased by only 1% per segment.

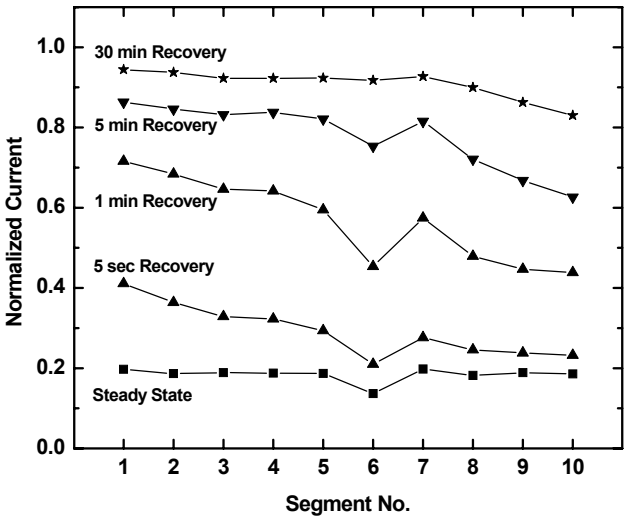

Figure 45: Distribution of normalized segment currents before and during the recovery on pure hydrogen (initial stoich 1.1).

Contrary to the CO adsorption step, cell recovery appeared independent of the cathode flow mode and cathode gas used (air or oxygen). **Figure 46** shows the recovery of the CO-saturated cell in the standard co-flow air mode, counter-flow air mode, and co-flow oxygen mode as measured and normalized for 1.1 initial stoich. The time required for cell recovery was identical in all three modes, with approximately 89% of the initial cell current recovered after 20 minutes of operation on pure hydrogen.

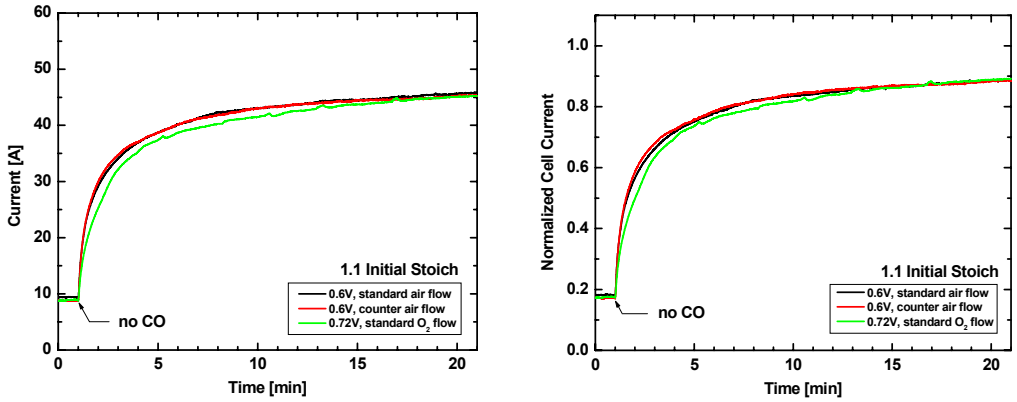

Figure 46: Cell response to a decrease in the CO partial pressure from 100 to 0 ppm CO (intial stoich 1.1).

Although neither the partial pressure of oxygen nor cathode flow mode affected the anode recovery process of the entire cell, significant differences were recorded for individual segments. **Figure 47** shows normalized recovery currents of the inlet segment Seg01 on the left and the outlet segment Seg10 on the right. During the first five minutes of recovery, the current at Seg01 increased significantly faster than at Seg10. The highest and most rapid recovery occurred in counter-flow air mode. After 20 minutes recovery, the current of Seg01 reached 97% of its initial value. In the same time period, recovery in co-flow air and oxygen mode led to 93% and 90% of the initial current value, respectively. Seg10 recovered slower than Seg01 at all cathode operating modes. Fastest and with 88% most complete recovery of Seg10 was recorded in co-flow oxygen mode. Co-flow and counter-flow air mode followed, recovering to 79% and 70%, respectively.

The anode recovery process is induced by the presence of pure hydrogen, and additionally favored by the presence of oxygen and water. Hydrogen access to surface CO was strongest at the anode inlet, where hydrogen partial pressure was highest. With the onset of recovery, increasing hydrogen utilization caused shifts in water management. Hydrogen partial pressure decreased along the flow-field and decelerated recovery at downstream segments. During counter-flow air mode higher water levels were present at Seg01 than at Seg10, as indicated by the current distribution at 0.6 V presented in Figure 39. Opposite trends occurred at co-flow air mode. Compared to co-flow air mode, recovery at counter-flow air mode was faster for Seg01, but slower for Seg10, indicating possible correlation of water level and recovery rate. Operation with oxygen equalized recovery of all segments. Segment recovery was slower at the cell inlet, but equally fast and complete at the cell outlet. The data allowed to safely conclude that a combination of hydrogen access to CO-covered anode catalyst sites and oxygen and water access to the corresponding regions of the cathode were responsible for the cell recovery rate. Trends

at different operating conditions equalized along the entire flow-field and resulted in identical recovery of the cell.

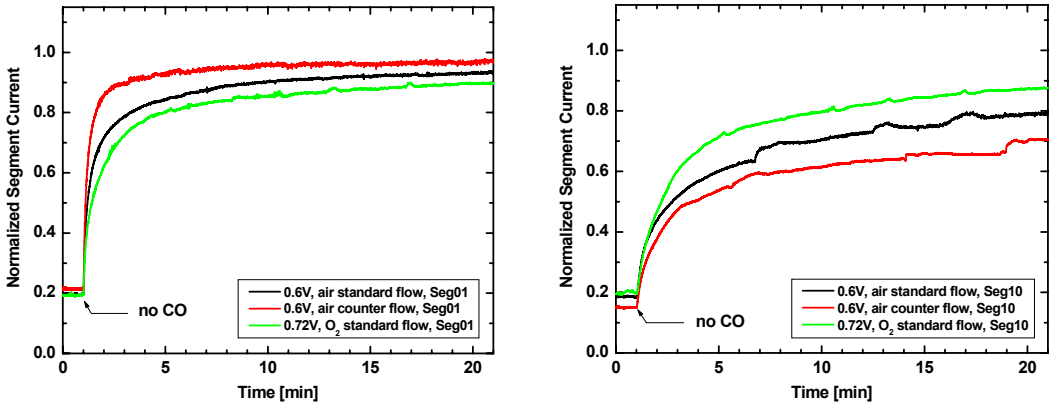

Figure 47: Normalized response of Seg01 (left) and Seg10 (right) to a decrease in CO partial pressure from 100-0 ppm CO at 1.1 initial stoich and various operation conditions.

4.1.5 Model Evaluation

The experimental data presented in previous sections of this chapter did not allow for definite identification of all processes occurring in the cell. In order to shed more light on the mechanism of CO poisoning and anode recovery, a time-dependent model for the segmented cell was developed by and in close collaboration with T.E. Springer from LANL. The model was based on previous Los Alamos models [111] and the experimental data acquired in the course of this work. In spite of several iterations to date, the model still needs further development to account for all the phenomena that take place in the fuel cell. However, the herein presented iteration was capable of predicting spatial response to CO injection into the hydrogen stream. A preliminary report describing the current state of the model and findings to date can be found in the Appendix.

Modeling of the anode poisoning with 100 ppm CO in hydrogen delivered at the initial stoich of 1.1 and subsequent anode recovery on pure hydrogen at 0.6 V is shown in **Figure 48**. The current values have been normalized to the initial current density of 0.67 A/cm^2, recorded prior to CO exposure. The model prediction of the cell response to CO differed from the experimental data shown in Figure 36. Overall, the model predicted faster and more significant current drop throughout the poisoning process. As expected, based on the assumption of constant cathode operating conditions during the measurement, the model did not predict the observed increase in the current density at the onset of CO poisoning at the cell outlet. At the same time, the model suggested a gradual decrease in the current density for the downstream segments at steady-state poisoning conditions. This performance pattern was caused by an increase in the mole fraction of

CO along the flow channel due to gradual hydrogen utilization. This prediction of the model was, however, not observed in the experiments (compare Figure 36).

The model agreed well with the experimental data recorded during anode recovery from CO exposure shown in Figure 44. Both the model and the experiment showed faster recovery at the inlet segments and slower recovery at the outlet segments. The predicted recovery time matched the experimentally measured recovery time. Contrary to the experiment that attested to an incomplete anode recovery, the model claimed full restoration of the active platinum sites over time. It allowed all segments to recover in 40 minutes to at least 97% of their initial performance.

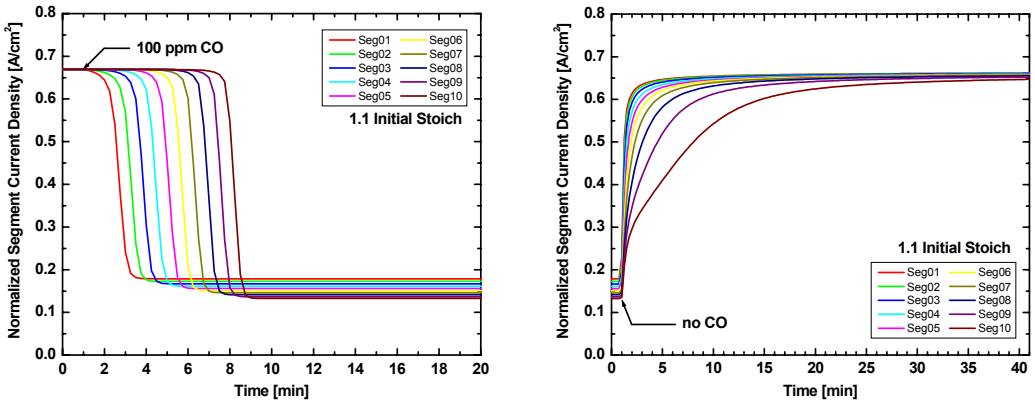

Figure 48: Modeling of the cell response to 100 ppm CO and subsequent recovery at 0.6 V. Current densities normalized to total cell current measured prior to CO exposure.

Molar fractions of CO and CO_2 in the anode feed stream under the steady-state CO poisoning conditions are listed in **Table 7**. Gas samples were collected and analyzed by gas chromatography (GC) at the outlets of (i) the gas tank (0.01% CO in hydrogen balance), (ii) the humidifier bottle (equivalent to the fuel cell inlet), and (iii) the fuel cell.

The GC measurements revealed that the mole fraction of CO decreased upon gas passage through the humidifier bottle. At the same time, the molar fraction of CO_2 increased by about the same amount, indicating that some CO was converted to CO_2 in the humidifier bottle. This was likely to involve air introduced with the water during the bottle refill. The theoretical gas composition at the fuel cell outlet was calculated from the inlet gas entering the cell and hydrogen utilization in the cell. While the predicted and measured gas composition data differed somewhat (Table 7), the sum of the CO and CO_2 molar fractions given in Table 7 remained constant. One possible reason for the discrepancy between the model and experiment was an additional conversion of CO to CO_2 inside the fuel cell, with water and/or dissolved oxygen acting as CO oxidizer.

Table 7: Predicted and measured composition of the anode gas stream under the steady-state CO poisoning conditions.

	Gas Tank	Fuel Cell Inlet	Outlet Prediction From Inlet Data	Fuel Cell Outlet
CO	118 ppm	106 ppm	147 ppm	120.5 ppm
CO2	0.5 ppm	9.5 ppm	15 ppm	43 ppm
CO + CO2	118.5 ppm	115.5 ppm	162 ppm	163.5 ppm

Introduction of CO conversion to CO_2 along the anode flow-field was one next step in the model development effort. **Figure 49** shows the modeled current response considering a constant amount (equivalent to $2 \cdot 10^{-5}$ A/cm^2) of CO converting to CO_2 in the anode feed stream. The effect of exposure to 100 ppm CO is shown in the left graph. The implementation of chemical conversion of CO into the model rendered the predicted cell response, including the poisoning times, closer to that obtained in the experiment. Also, the improved model predicted a nearly uniform distribution of current densities for individual segments, which was in agreement with the experimental data presented in Figure 36.

The altered model was also used to predict the segment current distribution in response to the removal of CO from the anode feed stream (Figure 49 right graph). It generated almost identical recovery plots for all segments of the cell, a result that was not confirmed by the performed experiments (Figure 44). This prediction incorrectly considered CO conversion to CO_2 in the cell without any CO present in the anode feed stream and thus demonstrated the model's sensitivity to input conditions.

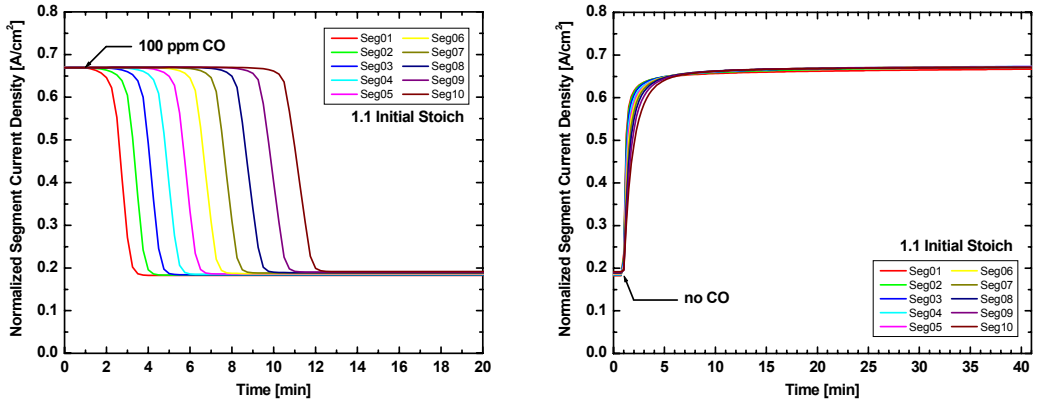

Figure 49: Predicted cell response to 100 ppm CO and subsequent recovery at 0.6 V using modified model (see text for details). Current densities normalized to total cell current measured prior to CO exposure.

4.2 Performance Distribution of DMFC

The design of practical DMFC systems involves a trade off between higher power density (low individual cell voltage, high power density) and higher efficiency systems (high individual cell voltage, low power density). Higher power density systems require fewer cells or less active surface area and therefore are smaller, lighter and cheaper on a capital basis. However, these gains come at the price of reduced efficiency requiring more fuel for equal power production resulting in higher fuel costs and either larger fuel reservoirs or shorter operation times. The operating potential of a DMFC will be specified by its application. For the data reported here, the focus lies on two operating potentials: 0.4 and 0.6 V. The latter represents a region where the DMFC is kinetically limited, the first represents a high power density region. Both operating potentials have relevance to operating conditions in practical systems.

4.2.1 Polarization Measurements

The left side of **Figure 50** shows polarization curves of the individually operated G-IV DMFC segments in hydrogen mode. Between measurements segments were operated 10 minutes at 0.7 V for equilibration. The performances deviated from segment to segment, but no regular pattern with downstream position or platinum loading could be identified, despite careful examination of current density data in the region of higher current densities at 0.6 V. Mass transport limitations in the segmented cell were high, even for hydrogen operation. The segment polarization curves already showed significant influence of concentration polarization at current densities between 700 – 800 mA/cm^2. The high compression of the fuel cell hardware that was needed for sealing impacted the backing porosity and obstructed mass transport of the gas diffusion layers of anode and cathode. This affected in particular the cathode performance of the cell negatively.

The HFR values of the individual measurements are presented on the right side of Figure 50. At current densities smaller than 400 mA/cm^2 resistance values were determined between 0.125 - 0.135 Ωcm^2. These were very low resistance values considering the thickness of the N117 membrane (178 μm). The high compression applied to the hardware probably created very good interfacial contacts between flow-fields, backings and electrodes. At current densities higher than 400 mA/cm^2, the HFR increased as a function of current density. This trend is stronger the closer the segment was located near the gas inlet. The increase of the HFR of the Pt-black catalyst is much stronger than the increase of the HFR observed with Carbon supported catalyst (Figure 13). The wetting properties of carbon may have contributed to keep the catalyst layers at the anode humidified and the cell resistance low.

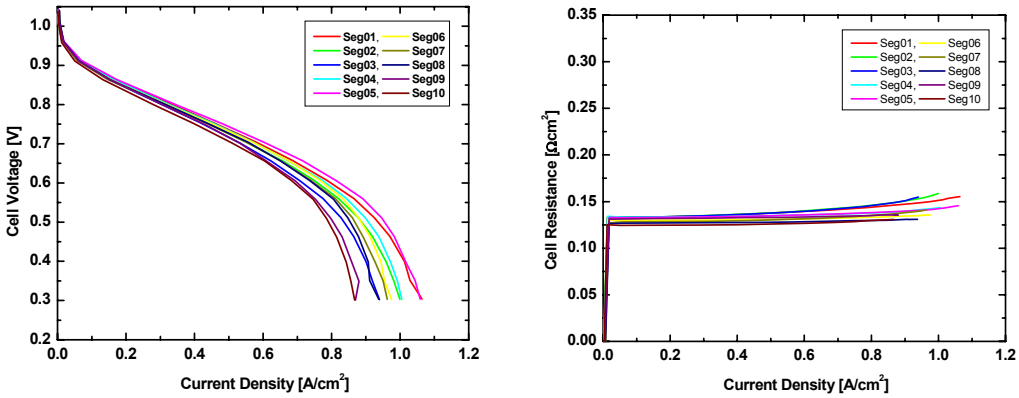

Figure 50: Polarization curves and HFRs of segmented DMFC operated individually at identical operation conditions with hydrogen. While one segment is operating, the other segments are disconnected.

The individually measured performance characteristics and HFRs of the 10 segments during operation with methanol are shown in **Figure 51**. Anode operating conditions and cell temperature were set to standard values. The cathode operated at the same air flow rate used for hydrogen operation, but at ambient pressure and without humidification.

Operating the cell with methanol instead of hydrogen clearly generates lower power due to increased overpotentials and methanol crossover. Currents started flowing at cell voltages of around 0.7 V and lower. The kinetic region of the segments, i.e. the region dominated by activation polarization, ended at about 0.6 V, the ohmic region spanned over cell voltages between 0.6 V - 0.5 V. At even lower potentials the cell began to be strongly limited by concentration polarization. Mass transport limitation of the segments was unusually high. Operation of DMFC cells at similar conditions, or even at humidified conditions, do not typically show mass transport limitations; as comparison with arbitrary DMFC data from the literature showed [119].

Performance also showed great variation of individual segment performance during methanol operation. One obvious reason for strong variation of the cathode performance was operation without cathode humidification. The HFRs are shown on the right side of Figure 51. They vary between 0.30 Ωcm^2 measured at segment Seg02 and 0.14 Ωcm^2 measured at segment Seg10, indicating decreasing HFRs with increasing presence of water from cell inlet to cell outlet. The water at the non-humidified cathode originated from (i) water crossing over from the anode due to water drag and diffusion, and (ii) internal hydration due to production of reaction water. The latter was rather small at the observed current densities. Methanol solution was fed into the anode. Hence liquid water was present at all anode segments and the amount of crossing water per membrane was constant at open circuit conditions. The presence of water consequently increased from cathode inlet to cathode outlet. The first segment could only profit from water crossover through its own area. All the other segments benefited from water crossing through

upstream segments also, diminishing the cell resistance as presented in Figure 51. Please note that segment Seg01 showed lower HFR than Seg02, inverting the trend of increasing HFR from outlet to inlet. This may have been caused by flow effects at the flow-field inlet of the cathode. This trend was not observed at lower cathode flow rates.

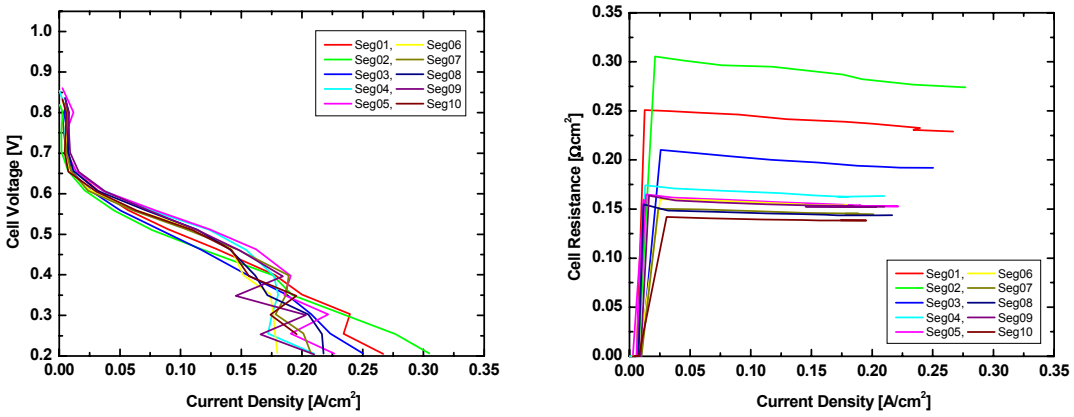

Figure 51: Polarization curves and HFRs of DMFC segments operated individually at identical operation conditions with 0.48 M methanol. While one segment is operating, the other segments are disconnected.

The changing local operating conditions along the flow-field resulted in varying segment performances. The left side of **Figure 52** shows segment current densities as a function of segment position plotted for different cell voltages. Fitting data for each cell voltage revealed that at cell voltages of 0.6 V and higher no trends of current density as a function of segment position existed. Instead the current density showed qualitative agreement with anode loading as illustrated in the right part of Figure 52. This suggested that at low current densities the individual segment performance was dominated by activation polarization. At a lower cell voltage of 0.5 V, the segment performance increased along the flow-field (Figure 52, left). The segment performances, now dominated by ohmic polarization were strongly dependent on the ionic conductivity of membrane and cathode catalyst layer. Stronger humidified segments at the cell outlet (Figure 51, right) consequently performed better. This trend was slowly reversed at a cell voltage of 0.4 V and lower. At these cell voltages the segments loss mechanism was dominated by concentration polarization due to the increased production of reaction water which, together with the water crossover, caused flooding of the cathode catalyst layer. As a result, at a cell voltage of 0.2 V, segment performance decreased strongly along the flow-field.

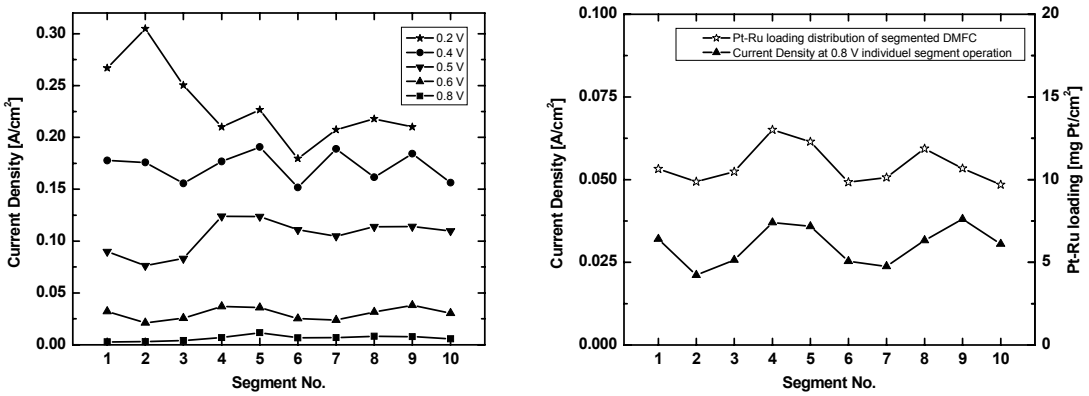

Figure 52: Performance of individually operated DMFC segments with respect to flow-field position.

4.2.2 Segmented DMFC Operation

Additional water production was expected with simultaneous operation of all 10 segments. **Figure 53** shows the performance characteristics for this case. The left part of Figure 53 shows the current distribution of the cell. Seg01 is plotted at the rear, the subsequent segments in sequential order moving forward to Seg10. The polarization curves were very similar to the individually measured data set. The kinetic performance during regular operation increased with segment location along the flow-field. Water at the cathode was now additionally originating from reaction water produced at all upstream segments. Although current densities were rather small, concentration polarization seemed slightly elevated and kinetic performance increased along the flow-field. The HFRs of the same measurement are plotted in the right part of Figure 53. They showed very similar behavior to the individually measured HFR. This indicated, that segment hydration along the flow-field was dominated by water diffusing from anode to cathode and not by internal hydration of preceding segments.

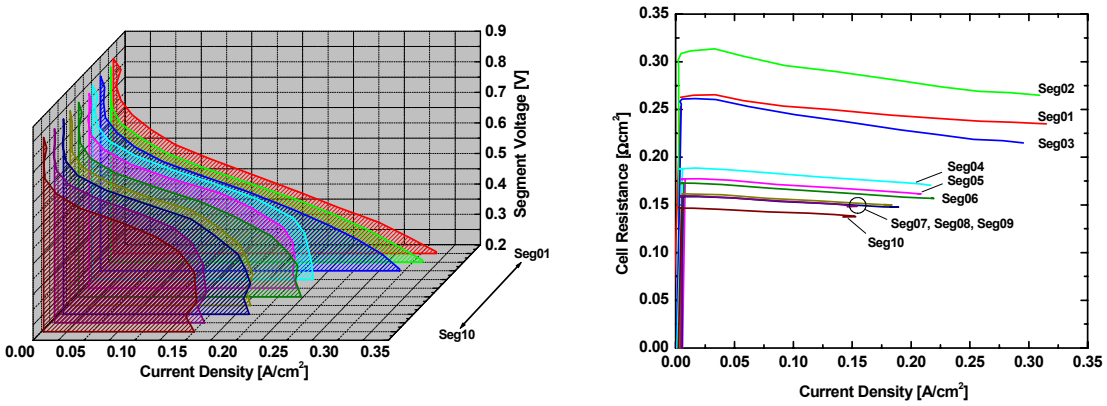

Figure 53: Left: Waterfall graph of the segmented DMFC showing the current distribution along the flow-field. Right: HFRs of the segmented cell recorded during measurement of the polarization curves.

Figure 54 shows polarization curves of the individually and joint operated segments Seg01, Seg04, Seg07, and Seg10. The current density in the kinetic region increased along the flow-field, which may have resulted from upstream water production. Small amounts of water could already be beneficial for a cathode that is operated without humidification. However, the strong variations in the region dominated by mass transport gave cause for concern. Higher limitations for the individually operated Seg01 and Seg04 were not expected.

While performing the reference measurements, segments upstream the measured segment were disconnected. During hydrogen operation, this led to minimum fuel utilization upstream and created constant operating conditions for the individually measured segments. But during methanol operation, the operating conditions for each individually measured segment changed. Water crossover and maximum methanol crossover occurred upstream the measured segment, changing its operating conditions as a function of its position along the flow-field. Constant operating conditions could not be achieved for each individual segment. Contrary to hydrogen operation, when switching to joint operation during methanol operation not only gas utilization and water distribution changed along the flow-field, but also methanol crossover rates due to fuel utilization. Employing the individually measured segment performances as references was not possible, since spatial processes like methanol and water crossover could not be isolated for the reference measurement. Instead, standard polarization, methanol crossover and anode polarization measurements were employed to analyze impact of DMFC operating conditions on spatial performance.

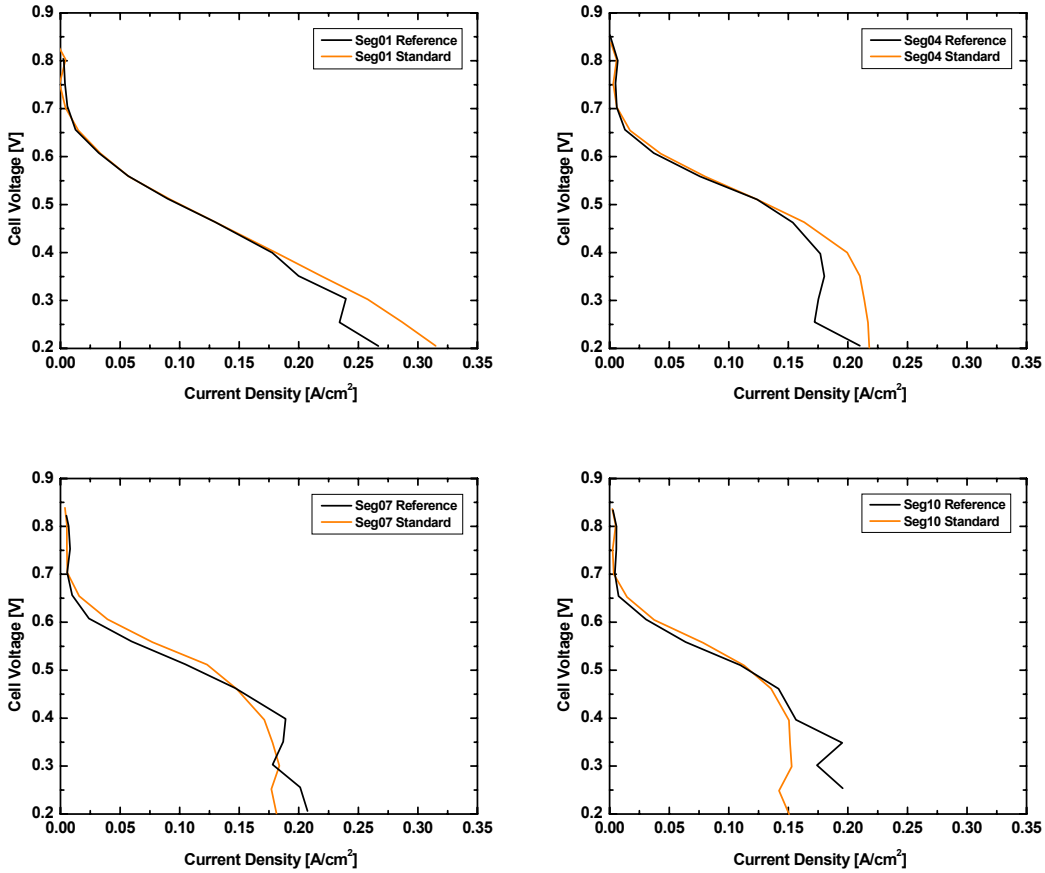

Figure 54: Comparison of reference measurements (only one segment operating) with standard operation measurements (all segments operating) for DMFC Seg01, Seg04, Seg07, and Seg10.

4.2.3 Effect of Methanol concentration

MeOH concentration is one of the most easily varied operating parameters and can have a significant impact on cell performance. **Figure 55** shows polarization and HFR measurements of the total cell operated with 0.29, 0.48, and 1.0 M methanol solutions. In the kinetic region, e.g. 0.6 V, performance decreased with increasing concentration of methanol, whereas in the region dominated by concentration polarization, e.g. 0.4 V, performance increased with concentration. This trend was expected and can be explained by two processes: (i) methanol crossover and (ii) concentration polarization. The amount of crossover methanol at the cathode increases with methanol concentration fed to the anode according to Fick's first law of diffusion (8). This lowered cathode potential and reduced cell performance. This effect is diminished with increasing current density since fuel utilization reduces the starting concentration for methanol crossover. At high current densities, concentration polarization dominates performance. The amount of methanol available at the anode is a function of methanol concentration. Lower concentrations are

limited to lower current densities due to fuel utilization. The data in Figure 55 show very high mass transport limitations at low methanol concentration resulting in a limiting cell current density of only 100 mA/cm^2. At 1 M methanol however, mass transport limitations are not dominant even at 400 mA/cm^2.

The HFR values of the cell range from 160 -170 mΩcm^2. The highest resistance value is observed for the 1 M methanol solution, suggesting a small change in conduction properties of the solid electrolyte due to methanol concentration.

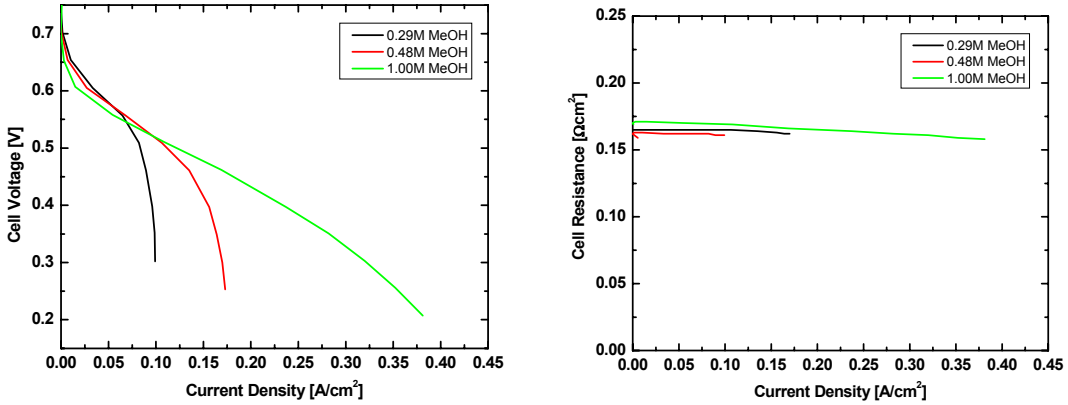

Figure 55: Total cell performance and HFR at various methanol concentrations.

The current density and HFR distribution of the cell was recorded at three methanol concentrations as shown in **Figure 56**. The data was presented at 0.6 V and 0.4 V, two operating points of potential importance for DMFCs as discussed previously. One of the most striking features of Figure 56 was the dependence of the HFR on segment number. Resistance values decreased similarly along the flow-field at all recorded MeOH concentrations and cell voltages. The HFR at the inlet segment Seg01 was about 45% larger than that of the outlet segment Seg10. While a small change of resistance due to methanol concentration was observed, this was minor compared to the spatial dependence of the resistance. In the kinetic region (0.6 V), cell performance was lower at high methanol concentration. Performance was constant along the flow-field, indicating no significant contribution of concentration polarization and confirming the conclusions drawn previously. At lower cell voltage (0.4 V) and higher current density, performance dropped linearly from cell inlet to cell outlet for 0.29 M and 0.48 M methanol solutions. This suggested concentration polarization was more important than trends associated with downstream decrease of HFR, shown on the right side of Figure 56. The fuel was utilized along the flow-field, which increased concentration polarization and thus affected segment performance throughout the cell. This situation changed at 1.0 M methanol concentration, where performance first increased up to segment Seg05, before it dropped along the flow-field. In this case, the trade off between activation polarization losses due to dry cathode operation and concentration polarization had been shifted due to the

increased amount of MeOH available for reaction. Obviously, cell resistance, as shown on the right of Figure 56, was slightly increased for 1.0 M methanol solution at 0.4 V, while it contributed disproportionately stronger to the overall loss at the cell inlet. As segments hydrated along the flow-field, concentration polarization regained its dominance and performance started dropping from Seg05 – Seg10.

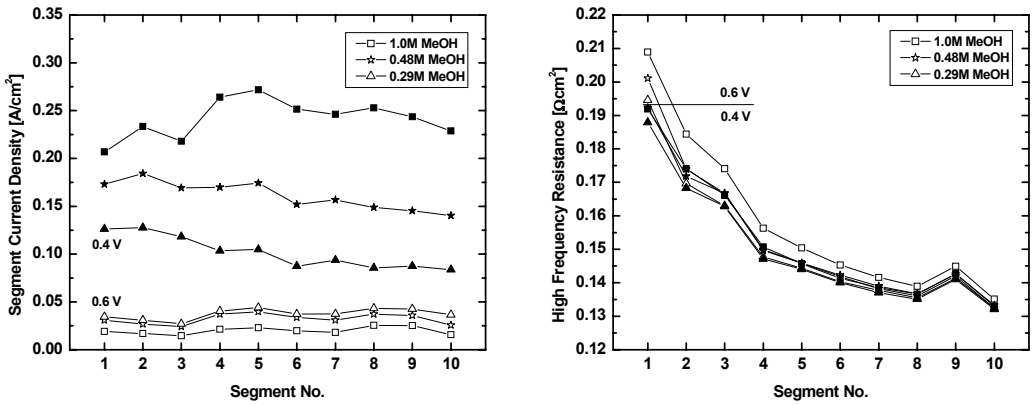

Figure 56: Current and HFR distribution at 0.6 and 0.4 V for various methanol concentrations.

To isolate and identify the contribution of the anode to performance differences at various methanol concentrations (0.29, 0.48, and 1.0 M), anode polarization measurements were performed. **Figure 57** shows the results of this experiment, which is performed in driven mode, for the entire cell on the left, and the corresponding distribution of the computed limiting currents on the right. Limiting currents at 0.48 M MeOH are shown for individual (white) and joint (black) operation.

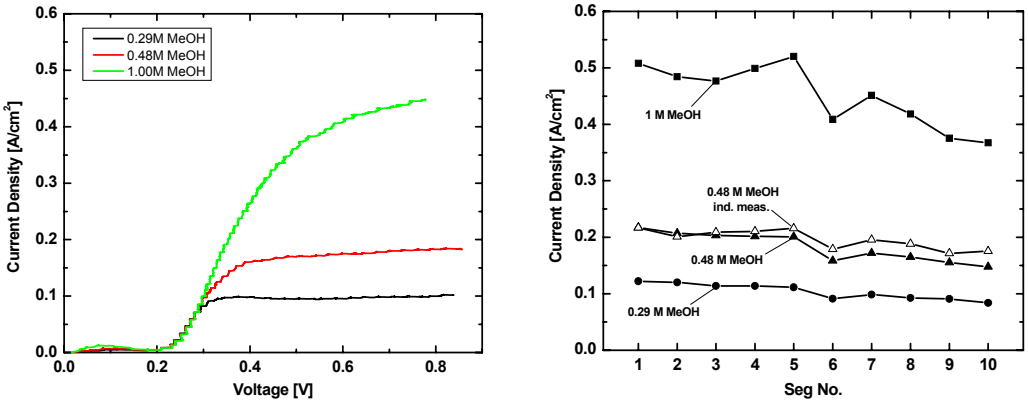

Figure 57: Total cell anode polarization measurements and spatial anode polarization limiting currents of various methanol concentrations.

As expected, the limiting currents of the cell increased with increasing methanol concentration. Up to a potential of 0.3 V, the anode performance was identical at all

concentrations, but it deviated at higher potentials, due to different onset of concentration polarization of the three methanol solutions. Limiting currents amount to about 0.45 A/cm^2 at 1.0 M methanol solution, 0.18 A/cm^2 at 0.48 M, and 0.1 A/cm^2 at 0.29 M, respectively, indicating a nonlinear response. The results corresponded well with the maximum currents of the polarization curves presented previously in Figure 55.

The limiting current densities of the total cell as shown in the left part of Figure 57 corresponded to the average limiting currents of the distribution shown in the right part of the graph. Anode performance decreased for all concentrations from inlet to outlet, an effect caused by methanol utilization, methanol crossover and/or CO_2 blinding adding up along the flow-field. **Table 8** lists the average decrease per segment of the anode polarization limiting currents expressed as both, an absolute value and a percent change (with respect to the performance measured at the inlet segment Seg01). Anode limiting currents at joint operation dropped between 31 – 37% from inlet to outlet, for all the concentrations tested here.

Table 8: Gradients of limiting currents determined during anode polarization and methanol crossover experiments for various methanol concentrations.

Methanol Concentration [M]	Gradients of Anode Polarization Limiting Currents along Flow-Field i / Seg		Gradients of MeOH Crossover Limiting Currents along Flow-Field i / Seg	
	[(A/cm^2)/Seg]	[%Seg01]	[(A/cm^2)/Seg]	[%Seg01]
5.0	-	-	-0.003	-0.9
2.0	-	-	-0.00186	-1.0
1.0	-0.01561	-3.1	-0.00113	-1.2
0.48	-0.00794	-3.7	-0.00096	-2.1
0.48 (ind. Seg measurements)	-0.00463	-2.1	-	-
0.29	-0.00438	-3.6	-0.00058	-2.1

The limiting currents of the individually performed anode polarization measurements dropped 21% from inlet to outlet. During these experiments, disconnected segments switched from maximum fuel utilization at joint operation to no fuel utilization, and from the minimum possible MeOH crossover to the maximum. Clearly, the increase in anode

performance during individual operation indicated that the loss of MeOH due to fuel utilization and minimum crossover exceeded the loss of MeOH due to maximum crossover. The results demonstrated the importance of methanol crossover as a power loss mechanism, especially at low currents.

The left side of **Figure 58** shows methanol crossover measurements of the total cell performed with 0.29 - 5.0 M methanol solutions. The recorded limiting crossover currents range from 25 - 335 mA/cm^2, their value increasing roughly proportional to methanol concentration. At high concentrations, the largest deviations from linearity were found, as would be expected due to the effects of electro-osmosis opposing methanol flux. These results could be rationalized using a model that accounted for the flux of water against MeOH diffusion like that proposed by Ren et. al. [109].

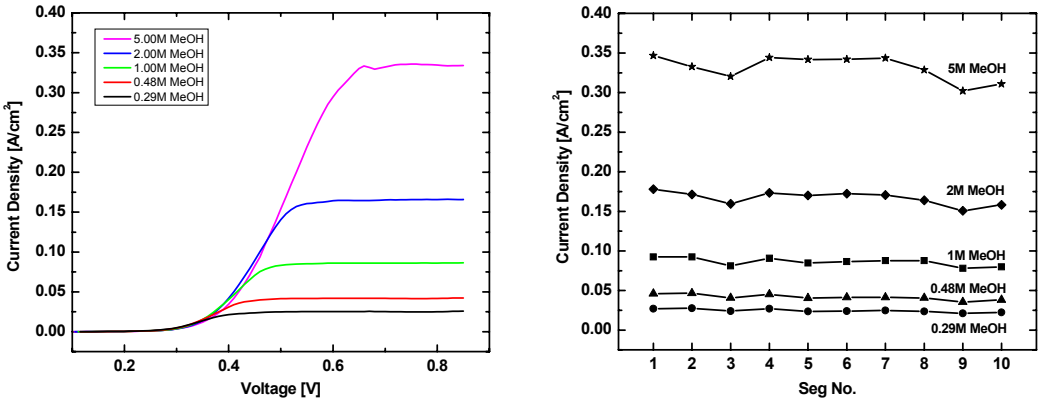

Figure 58: Total cell and spatial methanol crossover measurements performed at various methanol concentrations.

The distribution of the limiting current densities (at 0.8 V) at the five investigated concentrations is shown on the right side of **Figure 58**. Limiting currents decreased along the flow-field, as methanol was depleted by methanol crossover and/or gas blinding occurred from proton recombination to hydrogen. The results of methanol crossover experiments were quantified and compared to similar results for anode polarization in Table 8. While the absolute loss of MeOH increased with concentration, the relative change along the flow-field decreased. The determined relative change along the flow-field associated with MeOH crossover was higher for anode polarization experiments than for MeOH crossover experiments. This might have been attributed to different MeOH consumption or gas evolution rates during the experiments.

Figure 59 shows methanol crossover data of the entire cell at 0.8 V as measured (black) and after correcting for the effect of electro-osmosis (white). The correction was performed using the standard method at LANL as introduced by X. Ren *et.al.* [109]. The proton current opposing the methanol flux acts as a self-limiting effect on the recorded methanol crossover current. This effect becomes stronger with increasing methanol

concentration, since the proton current opposing methanol transport increases. The relative trend along the flow-field for each methanol concentration does not change. The corrected methanol crossover gradients along the flow-field were found to be identical to the data presented in Table 8. No additional information was gained by correcting the response of all segments for all methanol concentrations, but as the data in Figure 59 shows, substantial deviations result at high methanol concentrations between corrected and uncorrected values. If accurate methanol crossover values are sought for research purpose, correction is necessary. Otherwise, as in this work, general trends can be expressed by the recorded values.

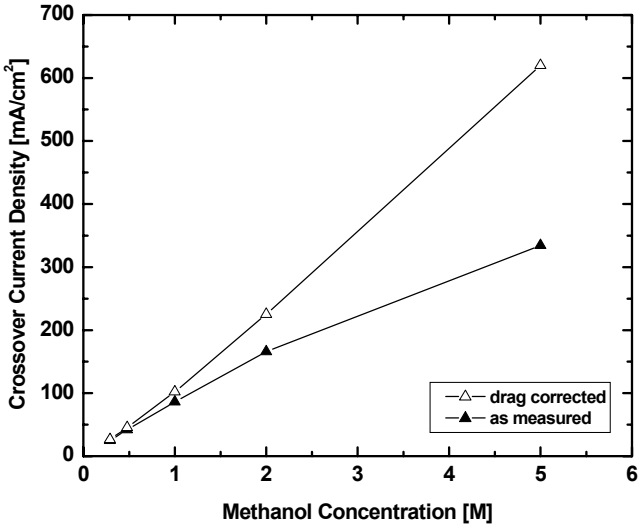

Figure 59: Total cell methanol crossover measurements at 0.8 V as measured and corrected for electro-osmotic drag.

It is important to recall that anode polarization and methanol crossover measurements are diagnostic techniques that isolate factors that directly contribute to cell performance. Care must be taken when trying to relate these results to DMFC performance. The one clear effect that could be seen from the data reported here was that downstream MeOH depletion occurred in the cell and that it decreased local performance from anode inlet to anode outlet.

4.2.4 Effect of cathode humidification

Cathode humidification is another operating condition that affects system performance. Incomplete humidification can lead to ohmic and kinetic losses at the cathode. Adding humidification to a DMFC system increases system complexity, volume, weight, cost, and energy losses due to power consumed by the humidification system. Thus it is vital to understand the trade offs between performance gains and losses associated with humidification.

Figure 60 shows total cell polarization curves and HFR measurements, dry and humidified, at standard DMFC operating conditions. Omitting humidification of the cathode feed increased the HFR by about 25 mΩcm^2 throughout the current range. Consequently cell performance decreased during dry operation. At a current density of 100 mA/cm^2 for example, cell voltage dropped 30 mV. Since the measurements were performed in controlled voltage mode, comparison of individual data is more convenient at constant voltages. At a constant potential of 0.5 V however the current density changes are 28.5 mA/cm^2 and appear rather large. It has to be kept in mind during the discussion of the following data sets, that a relatively large loss of current may correspond to only a small change in voltage. Performance in current controlled operating mode would have been useful for data interpretation and is strongly recommended for future investigations.

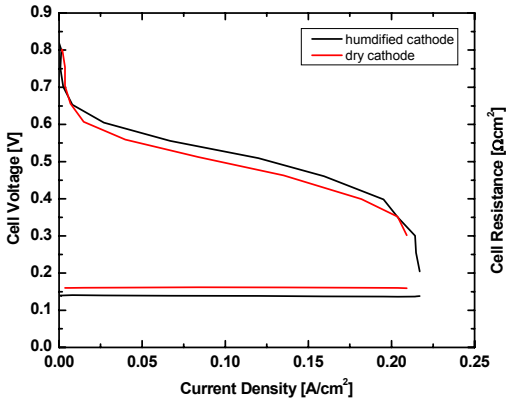

Figure 60: Total cell performance and HFR at humidified and dry cathode operation.

The effect of dry versus humidified operation on performance and HFR distribution is shown in **Figure 61**. While performance as a function of spatial dependence showed good qualitative agreement between dry and humidified operation, dry operation was detrimental for cell performance at all cell voltages. The performance of the fourth segment switching from humidified to unhumidified conditions was fairly representative of the observed trends. It exhibited 54% less current at 0.6 V, 32% at 0.5 V, and 6% at 0.4 V respectively.

The performance results complied with the performed HFR measurements. During dry operation HFR values decreased significantly from Seg01 – Seg10 (50 mΩcm^2), and only slightly (10 mΩcm^2) when humidified. The latter was most probably due to slightly incomplete external gas humidification. HFR was independent of current density during dry and humidified operation, as might be expected for constant stoich operation. The strong decrease in HFR along the flow-field during dry operation suggested that hydration increased along the flow-field due to water diffusing across the membrane and internal hydration. Measurements at decreased cathode stoich, such as presented in the

next section, did not show a further decrease in HFR at the cell outlet. This indicated that maximum hydration was reached at the outlet segments for dry operation. When humidifying the cathode, increased presence of liquid water at the cathode might have further facilitated cell hydration.

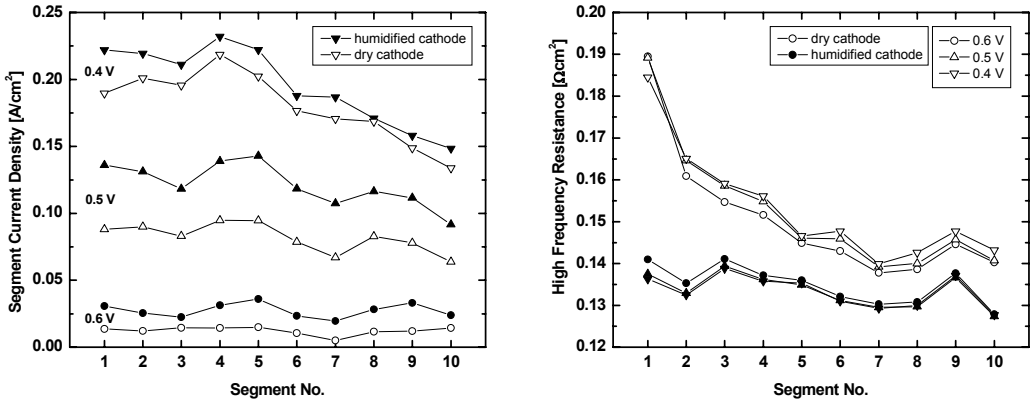

Figure 61: Current and HFR distribution at humidified and dry cathode conditions for various operating points.

4.2.5 Effect of anode and cathode flow rates

Anode flow

Reactant flow rates also impact cell performance. To investigate the influence of anode flow rate on performance, measurements were performed with anode flows ranging from 2 – 20 mL/min. The cathode air flow was humidified at standard temperature. Cathode stoich was the standard stoich of 2.5, so that cathode mass transfer effects were avoided. Resulting DMFC performance and HFRs of the total cell are shown in **Figure 62**. For the anode flow rates investigated, performance was identical for cell operation below current densities of 75 mA/cm^2. At higher current densities concentration polarization started to limit cell performance as a function of anode flow rate. For example, at a methanol flow rate of 2 mL/min cell current density was limited to 100 mA/cm^2. The maximum achievable limiting current density increased with increasing flow. **Table 9** lists theoretical and experimental limiting currents for the four applied flow rates, and the estimated methanol stoichiometry at the limiting current density, respectively. The theoretical maximum current density was calculated assuming that all methanol supplied to the cell could be converted to current. The methanol stoichiometric ratio at the limiting current is the ratio of the theoretical maximum current density to the experimental limiting current density. Discrepancies between maximum theoretical and experimental current densities were due to limitations in methanol access to the catalyst layer or incomplete oxidation within the catalyst layer. Since methanol

crossover is minimal at maximum fuel utilization rates, it is unlikely that it contributed significantly to the observed dicrepancies.

The most noticeable trend in Table 9 was the increasing methanol stoich (at the limiting current density) as a function of flow rate. At 2 mL/min 80% of the input methanol was converted into current, but this amount decreased significantly with anode flow rate. At 20 mL/min only a small fraction (20%) of the input methanol was available for reacting and thus generating the limiting current. This trend may be primarily attributed to carbon dioxide produced due to methanol oxidation. Carbon dioxide production can inhibit methanol access to the catalyst in two ways: (i) CO_2 produced at the electrode physically prevents methanol in the flow channel from reaching the electrode surface. (ii) The gas produced takes up volume within the cell and effectively increases the velocity of the methanol solution in the anode flow channel, thereby decreasing residence time of the methanol in the anode. Depletion of methanol by crossover due to incomplete oxidation is another possibility, but is unlikely significant under limiting current conditions.

The HFR values as a function of flow rate were essentially identical.

Table 9: Theoretical and experimentally determined limiting current densities at various flow rates.

Anode Flow Rate [mL/min]	Theoretical Maximum Current Density [A/cm2]	Experimental Current Density [A/cm2]	Methanol Stoichiometric Ratio at Limiting Current
2	0.12	0.10	1.2
5	0.30	0.17	1.8
10	0.60	0.21	2.9
20	1.20	0.24	5.0

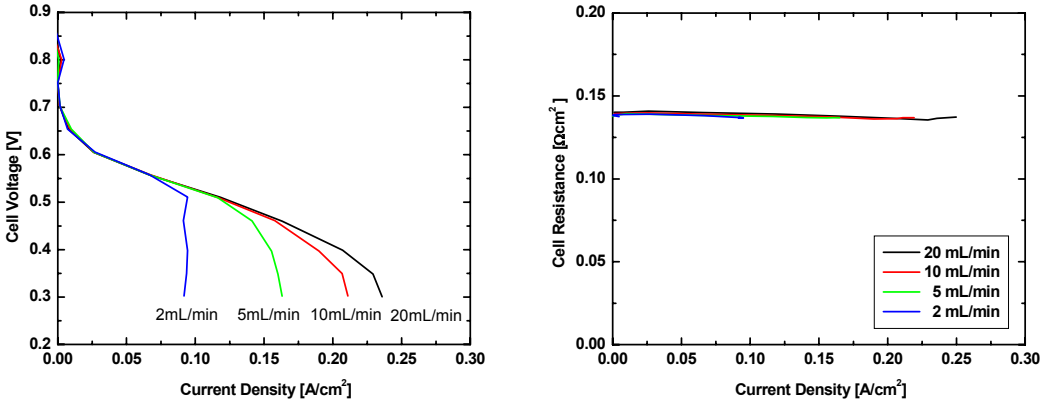

Figure 62: Total cell performance and high frequency resistance at various anode flow rates.

Spatial measurements showing performance distribution as a function of anode flow rate reproduced the results presented for the total cell. The performance and HFR distributions at the four anode flow rates investigated are plotted in **Figure 63** for cell voltages of 0.4, 0.5, and 0.6 V. At 0.6V (low current density, blue), performance was independent of flow rate and showed a slight decrease along the flow-field. At higher current densities significant trends developed as a function of flow rate. At 0.5 V (medium current density, red), 2 mL/min was insufficient to maintain the performance of higher flow rates. The difference in performance was small in upstream segments, but became more pronounced downstream. Methanol availability decreased at an even lower cell voltage of 0.4 V (highest current densities, black). At this operating point, segment performance of the inlet segment Seg01 was dependent on flow rate, indicating concentration polarization impacted performance of the first segment itself. Again the trends were consistent and as expected, increasing in magnitude downstream and with decreasing flow rate.

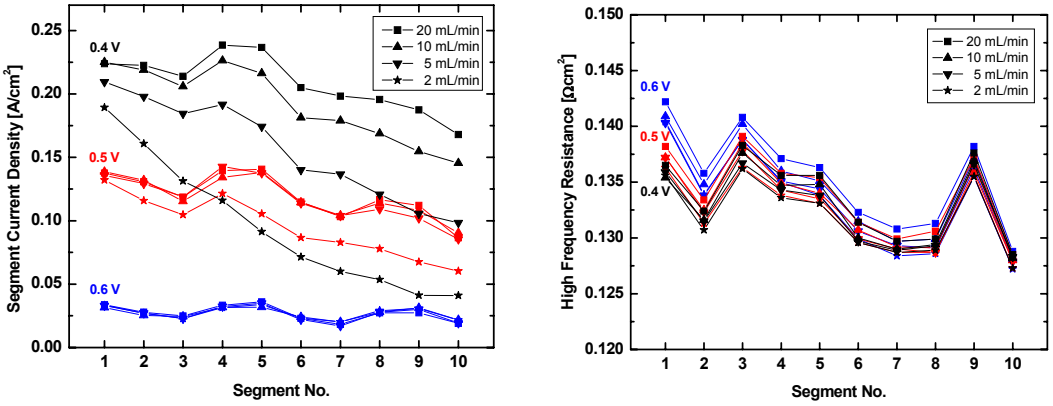

Figure 63: Performance and HFR distribution at different anode flow rates for various operating points.

The data of Figure 63 showed an interesting phenomenon when comparing the results for 2 mL/min at 0.4 and 0.5 V. The performance decay of the at 0.4 V initially better performing inlet segment Seg01, dropped along the flow-field so strongly that the outlet segment Seg10 performed worse than at a cell voltage of 0.5 V. Although performance at the cell inlet increased with decreasing cell voltage, a higher penalty was paid downstream due to fuel utilization. In average however, as comparison to Figure 62 showed, the overall performance was limited by the flow rate and remained constant.

The HFR distribution of the cell showed no changes with anode flow rate. The data showed two general trends: (i) The HFR decreased along the flow channel due to slightly insufficient cathode humidification at 75°C. (ii) HFR values increased slightly with increasing cell voltage. The latter trend might be explained by higher methanol utilization in the anode and therefore a slight decrease in methanol concentration leading to slightly better conductivity. Both trends were not related to anode flow rate, which was not surprising, since the amount of water present at both anode and cathode remained unchanged.

Cathode Flow

While balance of plant losses associated with methanol flow tend to be minor, cathode flow represents the largest parasitic power loss in practical DMFC systems. Therefore, understanding trade offs between performance and efficiency as a function of cathode flow rate is crucial in optimizing DMFC systems. Variation of cell performance and HFR with respect to cathode stoichiometric flow rates is shown in **Figure 64** for dry standard operating conditions. The cell showed very minor performance losses for decreasing air flows ranging from 4.0 to 1.5 stoich. A larger performance drop occurred at a stoich of 1.2. At a current density of 150 mA/cm^2 for example, the cell voltage dropped about 30 mV. HFR values increased with increasing cathode flow, opposing the trend observed for cell performance. The total cell showed minor increases in HFR with

increasing stoich from 1.2 to 3.0 stoich. A larger step of 17 mΩcm^2 occurred between 3.0 and 4.0 stoich. Even though HFR increased with stoich, performance still improved. This was most probably caused by a trade-off between membrane dehydration and oxygen availability at the cathode.

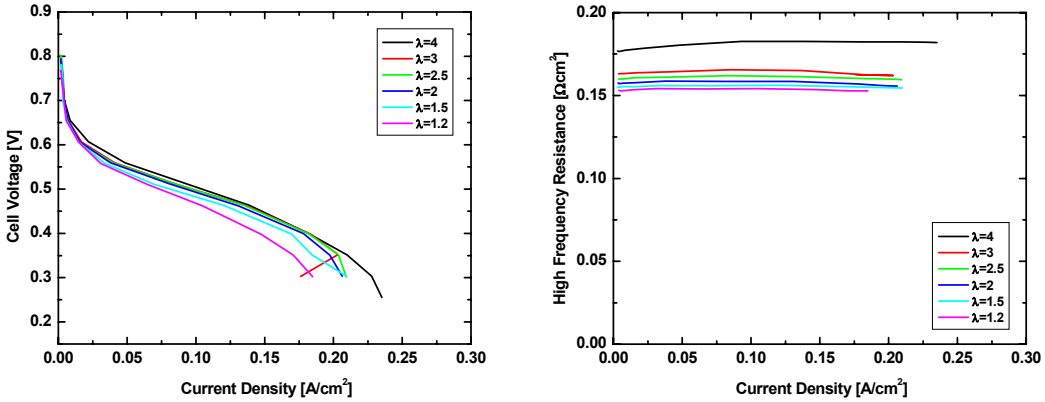

Figure 64: Total cell performance and high frequency resistance at non-humidified cathode and various air stoich.

Performance and HFR distributions of the same measurements are shown in **Figure 65**. All HFR values decreased along the flow-field due to water diffusing to and water production at the cathode. The HFR values of all segments increased with increasing current density or decreasing cell voltage. The results might be explained by the increased relative amount of diffusion compared to electro-osmosis in providing the total water flux through the membrane. At low current densities the amount of water transported through the membrane by diffusion was large, causing the amount of water per air to increase, and leading to improved hydration and decreased HFR.

Segment performance showed strong downstream effects, especially at high current density and low air flow. At 0.4 V, performance of segments downstream segment Seg05 clearly decreased with decreasing stoich and increasing segment number. For segments located closer to the inlet, trends in performance were not as pronounced. At 0.4 V and 4.0 stoich, performance was relatively constant due to trade offs between dehydration and oxygen availability. At the cell inlet (low segment number) lower stoich was advantageous upstream, although performance of the entire cell was still lower. These phenomena have important consequences in determining cell flow rates and flow-field designs.

Trends became more regular at high and medium cell voltages. Performance at 0.5 V was identical at the inlet segment for all stoichiometric flow rates. Progressing downstream, performance dropped with segment number, the lower the stoichiometric air flow, the stronger the performance decay. At 0.6 V, no clear trends were detected along the flow-field. Performance improved with higher stoich.

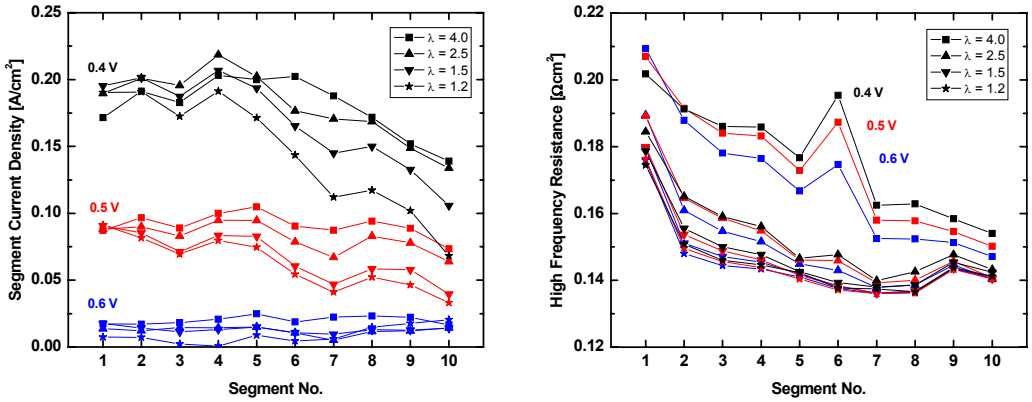

Figure 65: Performance and high frequency resistance distribution at non-humidified cathode and various air stoich.

Figure 66 shows the comparison of the performance distribution of a cathode stoich of 4.0, with a fixed cathode flow rate of 1000 sccm, i.e. very high stoichiometric ratios at low currents. This comparison was emphasized because many researchers report of results measured at fixed flows. It is important to understand how this relates to the more realistic fixed or controlled stoich operation. At the operating conditions presented here cell performance at 1000 sccm fixed flow showed very similar behavior to a stoichiometric flow rate of 4.0. While a stoich of 4.0 was high for a DMFC system, it is still below 1000 sccm for every data point presented here. Typically measurements that employ fixed flow rates operate at the highest expected flow rate, or slightly above.

The high fixed air flow created an unexpected effect at the gas inlet. The HFR of the first three segments seemed largely increased due to a flow effect at the inlet. Clearly, cell performance was still enhanced from Seg03 on downstream, but the strong increase of the HFR for segments Seg01 - Seg03 was detrimental for segment performance at the inlet and may additionally cause endurance limitations.

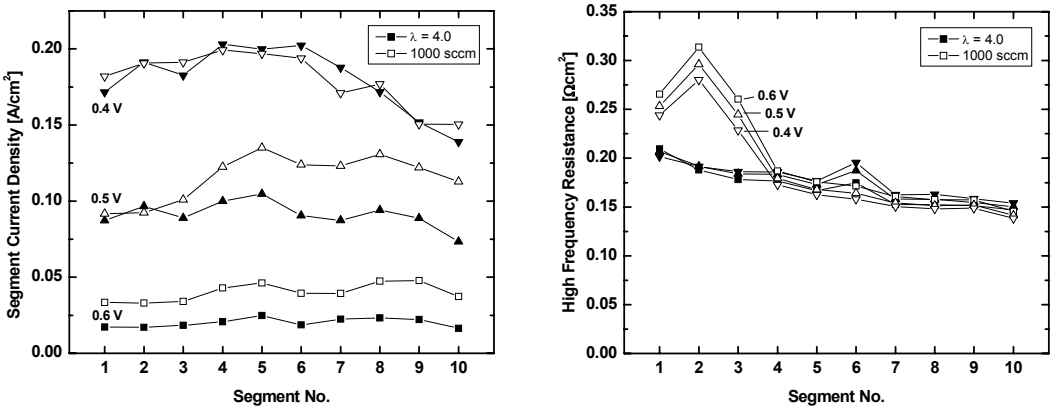

Figure 66: Current and HFR distribution of non-humidified cathode at air stoich of 4.0 compared to 1000 sccm.

5 Summary and Conclusions

This thesis was performed to study spatial effects in hydrogen and methanol powered fuel cells that employ solid polymer electrolyte membranes. Diagnostic tools were a generation three (G-III) and a redesigned and continuously refined generation four (G-IV) segmented cell system. The latter offered significant improvements over previous versions. The segmented cell system allowed spatial resolution of standard fuel cell measurements, such as polarization curves, high frequency resistance, cyclic voltammetry, transients, life tests, AC spectroscopy, crossover measurements, and anode polarization. Segmented membrane electrode assemblies of high homogeneity, high reproducibility, and high endurance were developed simultaneously to the G-IV segmented cell. Together, they formed an effective investigative tool for spatial and temporal PEFC and DMFC research. The system gave exceptional insight into fuel cell processes and allowed evaluation and iteration of fuel cell modeling.

The first part of this thesis focused on the time and space distribution of surface CO and its impact on PEFC performance, measured *in situ* in a fuel cell system. This section of the thesis primarily dealt with non-steady-state states of the fuel cell and time-dependent distribution of the CO in the segmented anode. The study's goal was to provide direct insight into the CO poisoning processes in a real fuel cell system. These findings were expected to improve understanding of the mechanism of CO poisoning and, consequently, to support the development of more CO tolerant fuel cell systems.

The second part of this work focused on segmented cell studies to investigate a number of operating conditions important for DMFCs: (i) methanol concentration, (ii) methanol flow rate, (iii) cathode humidification, and (iv) cathode flow rate. The objective was to qualitatively and quantitatively determine effects along the flow-field as a function of the listed operating conditions and evaluate their importance with respect to DMFC performance. Understanding these effects was expected to help develop strategies and alternative cell designs beneficial for DMFC performance.

Prior to pursuing the research objectives for PEFCs, reference measurements were performed to assure homogeneous performance of all catalyst segments during hydrogen operation. Furthermore, a variety of operating conditions were examined for better analysis of (i) anode and cathode processes, and (ii) cause and effect of processes. Reversing flow direction at one electrode was found to be a very valuable method to separate and identify anode and cathode effects with the segmented cell system. The preparatory studies revealed, for example, that the magnitude of catalyst ripening in a fuel cell is a spatial process that is heavily dependent on the local presence of water. The experience gained during these experiments created the knowledge foundation necessary for investigating time- and space-resolved processes in a PEFC.

Cyclic voltammetry was performed with the G-III segmented cell setup, to study CO adsorption at nanoparticles of carbon-supported Pt catalyst. The measurements focused on non-steady-state states of the anode segment catalyst layers, using an experimental approach to obtain data independent of hydrogen crossover. The charge values of these CO stripping experiments were set in relation to low temperature experiments of the same kind that determined the total number of accessible surface Pt sites. The comparison delivered accurate CO coverage values for each non-steady state experiment. The results of the CV measurements were confirmed by results achieved with CO transient experiments. These experiments were performed with the G-IV segmented cell system. The transient experiments extended the focus of investigating the CO adsorption processes at the anode to studying the steady-state poisoning state of the cell and the recovery processes after saturation of the catalyst layer with CO. Parallel to these experiments, a dynamic and spatial model describing CO adsorption and desorption processes on the Pt catalyst surface was developed by and in close collaboration with T.E. Springer at Los Alamos National Laboratory. The model was experimentally verified and subject to several iterations for best fitting the experimental results.

The results obtained by CO transient and CV stripping experiments indicated that initial catalyst poisoning and saturation of the catalyst layer with CO occurs first at catalyst areas closest to the anode inlet. CO poisoning then continuously progresses along the flow-field from anode inlet to anode outlet as a function of poisoning time and operating conditions. With the onset of CO exposure, the CO molecules do not advance far down the flow-field before they are adsorbed on an available Pt reaction site. The experiments revealed that prior to saturation of the entire cell, the CO coverage gradually decreases from the last saturated segment in downstream flow-direction to the segment closest to the outlet. During fuel cell operation, this causes temporary inhomogeneous performance distribution in the fuel cell. The fuel cell current distribution during such a non-steady state poisoning state was found to be highly dependent on the anode flow rate and the CO exposure time. Currents diminish last in catalyst areas located close to the cell outlet. The observed time period required for saturation of the entire anode with surface CO agreed with the time period needed to reach steady-state poisoning state in a transient experiment of identical operating conditions. Consequently, at steady-state poisoning conditions, the anode surface is saturated with CO with respect to the given operating conditions. In this case fuel cell performance depends entirely on the competition between H_2 oxidation and CO adsorption. At operating temperatures of 80°C, 80-85% of an entire monolayer of CO was completed on the accessible platinum surface. This coverage maintained about 11% of the initial performance, confirming correlation of accessible platinum reaction sites with hydrogen oxidation current density.

The CV experiments further led to the conclusion that low- and high-coverage binding of CO on a carbon supported Pt fuel cell catalyst of nanoparticle size reverses the trend typically observed on low-index planes of Pt, i.e. (111), (110), and (100). High CO coverage limits the mobility of CO on a nanocrystalline Pt catalyst surface and limits the access of water required for the CO oxidation reaction to take place. The surface bond energy of CO adsorbed on the fuel cell catalyst consequently increases with increasing CO coverage. During the non-steady state poisoning state, regular decrease of surface bond energy along the flow field due to decreasing coverage of CO downstream was observed. Entire saturation of the anode however, led to identical and increased bonding strength independent from segment position.

CO adsorption at the anode catalyst surface was found to be influenced by cathode operating conditions. This influence was not associated with oxygen crossover participating in a reaction equivalent to an air bleeding effect at the anode, as stated in the literature, but attested to a substantial role of water in limiting the access of oxygen to the active cathode reaction sites. Adsorption rates accelerated significantly for downstream segments during oxygen co-flow and air counter-flow configuration. At the given operating conditions oxygen crossover was found negligible.

Additional experiments were performed to study the ability of the catalyst to recover from the exposure to CO. During recovery using pure hydrogen, the performance of all ten segments was rapid in the early phase of the process. Later on, the rate and degree of the recovery process depended on the segment location. At the experimental conditions used in this work, CO-poisoned anode catalyst is capable of recovering up to 95% of the initial current once the flow of pure hydrogen is regained. Full recovery was not possible over 93 hours without removal of accumulated surface species by CV. Identification of the surface species remained out of the scope of this work, but may be key to creating an electrode structure capable of fully recovering from CO exposure.

Comparison of the experimental data to a developed model gave rise to refinement of the model and helped to gain additional insight into processes occurring during cell exposure to CO. This comparison triggered the discovery of in-cell conversion of CO to CO_2. This chemical conversion significantly impacted the CO adsorption rate and kept the current distribution during steady state poisoning conditions homogeneous. If this effect can be artificially supported, CO poisoning rates would be effectively decelerated and higher steady-state poisoning currents could be achieved. This would increase the systems tolerance with respect to CO.

The latest iteration of the model is capable of predicting the dynamic and spatial fuel cell response to CO exposure and its subsequent recovery on pure hydrogen feed. The model assumes unchanging local operating conditions at the cathode, while it predicts changes at the anode electrode. An extension of the model to describe dynamic cathode

processes as well, could be very beneficial to more comprehensively describe the observed processes and help identify strategies to increase the system tolerance to CO.

The second part of the presented work effectively demonstrated the ability of the segmented cell approach to investigate performance critical DMFC parameters. Data was presented on the effects of methanol concentration, cathode humidification, and anode and cathode flow rates on DMFC performance. In addition to spatial standard fuel cell measurements, methanol crossover and anode polarization experiments were performed to accomplish the task. The results obtained helped to define viable operating conditions for the given system and showed that the developed G-IV segmented cell system can be used as a valuable design tool. The particular flow-field design of this work was a standard hydrogen flow-field employed for DMFC operation to benefit from the segmented nature of the cell.

The results of the experiments were found valuable for increasing the understanding of a DMFC fuel cell system. Before they can be applied into DMFC development issues, they need to be carefully interpreted, since the trends are true only for the exact hardware and operating conditions reported. They may significantly change by using other flow-field designs, since there is a strong interplay of local operating conditions, hardware and cell performance. Nevertheless, the measurements here can be very useful to, for example, determine a minimum flow rate for DMFC applications with similar flow-fields.

Prior to operating the cell at regular methanol operating conditions, measurements of individually operated segments confirmed particular differences between hydrogen and methanol operated fuel cells. These measurements were intended to be employed as performance references for subsequent experiments. However, the nature of the fuel, i.e. its similarity to water, did not allow for adjustment of identical operating conditions during individually performed segment reference measurements. At any given moment, water and methanol crossing from anode to cathode influences and changes local conditions along the flow-field. The analysis of spatial DMFC processes had to rely on interpretation of results obtained by spatially resolved standard DMFC experiments.

Methanol concentration was found to strongly affect the overall cell performance and its distribution. With respect to methanol concentration, a transition between methanol crossover and concentration polarization as the dominant power loss mechanism in the DMFC was observed with increasing current density. The downstream depletion by methanol crossover and/or methanol utilization has an important influence on the local performance of a DMFC.

Significant attention was given to the methanol flow rate and it was shown that going below certain flow levels at specific operating conditions can significantly impact cell performance. The maximum achievable limiting current density increased non-linearly with increasing anode flow rate. This increase implied that methanol utilization decreased significantly at limiting currents, most likely due to the effects of carbon dioxide production. In general, methanol flow rate is not a critical factor in DMFC design, because the pumps necessary to reach even high flow rates are not large compared to the system. Energy losses associated with pumping a liquid solution are small, especially compared to air pumps. Therefore, DMFC systems should be designed to operate at sufficient methanol flow to achieve the highest performance.

Cathode humidification was found to be beneficial for cell performance. The performance penalty paid due to lack of cathode humidification originated from membrane dehydration, which was detected by increased HFR values. Operating with dry air at the cathode improved internal hydration along the flow-field due to water generated at the cathode or transported through the membrane from the anode. For system design, the costs associated with humidification have to be weighed against potential performance improvements.

Performance losses were observed for decreasing stoichiometric air flow between 4.0 and 1.2 stoich. HFR increased with increasing stoich even though performance increased also. This trend was attributed to oxygen availability being more important at the given test conditions, than membrane dehydration. The current distribution of the cell showed clear downstream performance decay increasing in magnitude with decreasing stoich. The corresponding HFRs decreased along the flow-field due to water produced or transported through the membrane. To optimize cathode flow and reduce the related costs and parasitic losses, the typical operation point of the system is a key parameter.

The interplay of all operating conditions to DMFC performance, no matter if varied during this work or kept constant, does not allow for general statements to be drawn from the specific hardware and operating conditions used here. However, it can be concluded that a trade-off between flooding and drying processes exists in DMFCs that requires a carefully balanced water management to achieve maximum performance. This performance then has to be weighed against other system factors such as parasitic energy losses in determining the optimum operating conditions for a DMFC system.

The experiments and data from the segmented cell operating on direct methanol suggest several valuable research topics as possible targets for future DMFC efforts. The data presented here or other data from the segmented cell would be very useful for model validation as done for CO poisoning processes in the hydrogen fuel cell. The segmented cell would also be useful in flow-field design investigations specific for DMFC and/or

PEFC applications. The employment of a standard hydrogen flow-field, as done in this work, demonstrated the ability to discern general DMFC trends, but could also be used in the optimization and validation of DMFC and/or PEFC flow-field design. Additionally, current controlled measurements are expected to reveal supplementary information about performance distribution and should be considered as an addition to the presented set of measurement techniques.

The segmented cell system as used in this work gives exceptional insight into fuel cell processes and allows evaluation of fuel cell modeling and hardware development. Nevertheless, the research presented in this work simplified the real life operating conditions of a PEFC operating on a reformed hydrocarbon fuel. Future work needs to adjust standard operation to an exposure of about 10 ppm CO, while operating with a standard anode catalyst, such as carbon supported Pt-Ru. Operating at constant cell currents and real anode stoich during the entire measurements would give better insight into practical PEFC processes. The poisoning process would slow down severely and could open the door for discovery of yet unknown processes.

The segmented cell could further be used to focus on fuel cell aging, a process most likely dependent on the water contents in catalyst and gas diffusion layers. It is likely that the hydrophobicity of the gas diffusion layer changes due to long term exposure to water. Since the water distribution gradually changes along the flow-field of the presented segmented cell, aging of individual segments should differ accordingly. Hydrophobicity changes in the gas diffusion layer may be monitored *in situ* by AC impedance spectroscopy, due to changing obstruction of oxygen access to active catalyst sites of the cathode over time. Simultaneously, CV measurements could monitor for catalyst ripening and change of double layer capacity, which should accompany filling of the pores of the gas diffusion layer with water. Such a topic would require standard fuel cell testing, cyclic voltammetry, endurance testing and AC impedance spectroscopy, all methods tested and available with the developed segmented system.

In summary, the segmented cell system can greatly contribute to the scientific community in their endeavors for improving fuel cell understanding and applications, both through work presented here and through future research efforts.

References

[1] C. Stone, A.E. Morrison, *'From curiosity to power to change the world'*, Solid State Ionics, 152–153 (2002) 1-13.

[2] K. Kordesch, G. Simader, '*Fuel Cells and Their Applications*', (VCH Verlagsgesellschaft mbH, Weinheim, 1996) Preface.

[3] Ref. [2] P. 2.

[4] A.J. Appleby, '*The electrochemical engine for vehicles*', Scientific American, July 1999, P. 74-79.

[5] K. Ledjeff, in '*Brennstoffzellen Entwicklung-Technologie-Anwendung'*, (C. F. Müller Verlag, Heidelberg, 1995) P. 25.

[6] L. Carrette, K.A. Friedrich, U. Stimming, '*Fuel Cells: Principles, Types, Fuels, and Applications*', ChemPhysChem **2000-1**, 162-193, (2000).

[7] Ref. [5] P. 27.

[8] J.H. Hirschenhofer, D.B. Stauffer, R. R. Englemann, M.G. Klett , '*Fuel Cell Handbook, Fourth Edition*', (U.S. Department of Energy, Office of Fossil Energy, Federal Energy Technology Center, Morgantown, USA, November 1998) P. 1-3.

[9] Ref. [5] P. 30.

[10] J. Larminie, A. Dicks, '*Fuel Cell Systems Explained*', (John Wiley & Sons, LTD, West Sussex, England, 1999) P. 10.

[11] EG&G Technical Services Inc., Science Applications International Corporation, '*Fuel Cell Handbook, Sixth Edition*', (U.S. Department of Energy, Office of Fossil Energy, National Energy Technology Center, Morgantown, USA, November 2002) P. 1·3-1·5.

[12] J.H. Hirschenhofer, D.B. Stauffer, R. R. Englemann, M.G. Klett , '*Fuel Cell Handbook, Fourth Edition*', (U.S. Department of Energy, Office of Fossil Energy, Federal Energy Technology Center, Morgantown, USA, November 1998) P. 157.

[13] Ref. [12] P. 1-7.

[14] Cabot, North American Technical Report S-136.

[15] M.S. Wilson, F. H. Garzon, K. E. Sickafus, S. Gottesfeld, '*Surface Area Loss of Supported Platinum in Polymer Electrolyte Fuel Cells*', Journal of Electrochemical Society, **140** (10), 2872-2877, (1993).

[16] T. A. Zawodzinski, C. Derouin, S. Radzinski, R J. Sherman, V. T. Smith, T. E. Springer, S. Gottesfeld, '*Water Uptake by and Transport Through Nafion 117 Membranes*', Journal of the Electrochemical Society, **140** (4), 1041-1047, (1993).

[17] S. Gottesfeld, T. A. Zawodzinski, '*Polymer Electrolyte Fuel Cells, in Advances in Electrochemical Science and Engineering*', R. C. Alkire, H. Gerischer, D. M. Kolb, C. W. Tobias (Ed.), P. 202.

[18] I. D. Raistrick, Internal Report, Los Alamos National Laboratory, (1985).

[19] T. E. Springer, T. A. Zawodzinski, M. S. Wilson, S. Gottesfeld, '*Characterization of Polymer Electrolyte Fuel Cells Using AC Impedance Spectroscopy*', Journal of the Electrochemical Society, **143** (2), 587, (1996).

[20] Ref. [17] P. 218.

[21] Ref. [17] P. 203.

[22] F. A. Uribe, T. E. Springer, S. Gottesfeld, *'A Microelectrode Study of Oxygen Reduction at the Platinum / Recast-Nafion Film Interface'*, Journal of the Electrochemical Society **139**, 765, (1992).

[23] P. D. Beattie, V. I. Basura, S. Holdcroft, *'Temperature and pressure dependence of O2 reduction at Pt | Nafion® 117 and Pt | BAM® 407 interfaces'*, Journal of Electroanalytical Chemistry, 468, 180–192 (1999)]

[24] M. Eikerling, A. A. Kornyshev, U. Stimming, '*Electrophysical Properties of Polymer Electrolyte Membranes: A Random Network Model*', J. Phys. Chem. B, **101**, 10807 (1997).

[25] J. Rozière, D.J. Jones, '*Non-Fluorinated Polymer Materials For Proton Exchange Membrane Fuel Cells*', Annual Review of Materials Research, **33**, 503-555, (2003).

[26] O. Savadogo, '*Emerging membranes for electrochemical systems: (I) solid polymer electrolyte membranes for fuel cell systems*', Journal of New Materials for Electrochemical Systems, **1**, 47-66 (1998).

[27] S. J. Paddison, David W. Reagor, T. A. Zawodzinski Jr., '*High Frequency Dielectric Studies Of Hydrated Nafion*', Journal of Electroanalytical Chemistry, **459**, 91 (1998).

[28] G. Gebel, J. Lambard, '*Small-Angle Scattering Study of Water Swollen Perfluorinated Ionomer Membranes*', Macromolecules, **30**, 7914, (1997).

[29] K. Kordesch, G. Simader, '*Fuel Cells and Their Applications*', (VCH Verlagsgesellschaft mbH, Weinheim, 1996), P. 79.

[30] T.A. Zawodzinski, C. Derouin, S. Radzinski, R.J. Sherman, V.T. Smith, T.E. Springer, S. Gottesfeld, *'Water Uptake by and Transport Through Nafion 117 Membranes'*, Journal of Electrochemical Society, **140** (4), 1041-1047, (1993).

[31] K.D. Kreuer, '*On the development of proton conducting materials for technological applications*', Solid State Ionics, **97**, 11-12 (1997).

[32] Ref. [12] P. 6-2.

[33] Ref. [17] P. 271.

[34] S. Thomas, M. Zalbowitz, '*Fuel Cells – Green Power*', US Department of Energy, 1999.

[35] C. H. Hamann, W. Vielstich, *'Elektrochemie II'*, (Verlag Chemie GmbH, Weinheim, Germany, 1981) P. 16.

[36] Fuel Cell Handbook, 6th edition, P. 2-11 ff.

[37] Ref. [5] P. 137.

[38] Ref. [2] P. 151.

[39] A.S. Arico, S. Srinivasan, V. Antonucci, '*DMFCs: From Fundamental Aspects to Technology Development*', Fuel Cells 2001, **1** (2), 133-161, P. 146.

[40] J. Cruikshank, K. Scott, '*The degree and effect of methanol crossover in the direct methanol fuel cell*', Journal of Power Sources, **70**, 40-47, (1998).

[41] S. Wasmus, A. Küver, '*Methanol oxidation and DMFC fuel cells: a selective review*', Journal of Electroanalytical Chemistry, **461**, 14-31, (1999).

[42] Ref. [10] P. 93.

[43] J. Larminie, and A. Dicks, '*Fuel Cell Systems Explained*', (John Wiley & Sons, New York, 2000).

[44] J. J. Baschuk, and X. Li, *'Carbon monoxide poisoning of proton exchange membrane fuel cells'*, International Journal of Energy Research, **25**, 695-713, (2001).

[45] N. M. Marković, C. A. Lucas, B. N. Grgur, and P. N. Ross, *'Surface Electrochemistry of CO and H_2/CO Mixtures at Pt(100) Interface: Electrode Kinetics and Interfacial Structures'*, Journal of Physical Chemistry B, **103**, 9616-9623, (1999).

[46] N. M. Marković, C. A. Lucas, A. Rodes, V. Stamenković, and P. N. Ross, *'Surface Electrochemistry of CO on Pt(111): Anion Effects'*, Surface Science, **499**, L149-L158, (2002).

[47] I. Villegas, and M. J. Weaver, *'Carbon monoxide adlayer sructures on platinum (111) electrodes: A synergy between in-situ scanning tunneling microscopy and infrared spectroscopy'*, Journal of Chemical Physics, **101** (2), 1648-1660, (1994).

[48] K. A. Friedrich, K.-P. Geyzers, U. Linke, U. Stimming, and J. Stumper, '*CO adsorption and oxidation on a Pt(111) electrode modified by ruthenium deposition: an IR spectroscopic study'*, Journal of Electroanalytical Chemistry, **402**, 123-128, (1996).

[49] J. M. Feliu, J. M. Orts, A. Fernandez-Vega, A. Aldaz, and J. Clavilier, *'Electrochemical studies in sulphuric acid solutions of adsorbed CO on Pt(111) electrodes'*, Journal of Electroanalytical Chemistry, **296**, 191-201, (1990).

[50] H. A. Gasteiger, N. M. Marković, P. N. Ross, and E. J. Cairns, *'CO oxidation on Well-Characterized Pt-Ru Alloys'*, Journal of Physical Chemistry, **98** (2), 617-625, (1994).

[51] H. A. Gasteiger, N. M. Marković, and P. N. Ross, *'H_2 and CO Electrooxidation on Well-Characterized Pt, Ru, and Pt-Ru. 1. Rotating Disk Electrode Studies of the Pure Gases Including Temperature Effect'*, Journal of Physical Chemistry, **99**, 8290-8301, (1995).

[52] H. A. Gasteiger, N. M. Marković, and P. N. Ross, *'H_2 and CO Electrooxidation on Well-Characterized Pt,* Ru*, and Pt-Ru. 2. Rotating Disk Electrode Studies of CO/H_2 Mixtures at 62°C'*, Journal of Physical Chemistry, **99**, 16757-16767, (1995).

[53] Z. Jusys, H. Massong, and H. Baltruschat, *'A New Approach for Simultaneous DEMS and EQCM: Electro-oxidation of Adsorbed CO on Pt and Pt-Ru'*, Journal of the electrochemical Society, **146** (3), 1093-1098, (1999).

[54] B. Hammer, O. H. Nielsen, and J. K. Nørskov, *'Structure sensitivity in adsorption: CO interaction with stepped and reconstructed Pt surfaces'*, Catalysis Letters, **46**, 31-35, (1997).

[55] G. A. Camara, E. A. Ticianelli, S. mukerjee, S. J. Lee, and J. McBreen, *'The CO Poisoning Mechanism of the Hydrogen Oxidation Reaction in Proton Exchange Membrane Fuel Cells'*, Journal of the Electrochemical Society, **149** (6), A748-A753, (2002).

[56] L. Gubler, G. G. Scherer, and A. Wokaun, *'Effects of cell and electrode design on the CO tolerance of polymer electrolyte fuel cells'*, Phys. Chem. Chem. Phys., **3**, 325-329, (2001).

[57] J. Zhang, R. Thampan, and R. Datta, *'Influence of Anode Flow Rate and Cathode Oxygen Pressure on CO Poisoning of Proton Exchange Membrane Fuel Cells'*, Journal of the Electrochemical Society, **149** (6), A765-A772, (2002).

[58] S. Cleghorn, C.R. Derouin, M.S. Wilson, and S. Gottesfeld, '*A printed circuit board approach to measuring current distribution in a fuel cell*', Journal of Applied Electrochemistry, **28**, 663-672, (1998).

[59] C. Wieser, A. Helmbold, and E. Gülzow, '*A new technique for two-dimensional current distribution measurements in electrochemical cells*', Journal of Applied Electrochemistry, **30**, 803-807, (2000).

[60] J. Stumper, S.A. Campbell, D.P. Wilkinson, M.C. Johnson, and M. Davis, '*In-situ methods for the determination of current distributions in PEM fuel cells*'**,** Electrochimica Acta, **43** (24), 3773-3783, (1998).

[61] G. Bender, M. Wilson, T.A. Zawodzinski, *'Further Refinements in the segmented cell approach to diagnosing performance in polymer electrolyte fuel cells'*, Journal of Power Sources, **123**, 163-171, (2003).

[62] H.A. Gasteiger, N. Markovic, P.N. Ross, E.J. Cairns, *'Methanol Electrooxidation on Well-Characterized Pt-Ru Alloys'*, Journal of Physical Chemistry, **97**, 12020-12029, (1993).

[63] W.F. Lin, J.T. Wang, R.F. Savinell, *'On-line FTIR spectroscopic investigations of methanol oxidation in a direct methanol fuel cell'*, Journal of the Electrochemical Society, **144** (6), 1917-1922, (1997).

[64] J.-H. Choi, K.-W. Park, B.-K. Kwon, Y.-E. Sung, *'Methanol oxidation on Pt/Ru, Pt/Ni, and Pt/Ru/Ni anode electrocatalysts at different temperatures for DMFCs'*, Journal of the Electrochemical Society, **150** (7), A973-A978, (2003).

[65] H.A. Gasteiger, N. Markovic, O.N. Ross, E.J. Cairns, '*Methanol Electrooxidation of Well-Characterized Pt-Ru Alloys*', Journal of Physical Chemistry, **97**, 12020-12029, (1993).

[66] V.M. Schmidt, R. Ianniello, H. Oetjen, H. Reger, U. Stimming, '*DEMS and Single Cell Measurements of a Direct Methanol Fuel Cell*', Electrochemical society Proceedings, **95-23**, 267-277, (1995).

[67] B.S. Pivovar, '*Electrochemical Selectivity and Electro-osmosis in Direct Methanol Fuel Cell Electrolytes*', PhD dissertation, University of Minnesota, P. 11, (2000).

[68] B.S. Pivovar, Y. Wang, E.L. Cussler, *'Pervaporation Membranes in Direct Methanol Fuel Cells*', Journal of Membrane Science, **154**, 155-162, (1999).

[69] L.J. Hobson, Y. Nakano, H. Ozu, S. Hayase, *'Targeting improved DMFC performance*', Journal of Power Sources, **104** (1), 79-84, (2002).

[70] A. Heinzel, V.M. Barragan, *'Review of the state-of-the-art of the methanol crossover in direct methanol fuel cells*', Journal of Power Sources, **84** (1), 70-74, (1999).

[71] X. Ren, T.E. Springer, S. Gottesfeld, *'Water and methanol uptakes in Nafion membranes and membrane effects on direct methanol cell performance*', Journal of The Electrochemical Society, **147** (1), 92-98, (2000).

[72] B. Gurau, E.S. Smotkin, *'Methanol crossover in direct methanol fuel cells: A link between power and energy density*', Journal of Power Sources, **112** (2), 339-52, (2002).

[73] X. Ren, T.A. Zawodzinski, F. Uribe, D. Hongli, S. Gottesfeld, *'Methanol crossover in direct methanol fuel cells*', First International Symposium on Proton Conducting Membrane Fuel Cells 1, 8 Oct. 1995, Chicago, IL, USA; p.284-98.

[74] S. Narayanan, A. Kindler, B. Jeffries-Nakamura, W. Chu, H. Frank, M. Smart, S. Surampudi and G. Halpert, Proton Conducting Membrane Fuel Cells, eds. S. Gottesfeld, G. Halpert, and A. Landgrebe, Electrochemical Society Proceedings, **95-23**, 261-266, (1995).

[75] S.C. Thomas, X. Ren, S. Gottesfeld, '*Influence of Ionomer Content in Catalyst Layers on Direct Methanol Fuel Cell Performance*', Journal of The Electrochemical Society, **146** (12), 4354-4359, (1999).

[76] H.N. Dinh, X. Ren, F.H. Garzon, P. Zelenay, S. Gottesfeld, '*Electrocatalysis in direct methanol fuel cells: in-situ probing PtRu anode catalyst surfaces*', Journal of Electroanalytical Chemistry, **491** (1-2), 222-233, (2000).

[77] A.S. Arico, P.L. Antonucci, E. Modica, V. Baglio, H. Kim, V. Antonucci, '*Effect of Pt-Ru alloy composition on high-temperature methanol electro-oxidation*', Electrochemica Acta, **47** (22-23), 3723-3732, (2002).

[78] Z.B. Wei, S.L. Wang, B.L.Yi, J.G. Liu, L.K. Chen, W.J. Zhou, W.Z. Li, Q. Xin, '*Influence of electrode structure on the performance of a direct methanol fuel cell*', Journal of Power Sources, **106** (1-2), SI, 364-369, (2002).

[79] J. Nordlund, A. Roessler, G. Lindbergh, '*The influence of electrode morphology on the performance of a direct methanol fuel cell anode*', Journal of Applied Electrochemistry, **32** (3), 259-265, (2002).

[80] J.C. Amphlett, B.A. Peppley, E. Halliop, A. Sadiq, '*The effect of anode flow characteristics and temperature on the performance of a direct methanol fuel cell*', Journal of Power Sources, **96** (1), 204-213, (2001).

[81] M. Neergat, A.K. Shukla, '*Effect of diffusion-layer morphology on the performance of solid-polymer-electrolyte direct methanol fuel cells*', Journal of Power Sources, **104** (2), 289-294, (2002).

[82] C. Lim, C.Y. Wang, '*Development of high-power electrodes for a liquid-feed direct methanol fuel cell*', Journal of Powers Sources, **113**, (1), 145-150, (2003).

[83] M.M. Mench, C.Y. Wang, '*An In Situ Method for Determination of Current Distribution in PEM Fuel Cells Applied to a Direct Methanol Fuel Cell*', Journal of The Electrochemical Society, **150** (1), A79-A85, (2003).

[84] A.B. Geiger, R. Eckl, A. Wokaun, G.G. Scherer, '*An Approach to Measuring Locally Resolved Currents in Polymer Electrolyte Fuel Cells*', Journal of The Electrochemical Society, **151** (3), A394-A398, (2004).

[85] J.-P. Diar, B. Le Gorrec, C. Montella, C. Poinsignon, G. Vitter, '*Impedance measurements of polymer electrolyte membrane fuel cells running on constant load*', Journal of Power Sources, **74**, 244-245, (1998).

[86] J.T. Mueller, P.M. Urban, '*Characterization of direct methanol fuel cells by ac impedance spectroscopy*', Journal of Power Sources, **75**, 139-143, (1998).

[87] T.E. Springer, M.S. Wilson, S. Gottesfeld, '*Modeling and Experimental Diagnostics in Polymer Electrolyte Fuel Cells*', Journal of the Electrochemical Society, **140** (12), 3513-3526, (1993).

[88] M.S. Wilson, S. Gottesfeld, '*Thin-film catalyst layers for polymer electrolyte fuel cell electrodes*', Journal of Applied Electrochemistry, **22** (1), 1-7, (1992).

[89] M.S. Wilson, S. Gottesfeld, '*High performance catalyzed membranes of ultra-low Pt loadings for polymer electrolyte fuel cells*', Journal of the Electrochemical Society, **39** (2), L28-L30, (1992).

[90] M.S. Wilson, J.A. Valerio, S. Gottesfeld, '*Low Platinum Loading Electrodes For Polymer Electrolyte Fuel-Cells Fabricated Using Thermoplastic Ionomers*', Electrochimica Acta, **40** (3), 355-363, (1995).

[91] G. Bender, T.A. Zawodzinski, A.P. Saab, '*Fabrication of High Precision PEFC Membrane Electrode Assemblies*', Journal of Power Sources, **124**, 114-117, (2003).

[92] C.S. Kim, Y.G. Chun, D.H. Peck, D.R. Shin, '*A Novel Process to Fabricate Membrane Electrode Assemblies for Proton Exchange Membrane Fuel Cells*', International Journal of Hydrogen Energy, **23** (11), 1045-1048, (1998).

[93] L.J. Hobson, Y. Nakano, H. Ozu, S. Hayase, '*Targeting improved DMFC performance*', Journal of Power Sources, **140**, 79-84, (2002).

[94] D. Bevers, N. Wagner, M. von Bradke, '*Innovative production procedure for low cost PEFC electrodes and electrode/membrane structures*', International Journal of Hydrogen Energy, **23** (1), 57-63, (1998).

[95] K Bolwin, E. Gulzow, D. Bevers, W. Schnurnberger, '*Preparation of porous electrodes and laminated electrode-membrane structures for polymer electrolyte fuel cells (PEFC)*', Solid State Ionics, **77**, 324-330, (1995).

[96] Y.G. Chun, C.S. Kim, D.H. Peck, D.R. Shin, '*Performance of a polymer electrolyte membrane fuel cell with thin film catalyst electrodes*', Journal of Power Sources, **71**, 174-178, (1998).

[97] C.K. Subramanian, N. Rajalakshmi, K. Ramya, K.S. Dhathathreyan, Bull. Electrochem. **16**, 350, (2000).

[98] S. Moller-Holst, D. Kagaku, **64**, 699, (1996).

[99] A.P. Saab, F.H. Garzon, T.A. Zawodzinski, '*Determination of Ionic and Electronic* Resistivities *in Carbon/Polyelectrolyte Fuel-Cell Composite Electrodes*', Journal of Electrochemical Society, **149** (12), A1541-A1546, (2002).

[100] K. Konoshita, '*Carbon: Electrochemical and Physicochemical Properties*', (John Wiley & Sons Inc., New York, 1988), P. 86.

[101] K.H. Kangasniemi, D.A. Condit, T.D. Jarvi, '*Characterization of Vulcan Electrochemically Oxidized under Simulated PEM Fuel Cell Conditions*', Journal of the Electrochemical Society, **151**, (4), E125-E132, (2004).

[102] F.A. Uribe, T.A. Zawodzinski, '*The Effects of Fuel Impurities on PEM Fuel Cell Performance*', Meeting Abstracts 2001, Joint International Meeting of the Electrochemical Society and the International Society of Electrochemistry 2001, Abstract 339.

[103] M.S. Wilson, personal communication, Los Alamos National Laboratory, Los Alamos, New Mexico, USA, March 4th 2004.

[104] P.M. Piela, personal communication, Los Alamos National Laboratory, Los Alamos, New Mexico, USA, March 4th 2004.

[105] B. Pivovar, F. LeScornet, C. Eickes, C. Zawodzinski, G. Purdy, M. Wilson, P. Zelenay, '*A Six-Cell 'Single-Cell' Stack for Stack Diagnostics and Membrane Electrode Assembly Evaluation*', Proceedings of the Third International Symposium On Proton Conducting Membrane Fuel Cells, 202nd meeting of the Electrochemical Society, October 20-24, 2002, Salt Lake City, Utah, USA.

[106] F. A. Uribe, S. Gottesfeld, and T. A. Zawodzinski, *'Effect of Ammonia as Potential Fuel Impurity on Proton Exchange Membrane Fuel Cell Performance',* Journal of the Electrochemical Society, **149** (3), A293-A296, (2002).

[107] F. A. Uribe, and T. A. Zawodzinski, *'A study of polymer electrolyte fuel cell performance at high voltages. Dependence on cathode catalyst layer composition and on voltage conditioning',* Electrochimica Acta, **47**, 3799-3806, (2002).

[108] T. Zawodzinski, J. Bauman, T. Rockward, B. Müller, T. Springer, F. Uribe, J. Valerio, S. Gottesfeld, '*R&D on Optimized Cell performance for Operation on Reformate and Air*', OAAT Annual Review, June 23-25th, (1999).

[109] X. Ren, T.E. Springer, T.A Zawodzinski, S. Gottesfeld, '*Methanol transport through nafion membranes - Electro-osmotic drag effects on potential step measurements*', Journal of the Electrochemical Society, **147** (2), 466-474, (2000).

[110] J.W. Bauman, T.A. Zawodzinski, Jr., S. Gottesfeld, in '*Proton Conducting Membrane Fuel Cells II/1998*', S.Gottesfeld and T.F. Fuller, Editors, PV 98-27, p.136, The Electrochemical Proceedings Series, Pennington, NJ (1999).

[111] T.E. Springer, T. Rockward, T.A. Zawodzinski, S.Gottesfeld, '*Model for Polymer Electrolyte Fuel Cell Operation on Reformate Feed - Effects of CO, H_2 Dilution, and High Fuel Utilization*', Journal of The Electrochemical Society, **148** (1), A11-A23, (2001).

[112] N. M. Marković, B. N. Grgur, C. A. Lucas, and P. N. Ross, *'Electrooxidation of CO and H_2/CO Mixtures on Pt(111) in Acid Solutions'*, Journal of Physical Chemistry B, **103**, 487-495, (1999).

[113] S. Park, S. A. Wasileski, and M. J. Weaver, *'Electrochemical Infrared Characterization of Carbon-Supported Platinum Nanoparticles: A Benchmark Structural Comparison with Single Crystal Electrodes and High-Nuclearity Carbonyl Clusters'*, Journal of Physical Chemistry B, **105**, 9719-9725, (2001).

[114] R. J. Bellows, E. P. Marucchi-Soos, and D. T. Buckley, *'Analysis of Reaction Kinetics for Carbon Monoxide and Carbon Dioxide on Polycrystalline Platinum Relative to Fuel Cell Operation'*, Industrial & Engineering Chemistry Research, **35** (4), 1235-1242, (1996).

[115] T. Ioroi, K. Yasuda, and Y. Miyazaki, *'Humidity dependence of the oxidation of carbon monoxide adsorbed on Pt/C* and *PrRu/C electrocatalysts'*, Physical Chemistry Chemical Physics, **4**, 2337-2340, (2002).

[116] H. Igarashi, R. Fujino, and M. Watanabe, *'Hydrogen electro-oxidation on platinum catalysts in the* presence *of trace carbon monoxide'*, Journal of Electroanalytical Chemistry, **391**, 119-123, (1995).

[117] Z. Ogumi, T. Kuroe, Z. Takehara, '*Gas Permeation in SPE Method – II. Oxygen and Hydrogen Permeation Through Nafion*', Journal of the Electrochemical Society, **132** (11), 2601-2605, (1985).

[118] T. Sakai, H. Takenaka, E. Torikai, '*Gas Diffusion in the Dried and Hydrated Nafion*', Journal of the Electrochemical Society, **133** (1), 88-92, (1986).

[119] Y.S. Kim, M.J. Sumner, W.L. Harrison, J.S. Riffle, J.E. McGrath, B.S. Pivovar, '*Direct Methanol Fuel Cell Performance of Disulfonated Poly(Arylene Ether Benzonitrile) Copolymers*', Journal of the Electrochemical Society (Batteries and Energy Conversion), submitted February 2004.

APPENDIX A

A. PEFC Spraying

The application of the motor driven doctor blade spreader showed promising results for fabrication of segmented MEAs. In a parallel effort, spray coating of catalyst inks was also examined as a possible alternative to hand painting. To achieve highly reproducible catalyst layer with a spray coating system, automation is preferable to manual application with a spray gun.

The spray application method first gained interest at LANL for fabrication of DMFC membrane electrode assemblies for stack applications. A high throughput of MEAs was necessary for ongoing stack research and development projects, demanding labor intense fabrication of DMFC electrodes by means of hand painting directly onto the membranes. But the efforts to create DMFC electrodes with the in-house developed spray system failed due to physical and chemical properties of the highly catalytic Pt black catalyst. Use of alcohol based solvents, e.g. glycerol and isopropanol, as composites of the spray ink resulted in ignition and combustion of the catalyst layer immediately after spraying. Even if combustion could be avoided during spraying for individual ink compositions, oven drying of the decals at 140°C for removal of the solvents without destruction of the catalyst layer remained an unsolved challenge. Dilution of the inks with inert liquids, e.g. water, led to decreased viscosity of the ink and to catalyst falling out of suspension due to the high density of platinum (21.45 g/cm^3). Agglomerates in the catalyst ink solution clogged up filters, needle valves, and the spray nozzle. Initial good results motivated the efforts to develop the spray system. They were achieved with a semi-manual spray setup and showed identical performance to hand painted DMFC electrodes. These results could not consistently be reproduced with a more complex automated setup.

However, during the search for alternatives to substitute for the hand painting process in the segmented cell project, the existing spray setup at LANL was successfully modified for use with carbon supported platinum catalysts. The setup is shown in the two pictures of **Figure A1**. The left picture shows the complete system including all the peripherals, controls and the N_2 gas tank. The right picture shows a close-up of the spraying apparatus.

Figure A1: Spray setup for carbon supported platinum catalyst at LANL.

The spray ink injection system is located on top of the apparatus. It consists of a syringe infusion pump (Model 100, KDScientific Inc.) and a sonicator (Model CPX, Cole-Parmer Instruments). The syringe infusion pump is excellent for precise, continuous dispersion of small volumes. It is mounted vertically to immerse the 10 ml syringe in a beaker of water together with the micro sonicator head. Operation of the sonicator keeps the catalyst ink inside the syringe in motion and the catalyst particles dispensed. The catalyst ink is pumped to the ultrasonic spray nozzle (Sono Tek Corporation) that atomizes the ink mixture by employing a 60 kHz frequency of adjustable power onto its front horn. A crosscut of the physical embodiment of the ultrasonic spray nozzle is shown in **Figure A2**. The front horn vibration breaks up agglomerated catalyst particles and creates very small drop sizes with a median range of 18 – 68 μm [A1]. Unlike typical spray techniques, the ultrasonic nozzle operates pressureless, i.e. it does not propel the ink towards its target. This creates little tendency for the sprayed material to bounce off the surface into the environment as wasted overspray. As shown in Figure A2, N_2 gas flows through a vortexing gas shroud (Sono Tek Corporation) which embraces the stationary ultrasonic nozzle. The gas carries the mist of the catalyst ink towards the spray target. The target or sample is positioned on a temperature controlled vacuum hotplate (built in-house), which is mounted on an X-Y belt driven positioning table (Model XY-18, Arrick Robotics). The vacuum secures the location of one or more samples on the hotplate and preheats them for accelerated drying of the spray. A mounted ordinary laser pointer in co-operation with a LabView program enables careful calibration of sample position(s) and sample size(s) on the hotplate. During spraying, the program continuously moves the X-Y table including hot plate and samples underneath the spray nozzle in a

selectable rate and spray pattern, e.g. serpentine pattern, in the following referred to as a spray pass. Between passes, the spray pattern is offset by half the spray width to increase the homogeneity of the sprayed catalyst layer.

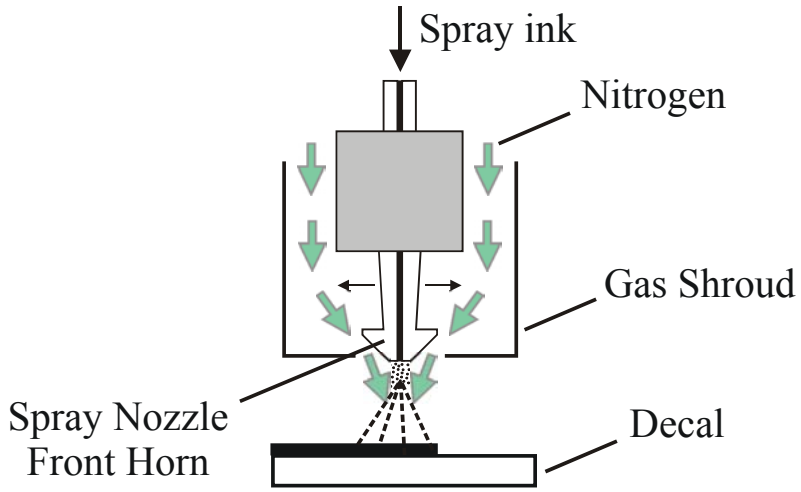

Figure A2: Crosscut through ultrasonic spray nozzle and gas shroud.

Standard spray ink composition contains 20% platinum on carbon (Vulcan XC-72, E-Tek) and 5% Nafion solution (1100 equivalent wt.) in the commonly used catalyst to Nafion mass ratio of 5:2. The ink can either be kept in proton form or be transferred to tetrabutylammonium hydroxide form as is done for the standard hand painting inks. In the latter case, a proton exchange step is needed even if the catalyst layer is sprayed directly onto the membrane. However, the standard catalyst/ionomer mix is diluted by weight ratio of 1:2 with an isopropanol/water mixture of 1:1 by weight. Due to the low density of carbon (2.26 g/cm^3), the overall density of the supported standard catalyst results in 6.10 g/cm^3. This rather low density allows the catalyst to stay homogeneously suspended in the solution. During spray application of the ink, neither settling of catalyst particles nor clogging is observed. Filter devices are not necessary.

The catalyst inks of all presented sprayed MEAs in this work were fed to the spray nozzle with a rate of 18 ml/h. Spray nozzle power was controlled to 3.5 W, and the pressure drop at the gas shroud was typically adjusted to 3 psi. The standard spray pattern was a serpentine pattern with a spray width, i. e. distance between spray rows, of 100 steps of the step motor, which relates to a length of about 5 mm. Offset width between spray passes was half this spray width. The 20 kHz sonicator was pulsed with 240 W pulses at an on:off ratio of 0.2 s:1.0 s. During the spray process the vacuum hot plate was held at a temperature of 50°C; after spraying this temperature was increased for 2 h to 80°C to reassure evaporation of all solvents of the catalyst layer.

Figure A3 shows the surface profile of a sprayed catalyst layer on a polycarbonate substrate. The sample was coated by 6 spray passes and subsequently dried as described

previously. The uniformity of the catalyst layer ranges between that of a hand painted sample and that of a doctor bladed sample. The sample has a continuous base of catalyst layer of 100000 Å at a loading of 0.17 g Pt/cm^2. Measurements of other samples showed that the base thickness of the catalyst material increases with catalyst loading by constant catalyst layer roughness. This prevents inhomogeneous drying of the catalyst layer as observed on hand painted samples. Consequently, no cracking or flaking off of catalyst material occurred over a range of Pt loadings up to 0.6 mg Pt/cm^2.

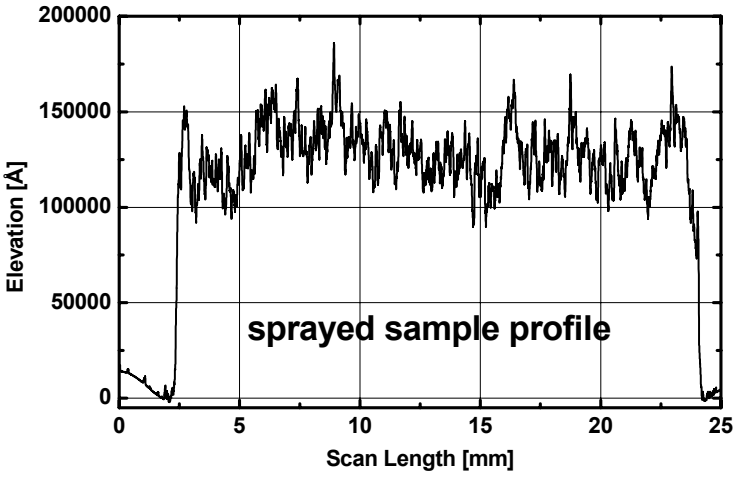

Figure A3: Profilometry of sprayed catalyst layer.

Spraying is by far the fastest application method for PEFC at LANL. Coating and drying of all 10 test samples onto Kapton decals needed about 2.3 hours. Due to the good transfer properties of the Kapton, high reproducibility of the sprayed coat could be adopted from the doctor blade application method and maintained throughout the hot pressing procedure. Excellent reproducibility is obtained if the ink is sprayed onto the membrane material directly. This additionally decreases the interface resistance between membrane and electrode and improves cell performance [A2].

Figure A4 shows a two-dimensional elemental map of platinum of such a sprayed electrode, taken with X-ray microfluorescence spectroscopy (XRMF). The sample, an unused segmented fuel cell anode, was sprayed in proton form (H^+-form) directly onto the membrane. The color distribution of the image reveals highly homogeneous platinum coverage on the individual segments.

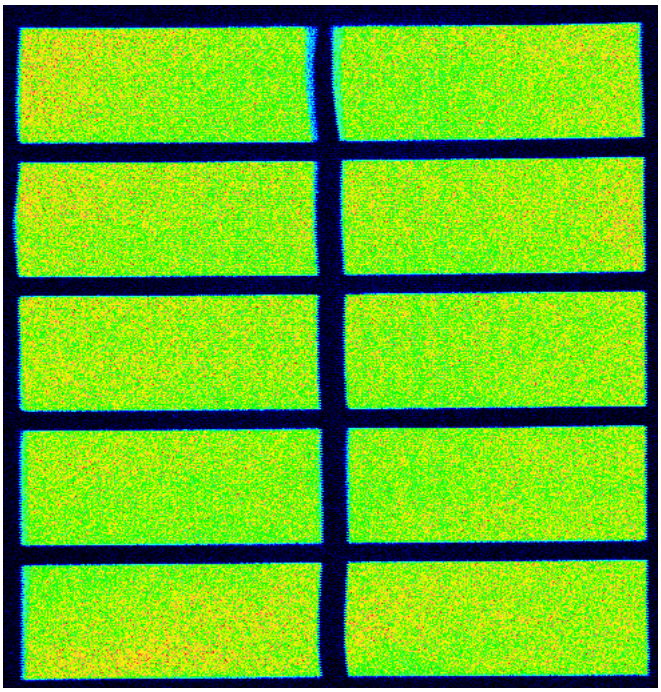

Figure A4: M-line XRF image of Pt in segmented PEFC anode produced by spray coating.

Similar to the Pt loading determination of the doctor bladed catalyst layers, a set of measurements was performed to obtain the correlation between the number of spray passes and the applied Pt loading for the chosen ink composition. The data taken at 5, 7, and 16 spray passes was averaged over 2 measurements each. The results, shown in **Figure A5**, demonstrate linear dependence of Pt catalyst loading with the number of applied spray passes. A fit of the data determines that each spray pass applies 0.036 mg Pt/cm^2. Hence, the spray application method is swiftly adjustable to any desired platinum loading for the found ink composition, but as the experience with DMFC catalysts showed, the adjustment on catalyst material other than carbon supported Pt catalyst of small weight ratios can be a painstaking if not impossible procedure.

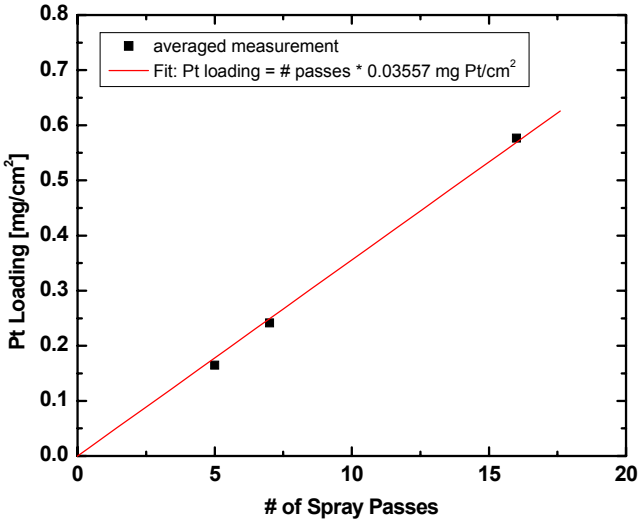

Figure A5: Spray loading as a function of spray passes.

References

[A1] www.sono-tek.com/technology/main_tech.html

[A2] M.S. Wilson, J.A. Valerio, S. Gottesfeld, '*Low Platinum Loading Electrodes For Polymer Electrolyte Fuel-Cells Fabricated Using Thermoplastic Ionomers*', Electrochimica Acta, **40** (3), 355-363, (1995).

APPENDIX B

B. PEFC Operation at Various Conditions

As demonstrated in the previous chapter, the understanding of fuel cell components is essential for engineering fuel cell hardware. Additionally it is necessary to further increase insight in the processes that occur in the catalyst layer, at the catalyst surface and in the gas diffusion layer, to develop strategies to continue lowering catalyst load, and/or increase performance. The following chapter will present investigation of standard PEFC measurements performed spatially by employment of the segmented cell system. Break-in, humidification, anode stoichiometric rates, cathode flow, cathode co- and counter-flow are discussed.

All the measurements presented were performed with a six-channel serpentine flow-field of segmented cell generation 4, as presented earlier. Comparison to a single channel serpentine flow-field was abolished due to the impractical high pressure drop of the segmented single channel flow-field. Measurements of this kind would not have had any practical benefit for fuel cell research and development.

B.1. Break-In

Before a PEFC can be operated at full performance, it needs a time period for start-up, i.e. a time period needed to reach its performance limits. This 'break-in' period is dependent on operating conditions and can last up to 12 hours or longer. During the historical laboratory break-in at Los Alamos National Laboratories (LANL), cells are typically set to a constant voltage of 0.5 V or 0.6 V and the cell is allowed to develop full current capacity overnight. Although the motivation of fuel cell industry should be high to shorten time and cost intensive break-in procedures, this important matter is utterly non-existent in the literature. Solely Saab et. al. [B1] reports of changing ionic and electronic resistance in the catalyst layer during exposure to water vapor. The parallel resistive paths change resistivity in opposing manner. Saab assigned the decreasing resistance to the ionic path, and the increasing resistance to the electronic path.

The left side of **Figure B1** shows the break-in curve of a total cell of MEA type II. Anode and cathode platinum loadings were 0.2 mg Pt/cm^2, catalyst was standard 20% Pt/C from ETEK. The graph contains voltage, current, and HFR of the total cell during the first 20 hours of operation. During this period, cell voltage was kept constant at 0.5 V. The cell needed about 6 - 10 hours to achieve its maximum functionality. This time frame is reproducible at similar operating conditions, but dependent on the chosen cell voltage during the break-in. The starting current of the dry MEA was about 57% of the final current. This is a high initial current value. Starting currents can improve during the break-in period from less than 30% of the final current to full current potential.

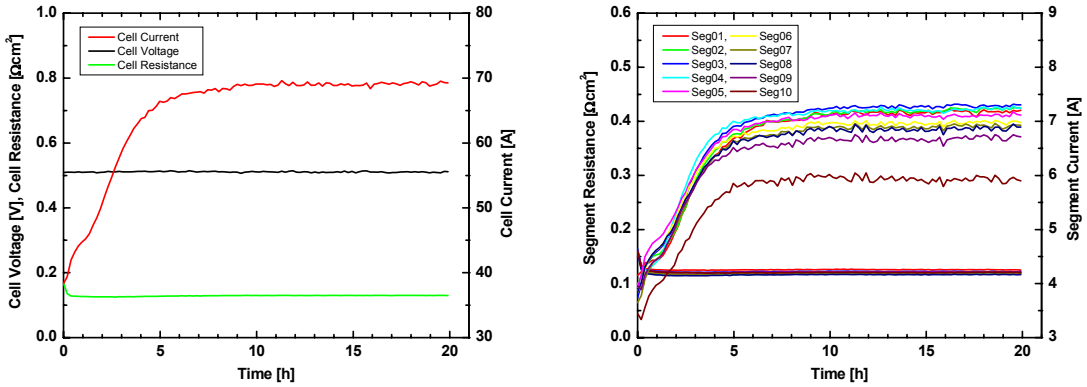

Figure B1: Break-in measurement of segmented cell. Left: Total cell data. Right: Segment data.

Based on the course of the current measurement and start-up of the MEA in dehydrated state, one might conclude that slow hydration of the membrane is causing the break-in period. This premature assumption is rejected by observation of the HFR of the cell. The cell resistance of the total cell changed during the initial half hour of operation only. Henceforth it remained constant and consequently had no influence on the current increase of the cell any more.

The resistance of a material is given by its resistivity ρ and its geometry, i.e. thickness d and cross sectional area A, according to equation (23). Using resistivity values determined for fully hydrated Nafion [B2]-[B3], and catalyst layer geometries treated with a proton exchange and hotpressing production step [B4], the resistances of the employed Nafion N1135 and the recast catalyst layer were calculated for a cross section of 1 cm^2 each.

$$R = \frac{\rho d}{A} \tag{23}$$

Table B1 lists the variables and results of this calculation. The equivalent circuit for the catalyst layer at high frequencies consists of parallel connected ionic and electronic resistance. The electronic resistance is three magnitudes smaller than the ionic resistance and essentially shortens the ionic pathway during the HFR measurement. Consequently, total resistance of the catalyst layer is about three magnitudes smaller than the membrane resistance, which is connected in series, and thus dominates the measured HFR value. Even significant resistance changes of ionic resistivity within the catalyst layer cannot be observed with standard HFR measurement. Cell reaction could still be favored by improvement of local ionic resistivity in the catalyst layer and hence be responsible for the break-in process, but this could not be observed employing the fuel cell setup.

Table B1: Resistances of membrane and catalyst layer of 1 cm^2 area.

	Resistance Type	ρ [Ωcm]	d [μm]	R [mΩ]
N1135	H^+	10	88.9	88.9
Catalyst Layer	e^-	>1	>10	>0.1
	H^+	123	>10	>12.3

The right side of Figure B1 shows the break-in current distribution of the cell. All individual segments showed the same tendencies as the total cell. During the 10 h break-in period segment currents increased from I = 3 - 4 A to final currents of I = 6 -7.5 A. To find a measure for the break-in progress of the individual segment, the 'mid-current' between initial current value and final current value was determined for each segment, including its associated time value, which in the following will be referred to as 'halftime'.

The left part of **Figure B2** shows the segment halftimes of two MEAs during break-in. Both fabrication methods of the segmented MEAs included a hotpressing and proton exchange step for the cathode, and resulted in small deviation of the catalyst loading as reported previously. MEA 1 was of type II, and MEA 2 of type IV. The right part of Figure B2 shows the mid-currents during break-in of the MEAs. The break-in speed gradually increased with respect to segment position along the flow-field. Seg10 of both MEAs reached the mid-current about 30 min earlier than its respective Seg01. Mid-currents of the segments decreased along the flow-field, seemingly with decreasing break-in time. The cells were operated at a constant voltage of 0.5 V, an operating point within or close to the region dominated by concentration polarization. As discussed earlier, mass transport limitation increased along the flow-field due to reaction water production and current densities decrease towards the outlet. The increased presence of water in the catalyst layers may be the cause for increased speed of segment break-in along the flow-field.

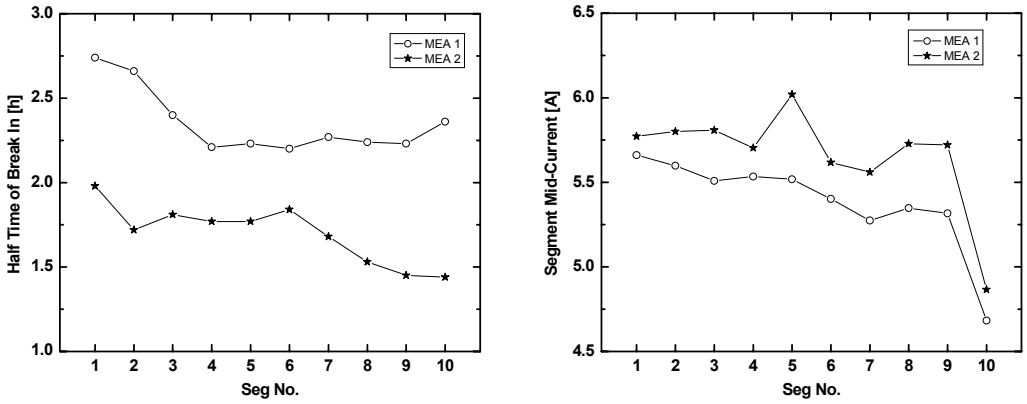

Figure B2: Break in halftimes and mid-currents of segmented MEAs.

The break-in process seems, possibly among other things, to be related to the presence of water within the catalyst layers. Obviously one factor that may slow down cell break-in is drying the MEAs for storage purposes prior to assembling them in the fuel cell hardware. By far the most effective way to quickly and completely humidify recast polymer electrolytes is by immersion in water. Apparently, assembling of saturated MEAs could be beneficial. This is mechanically difficult, since the saturated material dries quickly in air, evoking distortion of the membrane. Wrinkles and folds can develop while assembling the cell and may result in leaks. However, if carefully performed, assembling of a fully water saturated MEA is possible and has been done by T.Q. Rockward at LANL as part of yet unpublished break-in research [B5]. **Figure B3** shows the break-in of an MEA assembled when fully hydrated compared to a standard MEA. Break-in at 0.5 V was accelerated to 5 hours for both MEAs which seemed more related to the employed catalyst (Anode: Pt/C, Cathode $PtCr_3$/C) than to initial membrane hydration.

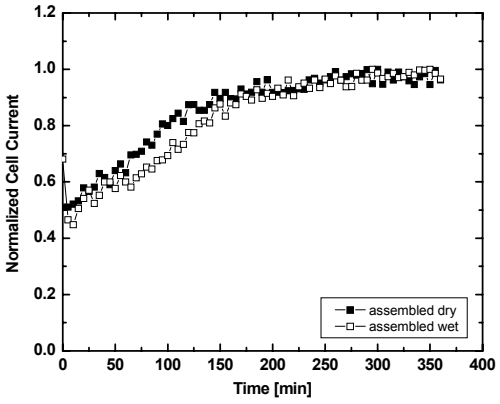

Figure B3: Break-in measurement of MEA assembled in water saturated state.

B.2. Humidification Matrix

Water is also key to maintain high PEFC performance and create good separation properties of the membrane. To establish high protonic conductivity and, consequently, an optimum performance of the cell, a suitable water balance must be maintained in the membrane. This is generally provided through the pre-humidification of the reactant gases and by the water generated during cell reaction. However, changing cell temperature, humidification of the gases, and/or power demands may create unfavorable conditions that could limit the fuel cell system efficiency, e.g. dynamic operational conditions of transportation applications. Thus, it is important to consider the behavior of the cell under non-ideal conditions, i.e. temperatures away from the optimal, current densities that are either very low or very high, etc..

Many recent publications addressed humidification of PEFCs. Some of this work focused on parametric studies and their influence on fuel cell performance [B6]-[B8]. Others investigated the ac-impedance response as a function of operating parameters [B9]-[B10]. A few recognized the dependence of humidification on the employed humidification system. They investigated so called internal membrane-based humidification systems [B11], or the common humidifier bottle that humidifies the gases by means of bubbling it through a heated water reservoir [B12]. Novel strategies to simplify and minimize membrane humidification were also presented. They suggested use of self-humidifying membranes which enclose catalyst material [B13]-[B14], or direct liquid hydration of the anode as the only source of humidification by wicking of the gas diffusion layer and liquid water feed channels in the flow-field [B15]. Most of the published work presented no means to measure cell resistance in situ to use it as an indicator for cell hydration. Performance data was typically interpreted to conclude indirectly on the state of hydration in the cell and to some extent an uncertainty remained with the drawn conclusions.

However the hydration of the membrane was created and maintained in the various projects, the references suggested that humidification and its influence on cell performance was strongly dependent on the individual fuel cell system and MEA. None of the articles discussed that membrane hydration was also a local parameter in the fuel cell. This chapter concentrates on the influence of gas humidification on spatial performance and HFR. The segmented cell response to a humidification matrix of cathode and anode humidifier temperatures around the standard humidification settings for 100 cm^2 cells was determined. Humidifier temperatures were varied in steps of 5°C, from 80 - 105°C at the anode, and 70 - 90°C at the cathode. The cell temperature was 80°C for all measurements and the back pressure was 2 bar for both the anode and cathode. The hydrogen gas flow was set at 1570 sscm equivalent to a stoichiometric flow of 1.1 if the cell was operated with a reformate gas containing 40% hydrogen and a cell

current of 85 A. The cathode operated on air with a fixed flow rate of 3570 sccm air, equivalent to a stoichiometry of 2.5 at 85 A.

The humidifier unit, shown in detail as part of Figure 17, was a hybrid system of membrane humidification and gas bubbler. It hydrated the gas stream (green arrows) by diffusing water through a thin immersed Nafion tube (orange) and bubbling the gas stream through water subsequently. The gas then traveled through a stainless steel pipe heated by the temperature controlled water to prevent condensation. The humidified gas stream after leaving the humidifier traveled a distance of 10 – 15 cm through insulated Teflon tubing before entering the fuel cell hardware. The gas humidification levels of this system, for gas reactant flows that accommodate a cell of 100 cm^2 active area, were determined to be 70% (± 5%) of the saturated water vapor pressure corresponding to each nominal temperature reported [B16]. Consequently, humidifier temperatures might appear rather high, but were necessary at the applied flow rates for sufficient fuel cell hydration.

Figure B4 shows polarization curves (left) and in situ HFR measurements (right) of the total cell operated at two different anode humidifier temperatures (top: 105°C, bottom: 80°C) and various cathode humidifier temperatures. At 105°C anode humidifier temperature, increasing the cathode humidification improved cell performance. Operating the cell at a cathode humidifier temperature equal to cell temperature resulted in lower kinetic performance and slightly less concentration polarization than operating at humidifier temperatures above cell temperature. The HFR measurements along with their better performing polarization curves showed $R_{\square} = 0.105\ \Omega cm^2$, very low values with respect to membrane thickness (Nafion N1135, 88.9 μm), indicating the MEA was well-humidified. At cathode humidifier temperatures lower than cell temperature, the HFR increased. Sufficient humidification was now dependent on internal hydration of the membrane by production of reaction water and its diffusion back into the polymer. At a kinetic current density of 100 mA/cm^2 the HFR reached $R_{\square} = 0.139\ \Omega cm^2$. This increased resistance caused the cell voltage to drop 30 mV. The HFR decreased at higher current densities to $R_{\square} = 0.115\ \Omega cm^2$, but the cell never regained full performance under these humidification conditions.

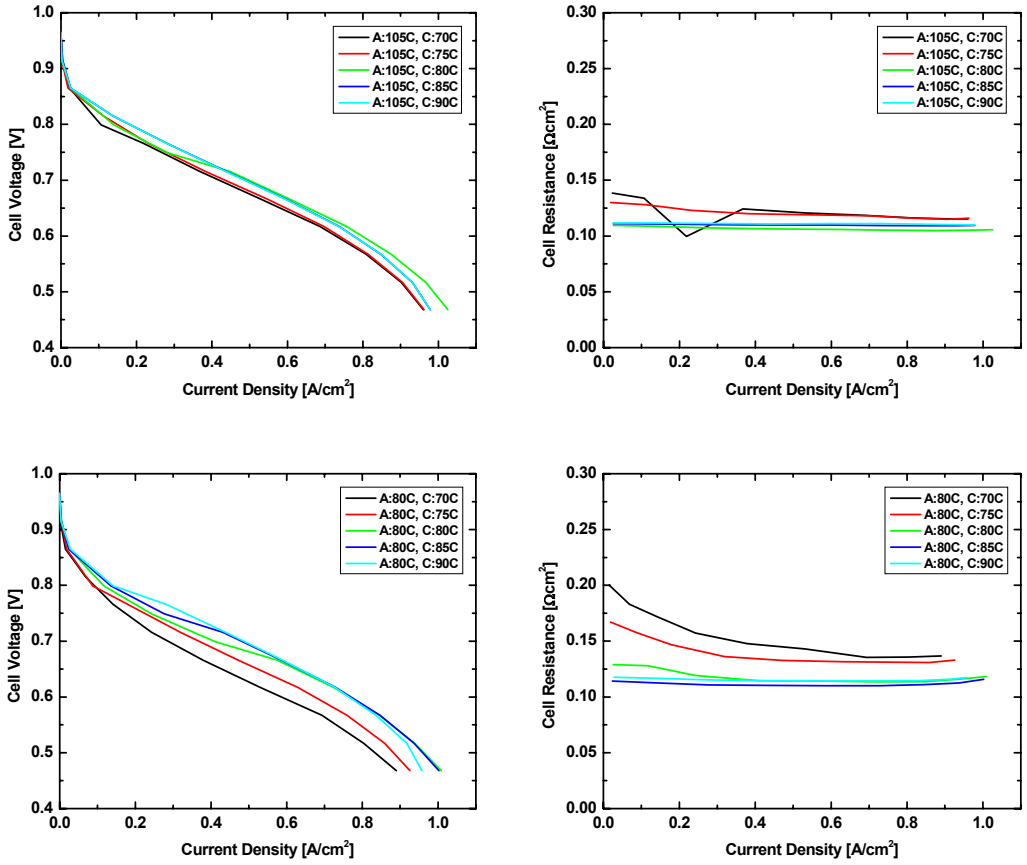

Figure B4: Polarization curves and HFRs of the total cell for constant anode humidifier temperature and varying cathode humidifier temperature.

Operation at increasingly lower anode humidification gradually pronounced the described trends. The bottom graphs of Figure B4 show the recorded data of the lowest anode humidification at varying cathode humidification. Cathode humidifier temperature showed larger effects on cell performance at low anode humidifier temperatures. Although the voltage loss was still identical in the kinetic region, i.e. 30 mV at a current density of 100 mA/cm^2, it doubled in the region dominated by ohmic polarization. At current densities of 500 mA/cm^2 the voltage loss between highest and lowest performing cell was 60 mV. The results were reflected in the HFR measurements. At 100 mA/cm^2 the difference of the HFR value between the best and worst performing humidification conditions was 0.065 Ωcm^2. This difference dropped with increasing current density to 0.034 Ωcm^2 at 500 mA/cm^2 and even further to 0.025 Ωcm^2 at 800 mA/cm^2 due to internal hydration.

The lowest anode and cathode humidification temperatures (80°C, 70°C) resulted again in the highest observed HFR value, i.e. $R_{\square}$ = 0.200 Ωcm^2. This resistance improved with increasing current densities to $R_{\square}$ = 0.137 Ωcm^2. In general, the total cell data

indicated that both, anode and cathode humidification have a strong impact on cell performance based on the given system and operating conditions.

Figure B5 shows similar polarization curves (left) and HFRs (right) at two constant cathode humidifications and various anode humidifications. At cathode humidifier temperatures of 90°C (top) very slight impact on cell performance and HFR values occurred. The polarization curves were very reproducible during variation of anode humidification. The HFR of the lowest anode humidification was slightly increased, without showing a noticeable impact on cell performance. Cathode humidifier temperatures of 90°C seemed to stabilize cell performance. This changed when the cathode humidifier temperature was lowered. The bottom of Figure B5 shows performance and HFR for the lowest constant cathode humidification of 70°C at various anode humidifications. Changing the anode humidifier temperature now impacted cell performance. Kinetic performance was fairly homogeneous. At a current density of 100 mA/cm^2, the cell voltage dropped 11 mV between the highest and lowest anode humidification. At higher current densities this effect increased. At 500 mA/cm^2 for example, the difference in cell voltage amounted to 48 mV, a quite significantly value. Even high anode humidifier temperatures of 105°C could not fully compensate for the lack of hydration in the oxidant feed stream. The according HFR values revealed that the membrane was never sufficiently humidified. Clearly, the cell was paying a penalty in performance due to insufficient cathode humidification. For current densities ≤ 700 mA/cm^2 previously observed HFR values could not be obtained. The lowest HFR value measured $R_{\square} = 0.115\ \Omega cm^2$ in the region of high current densities for 105°C anode humidifier temperature. This value dropped from the original $R_{\square} = 0.139\ \Omega cm^2$ at low current densities due to internal hydration. The highest HFR occurred for anode humidifier temperatures of 80°C and cathode humidifier temperatures of 70°C, see Figure B4.

Evidently operation at humidifier temperatures below cell temperature is detrimental. To achieve and maintain stable operation, humidifier temperatures should be set higher than cell temperature at the given gas flows. Results indicate the most stable performance was achieved at cathode humidifier temperatures of 90°C. Analogue behavior was observed with changing anode humidifier temperature. Anode humidifiers were typically set to 105°C.

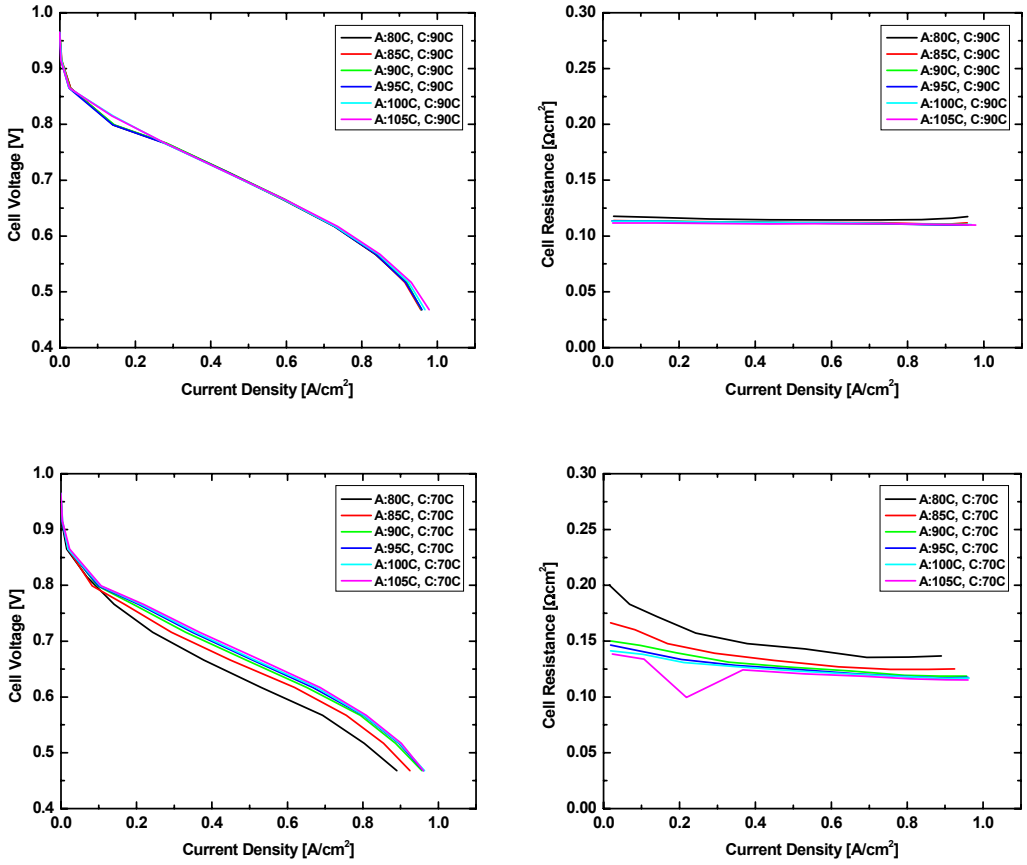

Figure B5: Polarization curves and HFRs of total cell. Cathode humidifier temperature are constant, Anode humidifier temperature are varied.

Figure B4 and Figure B5 presented total cell measurements. Simultaneously, current and HFR distribution in the cell was recorded to investigate the effects of external gas humidification on spatial operating conditions. **Figure B6** shows the kinetic segment current density (left) and HFR (right) data extracted at 0.8 V of the four most extreme humidification conditions and one medium humidification, plotted over the segment number.

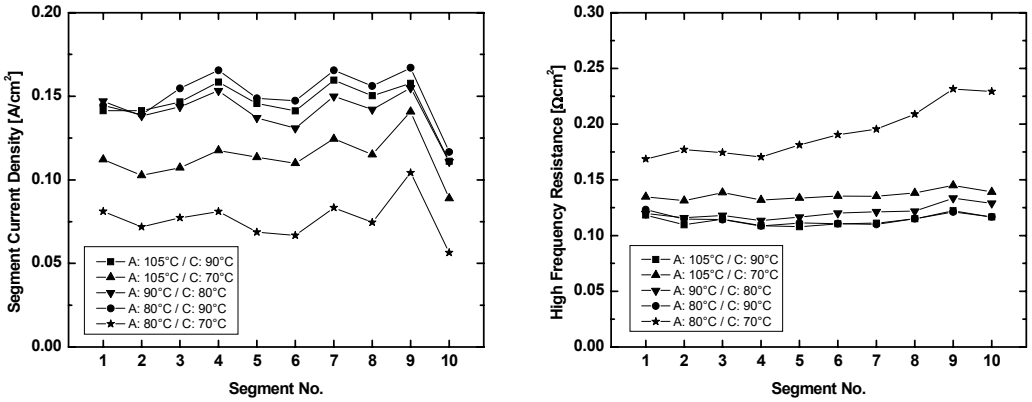

Figure B6: Current density and HFR distribution in the segmented cell at a cell voltage of 0.8 V and various humidification conditions.

At lowest humidification, i.e. humidifier temperatures of 80°C at the anode and 70°C at the cathode, segment performance was constrained to about 75 mA/cm^2 throughout the flow-field. Compensation for the lack of cathode humidification by increase of anode humidifier temperature to 105°C was moderate. The performance could be partly recovered to about 110 mA/cm^2. In both cases, a slight performance increase along the flow channel was observed, probably due to onset of internal hydration. All measurements showed a deviating performance for the last segment Seg10. This may be related to a minor misalignment of this particular segment and was neglected during the discussion of the results.

The cathode humidifier temperatures were increased further to values ≥ 80°C which increased cell performance to about 150 mA/cm^2. The highest performance was recorded at temperatures of 80°C at the anode, and 90°C at the cathode. Again a slight increase was detected along the flow-field during all humidifications. The applied fixed gas flow rates computed into very high stoichiometric flow rates, especially at the low current densities in the kinetic region. Assuming small production of reaction water and negligible gas utilization, cell performance was expected to be constant along the flow-field. The onset of internal hydration may be possible at the given operating condition, but it was surprising that it was distinct enough to be detected.

The segment HFRs increased with decreasing cathode humidifier temperature. As previously discussed, more sufficient humidification should result in HFRs values around $R_{\square} = 0.120\ \Omega cm^2$. Cathode humidification at 70°C increased the high frequency resistance to $R_{\square} = 0.135\ \Omega cm^2$ and $R_{\square} = 0.175\ \Omega cm^2$ at anode humidifier temperature of 105°C and 80°C, respectively. The measured HFR values were fairly constant along the flow-field for most operating conditions. At the driest conditions however, an increase of segment HFR was observed along the flow channel. Values increased up to $R_{\square} = 0.225\ \Omega cm^2$.

Generally, an increase in HFR values was typically due to insufficient cathode humidification, with minimal influence from the anode humidification. But the observed increase of HFR values along the flow-field was not caused by a cathode process. The air flow was not fully saturated, and cathode humidifier temperatures were lower than cell temperature. The air stream should consequently be capable to absorb water from the fuel cell, which is a process membrane humidification systems take advantage of, and not humidify it. Considering the fairly homogeneous current distribution measured at 0.8 V, reasonably identical amounts of water were produced at the cathode interfaces of the 10 segments. If water was absorbed by passing gas, the saturation level of the gas stream would increase downstream. Hence, the potential to further absorb water would decrease along the flow-channel. More water would have remained at the downstream interfaces of the cathode and HFR values should have dropped. This line of thought conflicts with the actual measurements, i.e. increasing segment HFR values at the lowest humidification, and therefore forces the conclusion that the trend may have been caused at the anode.

An anode humidifier temperature of 80°C in combination with a cathode humidifier temperature of 70°C was insufficient to hydrate the fuel cell. Water was permanently absorbed from the fuel stream, humidifying the membrane and balancing water drag as far as possible. This created decreasing water partial pressure along the anode flow-field and consequently an increasingly dry environment at the anode catalyst layers downstream. Since the anode reaction is fast and quite independent on the presence of water, anode performance was not yet spatially influenced at the given conditions. But clearly HFR values increased due to the dry anode catalyst layer and would eventually have caused further penalties for fuel cell performance if the cell hydration was further diminished.

Current density and HFR data were also extracted for lower cell voltages. The discussed trends incrementally changed with decreasing cell voltage resulting in the strongest deviations at low cell voltages. **Figure B7** shows the representative segment current density (left) and HFR (right) data extracted at 0.5 V plotted versus the segment number. Shifting the cell voltage towards the lower value increased the current density of the 10 segments by an order of magnitude. Segment performance first increased along the flow-field to a maximum value. This value was typically maintained through segments Seg03 - Seg05. It then decreased monotonically toward outlet segment Seg10, dropping in average 50 mA/cm^2 per segment from maximum current densities of 1.05 A/cm^2 to minimum values of 0.8 A/cm^2.

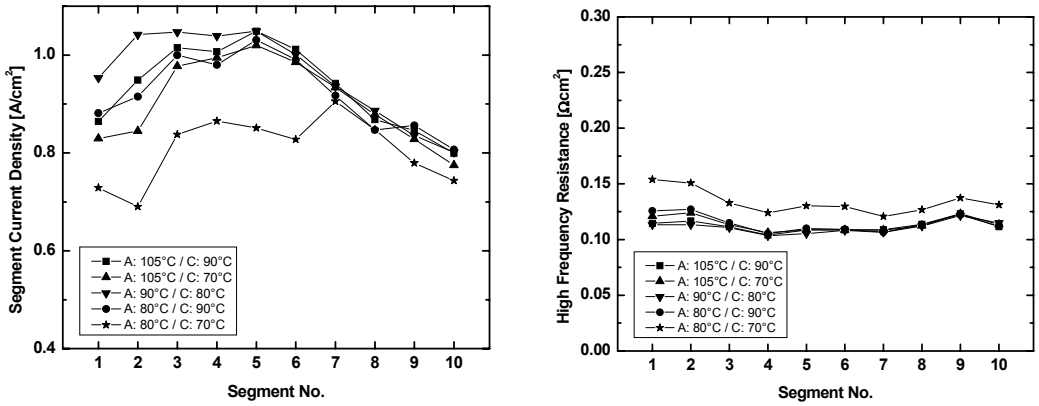

Figure B7: Current density and HFR distribution in the segmented cell at a cell voltage of 0.5 V and various humidification conditions.

Performance of the inlet segment Seg01 was dependent on the water saturation of the gas streams. Poor cathode humidification resulted again in the smallest current densities. Performance of Seg01 increased with improved humidification. The best results were achieved for 90°C anode and 80°C cathode humidifier temperatures. Downstream of Seg01 internal hydration first improved segment performances down to Seg06, and then worsened it down to the outlet during all humidification conditions. Segments Seg02-Seg05 benefited from the number of preceding segments. Their performance increased over the course of several segments depending on the strength of humidification. From about Seg06 on, performance decayed downstream. Inherently, too much reaction water began flooding the gas diffusion layers downstream and reduced access of oxidant to the reaction area.

The related HFR values indicated that the MEA was well hydrated in all but the driest humidification condition. The first four segments showed a decrease of HFR value downstream, due to internal hydration and reaction water produced. The resistance values for these segments dropped from about $R_{\square} = 0.125\ \Omega cm^2$ to about $R_{\square} = 0.105\ \Omega cm^2$. This drop was less pronounced at more favorable humidification. Downstream of segment Seg04, HFR values stayed fairly constant until Seg07. Then they slightly increased again, probably caused by drying anode catalyst layers. Dry humidification conditions elevated the segment HFR throughout the cell by 0.025 - 0.030 Ωcm^2. HFR dropped considerably along Seg01 – Seg04, but internal hydration could not completely compensate the lack of humidification and thus performance did not recover.

The observed trends did not correspond with the baseline measurements previously presented in Figure 16. Both experiments employed strongly different anodic gas flows, which resulted in different supplied water amounts per time sequence. Consequently, the water saturation level of the hydrogen was smaller during the recording of the

temperature matrix, revealing anode humidification processes that occur at drier operating conditions.

The observed trends at current densities of about 1 A/cm^2 were identical to measured data presented by Berg et. al. which addressed modeling of water management issues for different flow configurations and humidifications [B17]. The authors ascribed the performance distribution during co-flow configuration to significant water transfer from cathode to anode at the first 8 cm of flow channel. Dry anode hydration at the cell inlet may be responsible for the measured data trends, but theoretical and experimental data deviated significantly. Berg et. al. predicted a strong increase of the performance in the first 5 cm of the flow channel, followed by a continuous performance decrease. The performance and HFR values of our measurements showed slower humidification along the flow channel. The cell reached its minimum resistance over the course of four segments, i.e. 21.8 cm flow channel, from segment Seg01 – Seg04. The model predicted that HFR values were increased at the cell inlet, confirming that an anode process may be responsible for increased HFR values at the cell inlet.

Repetition of the temperature matrix showed an interesting and unexpected artifact caused by elongated operation. Prior to the experiment, this cell operated at a constant voltage of 0.6 V for 263 hours. **Figure B8** shows segment current densities and HFR values plotted versus segment number at 0.8 V and medium to dry humidification. Kinetic performance of this cell dropped continuously from inlet to outlet, a previously non-existant phenomena, which could not be attributed to utilization of the gases, since very high stoichiometric flow rates were applied. Contrary to the current densities, the HFR distribution along the flow-field reproduced the previous results. Hence, a change in humidification had to be excluded as a possible explanation.

During the lifetest all ten segments performed at similar high currents around 6.5 - 7 A. Depending on their location along the flow channel, the segments were subject to gradually increasing exposure of reaction water, as discussed previously. It is known that supported platinum catalysts of PEFCs suffer from surface area loss during prolonged operation. The particle growth of platinum dispersed on Carbon is significantly accelerated in the presence of a liquid environment [B18]. This mechanism was held responsible for loss of surface area during endurance tests on PEFCs, but the loss of active catalyst area was considered negligible in the kinetic region [B19]. The combination of long term operation and an increasing presence of water along the flow-field suggested that the observed impact on cell performance at 0.8 V may be caused by catalyst ripening and that indeed the local kinetic performance is affected by catalyst surface area loss.

This effect would be very difficult to observe with single cell technology. The segmented fuel cell system offers exactly identical operating conditions with an implemented integral increase of water along the flow-field at higher current densities. It

is the optimal system for this kind of investigation provided the measurement system offers sufficient accuracy.

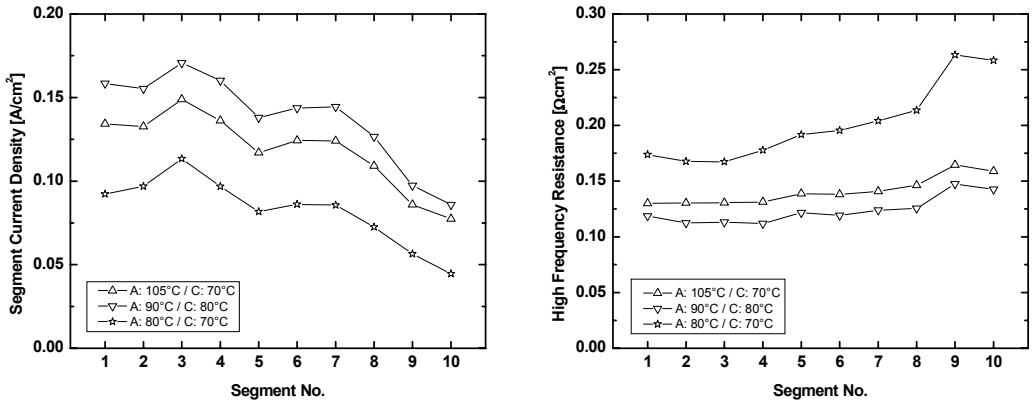

Figure B8: Current density and HFR distribution in the segmented cell at cell voltage of 0.8 V and dry cathode humidification conditions after 263 hours of operation.

The variation of the humidifier temperatures for anode and cathode resulted in a humidification matrix that could clearly emphasize the importance to optimize humidification at both electrode sides for the given system. Membrane hydration was the main cause for performance deviation, and was proven to be directly related to the humidification of the gas streams. HFRs measurements presented evidence that performance was also strongly influenced by internal hydration. The measurements showed that local performance is a function of humidification and consequently the presence of both produced and introduced water along the flow field. Performance gradients were not constant along the flow-field. At sufficient current densities, lack of water could quickly switch to excess of water, completely changing the dominating loss mechanism of the cell. Also, the very high flows and the relatively poor saturation of the gases of our system may have been contributing to stronger inlet effects than usual, i.e. operating at stoichiometric flows at anode and cathode sides.

Emphasizing the importance of humidification for one electrode or the other as done in the literature did not appear sensible. The influence of the humidifier conditions is far too dependent on the system and system parameter to conclude in general statements. Fuel and oxidant humidifications were generally found essential to optimize performance of the presented segmented system. Favorable humidification conditions consequently need to be determined for each system individually, considering the operation point or the range of operation points and their respective system efficiencies.

B.3. Anode & Cathode Flow Conditions

Fuel cell system efficiencies are also dependent on system pressure, gas utilization and gas flow rates. Utilization of hydrogen directly impacts system efficiency and becomes a challenge when the hydrogen source is a reformate gas mixture produced from reformed hydrocarbon fuel. The hydrogen then has to diffuse through nitrogen and carbon dioxide to reach the reaction area and fuel utilization of 90% or more becomes difficult [B20]. In this work undiluted hydrogen fuel was supplied to the fuel cell only. Hence, hydrogen utilization was not expected to be problematic for the presented research projects.

Cathode flow rates impact the system performance and efficiency also. High flow rates can, for example, prevent flooding of gas diffusion layers but also require energy to operate blower and/or compressors. In the following chapters experiments are presented and discussed that focused on the influence of (i) stoichiometric hydrogen flow rates, (ii) the flow configuration of the cell, and (iii) the cathode flow rate.

B.3.1. Anode Stoich

Figure B9 shows representative polarization curves and HFR measurements of the segmented cell at stoichiometric anode flows of λ = 1.1, 1.5 and 2.0. Airflows were set to 4000 sccm, humidifier temperatures were 105°C at the anode and 80°C at the cathode, respectively, cell temperature was 80°C, and cell pressure was 2 bar at both electrodes. To ensure constant anode operating pressures throughout the measurements, stoichiometric tracking started at a minimum flow of 100 sccm. Thus tracking was applied only above current densities of 169, 124, and 93 mA/cm^2 for λ = 1.1, 1.5 and 2.0, respectively. At lower current density values, higher stoich applied.

The recorded total cell polarization curves obtained at the three stoichiometric ratios were identical. At kinetic current densities, the HFR values deviated. Stoichiometric ratios of the measurements increased at the current limits mentioned above, but overall flow did not vary. The change of the HFR values in this region was rather surprising and unexpected. At currents densities above 270 mA/cm^2 internal hydration did participate enough to fully hydrate membrane and catalyst layers. The cell had identical HFR values of 0.11 Ωcm^2 or lower at all stoichiometric ratios.

The impact of stoichiometric hydrogen flow on segment performance and HFR values could be considered negligible. But operation with reformate fuel would significantly change the dependence on stoichiometric anode flow rates. Performance losses would consequently be expected and a separate investigation would be necessary to understand the processes for this operation mode.

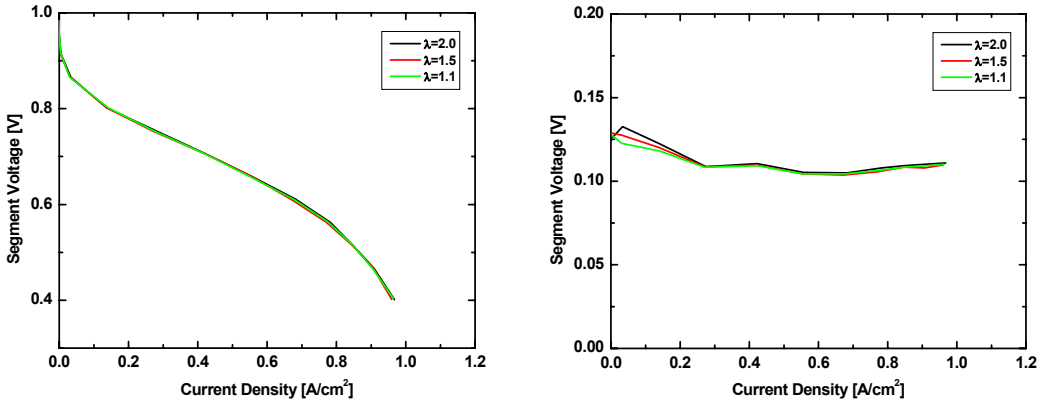

Figure B9: Polarization curves and HFR measurements of the total cell at different stoichiometric anode flows.

Figure B10 shows the current and HFR distribution of the presented measurements at 0.8, 0.6, and 0.4 V. The performance trends along the flow-field followed the previously observed patterns. Throughout the applied stoichiometric flow rates, cell performance stayed fairly constant. At kinetic current densities for example cell performance slightly improved at an anode stoich of 1.1. The performance increased up to 10 mA/cm^2 with respect to the recorded current densities of a stoich of 2. The distribution of HFR values showed, that the small enhancement originated from an improved resistance at low stoich flow. Before onset of internal hydration, saturation of the feed streams was the only source of water to humidify the cell. Decreasing the hydrogen flow increased the residence time of the fuel in the humidifier bottle and hence created higher gas saturation. As a consequence, the HFR of the cell decreased up to 10 mΩcm^2, about 10% of the measured resistance value. With onsetting internal hydration at higher current densities, the observed resistance deviation decreased significantly. Resistance differences between highest and lowest stoichiometric flow dropped below 2 mΩcm^2, a negligible value which indicated identical hydration at and above intermediate cell current densities.

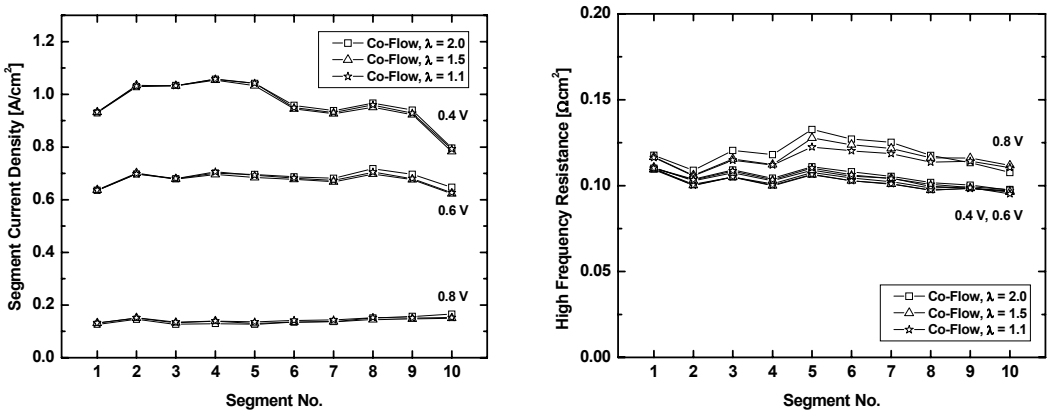

Figure B10: Current density and HFR distribution of segmented cell operated at three different anode stoichiometries.

B.3.2. Co- and Counter-Flow

One additional parameter was added to the variation of the anodic flow rates. The direction of the gas flows with respect to each other is likely to impact total and/or local cell performance, by changing local hydration of the cell. To permit testing this, the segmented cell system was designed to allow rotation of one flow-field in steps of 90 ° with respect to the other. The system enabled testing of co- (standard), counter-, and cross-flow as illustrated in **Figure B11**.

Comparison of the cell performance of these different flow strategies with the standard co-flow is meaningful, but only the counter-flow configuration allows direct comparison without disassembling the cell. Spatial interpretation of cross-flow data would be extremely challenging, since anode and cathode downstream effects mix in difficult patterns without the possibility to isolate and identify them. In the following chapter we investigate the impact of counter-flow on the performance distribution of the segmented cell at three anode stoichiometric flow rates.

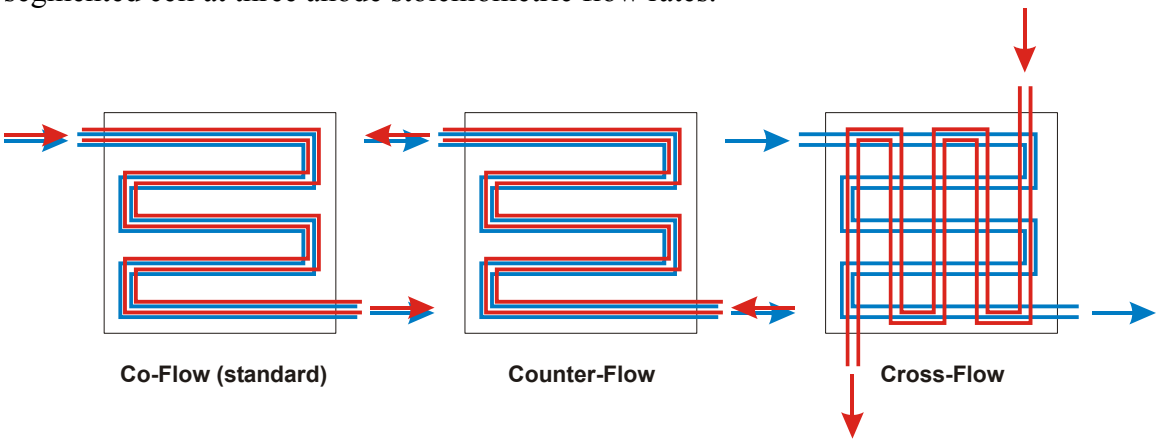

Figure B11: Schematic of various flow patterns in a fuel cell hardware.

To reverse the cathode flow of the segmented cell, a four way valve was installed connecting the incoming gas line, the fuel cell inlet, the fuel cell outlet, and the exhaust line in such a way, that turning the valve switched direction of the gas flow through the fuel cell cathode. The schematic of this setup is presented in **Figure B12**. The valve allowed switching the flow direction during fuel cell operation, without shutting down the cell, i.e. avoiding depressurizing, cooling down humidifiers and cell, and interrupting gas flows, before air feed and exhaust line can be exchanged. The gas flow through the cell during standard co-flow configuration was running downwards from flow inlet to flow outlet, in the counter-flow configuration the cathode outlet became physically the inlet and vice versa. In the following the segment notation will be kept according to standard flow direction, i.e. unchanging segment order from anode inlet to outlet.

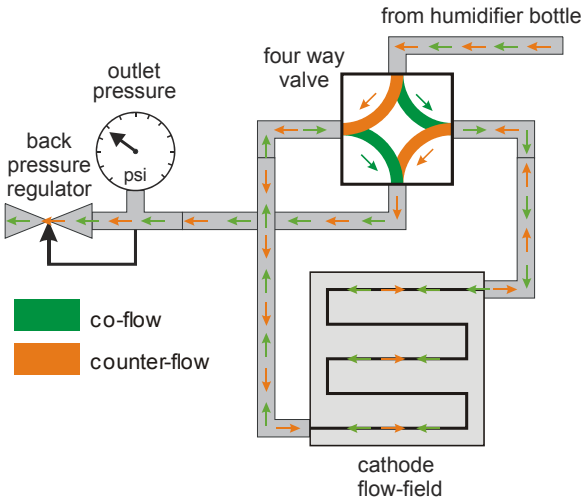

Figure B12: Schematic of setup to switch between co- and counter-flow.

Figure B13 shows polarization curves and HFR measurements of the segmented cell in counter-flow configuration at anode stoichiometric flows of $\lambda = 1.1$, 1.5, and 2.0 in comparison with one co-flow measurement recorded at $\lambda = 1.5$. Reversing the air flow had no visual effect on the performance of the total cell, but the HFR values at $\lambda = 1.1$, and 2.0 seemed increased in the kinetic region.

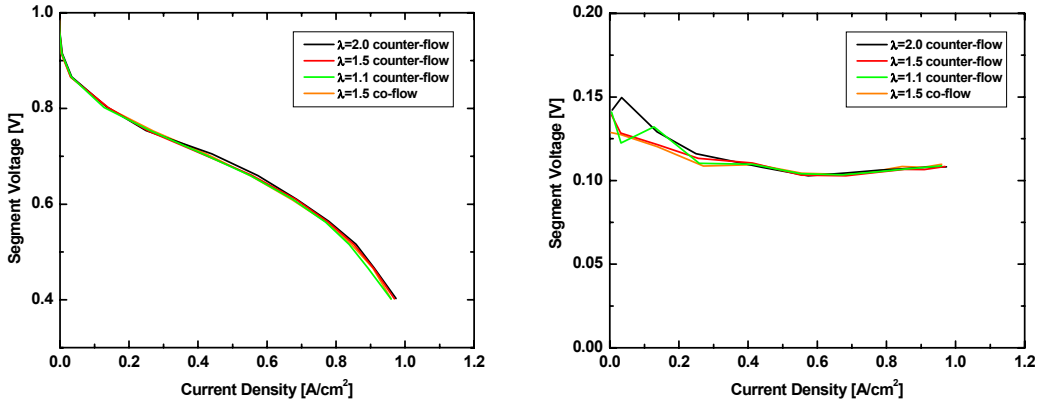

Figure B13: Total cell polarization and HFR measurements before, during, and after switching from co-flow to counter-flow and back.

The performance and HFR distribution of the cell for counter-flow configuration is shown in **Figure B14**. Reversing the air flow changed the performance pattern of the cell, especially noticeable in the high current region at 0.4 V. Slight performance changes occurred with variation of the stoichiometric anode flow, similar to the ones discussed for co-flow configuration as presented in Figure B10. At kinetic current densities, i.e. 0.8 V, the recorded HFR values were clearly elevated and increasing along the flow-field from segment Seg01 - Seg10. Note that the HFR changed non-linear with the stoichiometric anode flow at all current densities. The lowest values were measured for a stoichiometric flow rate of $\lambda = 1.5$. The HFR values differed up to 17 $m\Omega cm^2$ compared to higher and lower stoich of 2 and 1.1, recorded in the mid-section of the cell at segments Seg05 – Seg08. Smaller deviation occurred at the cell inlet and outlet.

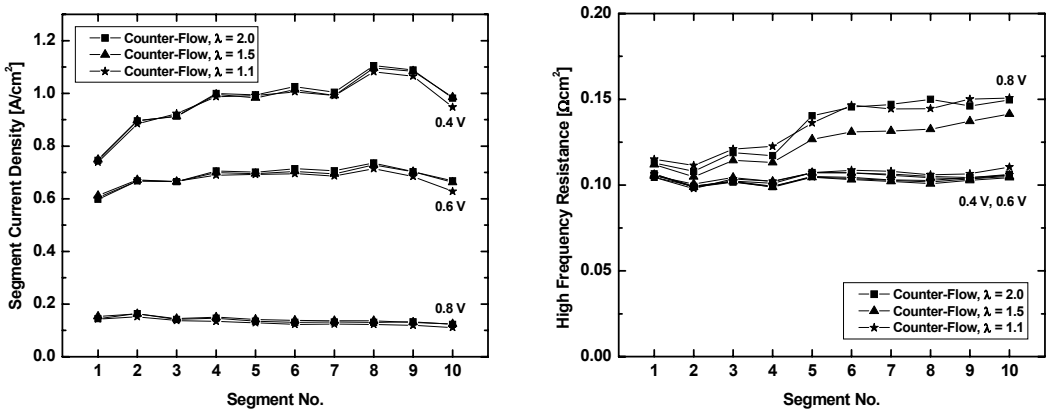

Figure B14: Current density and HFR distribution of segmented cell operated in counter-flow configuration at three different anode stoichiometries.

Direct comparison of co-flow and counter-flow configuration at a stoich of 1.5 is shown in **Figure B15**. The direction change of the cathode flow inversed the performance

pattern of the cell. At high current densities, the performance pattern switched from an increase of the performance along the flow-field to a decrease of the performance; at low current densities vice versa.

Two cathode processes impacted the cell performance at the given operating conditions: (i) In the kinetic region losses occurred due to dehydration of segments Seg06 – Seg10. (ii) At higher current densities internal hydration compensated for the lack of water in the gas stream but mass transport limitation dominated the performance distribution. Performance first slightly increased, and then dropped from cathode inlet at Seg10 to cathode outlet at Seg01.

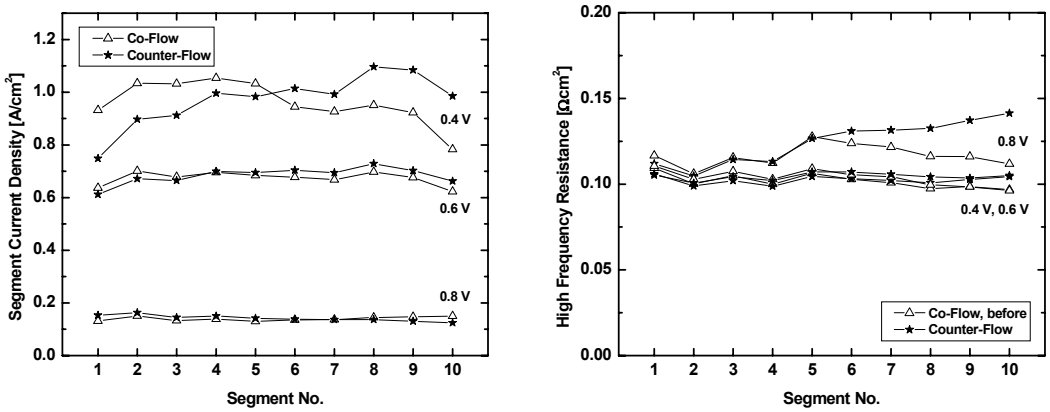

Figure B15: Current density and HFR distribution of segmented cell operated in co- and counter-flow configuration.

Although altering the cathode flow direction could not enhance cell performance, it was found to be of analytical value. **Figure B16** shows the performance and HFR distribution of a cell at 0.8 V in co- and counter-flow configuration measured after 263 h of operation. Reversal of the cathode flow showed minor impact on the previously observed performance and HFR trends along the flow-field (Figure B8). The kinetic performance and HFR pattern along the flow-field proved independent from the flow configuration of the cell, evaluating their possible origin in structural changes of the catalyst. The HFR values of Seg05 – Seg10 additionally decreased in counter-flow configuration, implying improved humidification at the cathode inlet. To further consolidate the drawn conclusion, the disassembled segmented MEA was sent to Oakridge National Laboratory for investigation of the structural composition of the catalyst layer.

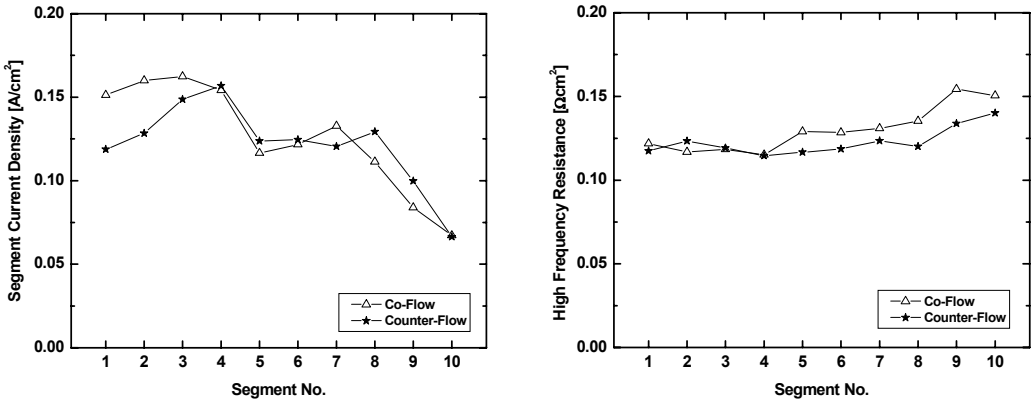

Figure B16: Current density and HFR distribution in the segmented cell at 0.8 V after 263 hours of operation.

B.3.3. Cathode flow

In contrast to changing the anode stoichiometric flow rate, changing the cathode flow rates was expected to significantly alter performance and performance distribution. **Figure B17** shows polarization curves and HFRs of the total cell at various constant cathode flow rates ranging between 1.6 – 5.7 L/min. At all current densities the stoich ratio was higher than 1.1.

Above current densities of 300 mA/cm^2 cell performance began to divert with changing cathode flow rates. This was particularly apparent at current densities above 800 mA/cm^2. At 0.47 V, current densities varied between 0.84 – 1.27 A/cm^2. The higher air flows removed water more aggressively from the gas diffusion layer, enhancing oxygen access to the three phase interface. Simultaneously, less water was transported into the cathode according to the shorter residence time of the oxidant in the humidifier bottle which may have contributed to further lower concentration polarization. Thus the high air flows were beneficial to prevent early onset of losses by mass transport.

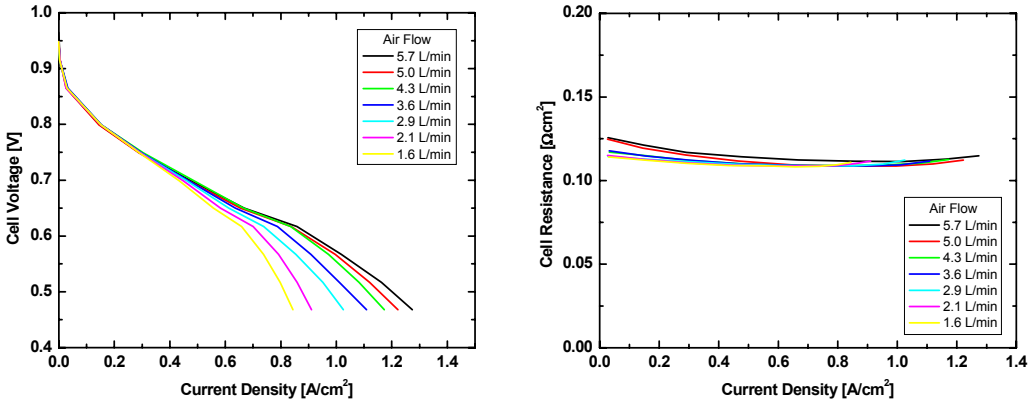

Figure B17: Polarization and HFR measurements of total cell for various constant air flows.

HFR changes accompanied the observed performance changes. The high air flows increased HFR values in the kinetic region below 200 mA/cm^2. At 5.7 L/min oxidant flow, the HFR value was 0.126 Ωcm^2, significantly higher than 0.115 Ωcm^2 recorded for 3.6 L/min. Resistances generally decreased downstream, at high flows down to 0.111 Ωcm^2, at low flows to 108 Ωcm^2, respectively. Although the high air flow rates slightly decreased membrane hydration, no apparent impact on kinetic cell performance occurred. Internal hydration recovered membrane hydration at medium and high current densities.

It was expected, that the influence of the air flow on cell performance would alter with the position along the flow-field and operating point. **Figure B18** shows the current distribution and HFR values of the measurements at 0.8 V. In general, cell performance first increased from Seg01 – Seg03 and then dropped significantly between Seg03 - Seg10. As previously discussed, the cell operated 263 hours prior to the measurements and the decrease in performance was attributed to the possible ripening of the carbon supported platinum catalyst. However, the decay of the segment performance increased with increasing air flow rate. Hence, segment Seg01 performed best at the highest and worst at the lowest cathode flow rate. At segment Seg05 all segments performed identical, while at the cell outlet , i.e. Seg10, the trend of Seg01 was reversed, and the strongest performance was measured for the lowest flow and vice versa.

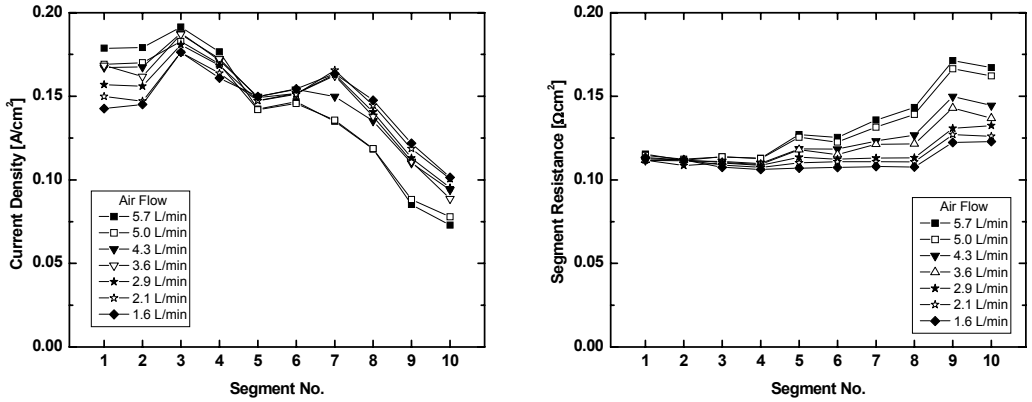

Figure B18: Current density and HFR distribution of segmented cell at 0.8 V after 263 hours of operation for various constant air flows.

Air flows above 2.9 L/min caused the recorded HFR values to increase along the flow-field, an unexpected observation. Increasing the cathode flow pronounced this trend, i.e. the segments downstream became less hydrated. Internal hydration was small in the kinetic region and hydration of the cell was mostly provided from the humidified gas streams. Since water saturation of the gas decreased with increasing flow rates, cathode humidification became less optimized at high flow rates. The cell reacted to an increase in cathode flow identical than to decreasing the cathode humidifier temperature as previously discussed. Once more, insufficient cathode humidification, this time due to high cathode flow rates, resulted in increasing anode catalyst layer resistances.

The measurements emphasized that proper humidification was essential during all possible applied flow rates. For operation at very high flow rates the applied hydration system would need reconsideration. Increasing the residence time of the gas in the Nafion tube by lengthening it, or switching the gas flow to several inlets with individual Nafion tubes, or even increasing the reservoir size to a larger gas exchange volume in the bottle may help to improve the humidification system of the segmented cell to compensate for high gas flows. Higher cathode humidifier temperatures may additionally support cell hydration.

Figure B19 shows current density distribution and HFR values of the same set of measurements at 0.5 V. Throughout the flow-field segment performance increased with increasing flow rate. At 2.9 - 5.7 L/min air flow, the segment current densities increased along the flow-field up to segment Seg06, at lower flow rates up to segment Seg04 respectively. Then they started to decrease to the outlet segment Seg10. Performance dropped about 400 mA/cm^2 from the strongest to the weakest performing segment. At all applied flows segment performance first benefited from reaction water production along the flow-field and then paid a penalty due to it.

Internal hydration kept sufficient amounts of reaction water in the membrane to achieve low HFR values at all flow rates. Just outlet HFR values of segments Seg08 - Seg10 were slightly increased at the highest flow rates. Once more the highest flows resulted in the highest HFR values, but the previously observed effect was suppressed by internal hydration of the membrane due to the high current densities at all segments.

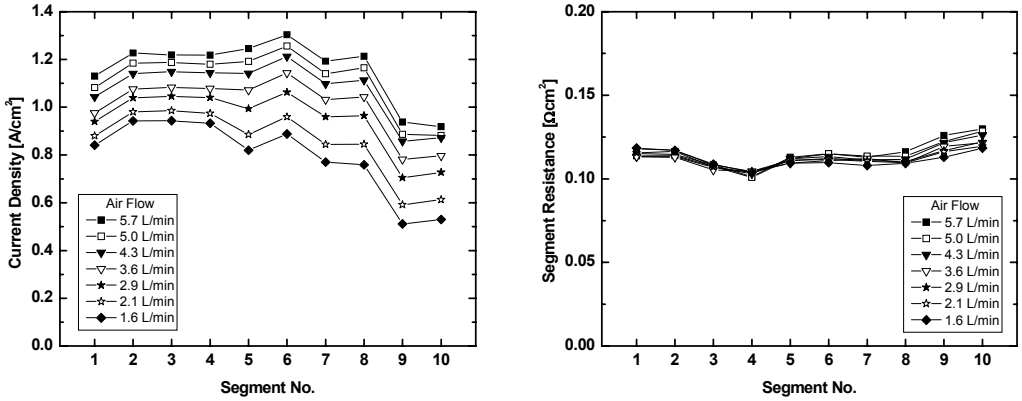

Figure B19: Current density and HFR distribution of segmented cell at 0.5 V after 263 hours of operation for various constant air flows.

Internal hydration showed a very strong contribution towards achieving constant cell humidification at high current densities. Although beneficial at high current densities, high air flows were detrimental for operation in the kinetic region of the fuel cell.

B.4. Conclusions

Spatial fuel cell measurements were performed and discussed employing the developed segmented cell approach. Break-in measurements revealed that the time needed for initial start up of a fuel cell hydration was accelerated with the amount of water present. The expected resistance changes in the catalyst layers could not be observed *in situ*, they were negligible with respect to total cell resistance.

Variation of anode and cathode humidification parameters showed strong impact on local cell performance and resistance. Both anode and cathode hydration interacted, and cannot be separated easily. It appeared necessary to optimize both parameters with respect to each other, the cell temperature and the chosen operating point or range of operating points. The segmented cell allowed furthermore insight in processes which would be very difficult to detect with single cell technology. A long term operated test cell suggested that the magnitude of ripening of a fuel cell catalyst depended on its exposure to water.

Variation of hydrogen stoichiometric flow rates showed little impact on performance distribution. The performance changes were caused by changing humidification of the

gas stream at increased anode flow rates. High cathode flow rates changed the performance distribution in the kinetic region and in the region of concentration polarization. Performance drops were observed that were identical to those of an improperly humidified cell. At low current densities the cell failed to compensate for the decreasing saturation of the gas at large flow rates. This resulted in dehydration of the anode catalyst along the flow-field. High cathode flow rates also decreased mass transport limitations of the cell.

Counter-flow measurements with the segmented system refuted predictions in the literature that this configuration was capable to better preserve water within the cell. The reversal of the flow was found to be a very valuable instrument to separate and identify anode and cathode effects and improved insight into fuel cell processes.

References

[B1] A.P. Saab, F.H. Garzon, T.A. Zawodzinski, '*Determination of Ionic and Electronic Resistivities in Carbon/Polyelectrolyte Fuel-Cell Composite Electrodes*', Journal of the Electrochemical Society, **149** (12), A1541-A1546, (2002).

[B2] T.A. Zawodzinski, C. Derouin, S. Radzinski, R.J. Sherman, V.T. Smith, T.E. Springer, S. Gottesfeld, *'Water Uptake by and Transport Through Nafion 117 Membranes'*, Journal of Electrochemical Society, **140** (4), 1041-1047, (1993).

[B3] K.D. Kreuer, '*On the development of proton conducting materials for technological applications*', Solid State Ionics, **97**, 11-12 (1997).

[B4] A.P. Saab, F.H. Garzon, T.A. Zawodzinski, '*The Effects of Processing Conditions and Chemical Composition on Electronic and Ionic Resistivities of Fuel Cell Electrode Composites*', Journal of the Electrochemical Society, **150** (2), A214-A218, (2003).

[B5] T.Q. Rockward, '*Break-In Process of Polymer Electrolyte Fuel Cells*', to be submitted

[B6] L. Wang, A. Husar, T. Zhou, H. Liu, '*A parametric study of PEM fuel cell performances*', International Journal of Hydrogen Energy, **28**, 1263-1272, (2003).

[B7] N. Rajalakshmi, P. Shridhar, K.S. Dhathathreyan, '*Identification and characterization of parameters for external humidification used in polymer electrolyte membrane fuel cells*', Journal of Power Sources, **109**, 452-457, (2002).

[B8] T. Susai, M. Kaneko, K. Nakato, T. Isono, A. Hamada, Y. Miyake, '*Optimization of proton exchange membranes and the humidifying conditions to improve cell performance for polymer electrolyte fuel cells*', International Journal of Hydrogen Energy, **26**, 631-637, (2001).

[B9] T.J.P. Freire, E.R. Gonzalez, '*Effect of membrane characteristics and humidification conditions on the impedance response of polymer electrolyte fuel cells*', Journal of Electroanalytical Chemistry, **503**, 57-68, (2001).

[B10] M. Ciureanu, R. Roberge, '*Electrochemical Impedance Study of PEM Fuel Cells. Experimental Diagnostics and Modeling of Air Cathodes*', Journal of Physical Chemistry B, **105**, 3531-3539, (2001).

[B11] P. Sridhar, R. Perumal, N. Rajalakshmi, M. Raja, K.S. Dhathathreyan, '*Humidification studies on polymer electrolyte membrane fuel cell*', Journal of Power Sources, **101**, 72-78, (2001).

[B12] D. Hyun, J. Kim, '*Study of external humidification method in proton exchange membrane fuel cell*', Journal of Power Sources, **126**, 98-103, (2004).

[B13] F. Liu, B. Yi, D. Xing, J. Yu, Z. Hou, Y. Fu, '*Development of novel self-humidifying membranes for fuel cells*', Journal of Power Sources, **124**, 81-89, (2003).

[B14] S-H. Kwak, T-H. Yang, C-S. Kim, K.H. Yoon, '*The effect of platinum loading in the self-humidifying polymer electrolyte membrane on water uptake*', Journal of Power Sources, **118**, 200-204, (2003).

[B15] M.S. Wilson, U.S. patent 5952119.

[B16] S. Cleghorn, C.R. Derouin, M.S. Wilson, and S. Gottesfeld, '*A printed circuit board approach to measuring current distribution in a fuel cell*', Journal of Applied Electrochemistry, **28**, 663-672, (1998).

[B17] P. Berg, K. Promislow, J.St. Pierre, J. Stumper, B. Wetton, '*Water Management in PEM Fuel Cells*', Journal of the Electrochemical Society, **151** (3), A341-A353, (2004).

[B18] J.A.S. Bett, K. Kinoshita, P. Stonehart, '*Crystallite Growth of Platinum Dispersed on Graphitized Carbon Black – II. Effect of Liquid Environment*', Journal of Catalysis, **41**, 124-133, (1976).

[B19] M.S. Wilson, F.H. Garzon, K.E. Sickafus, S. Gottesfeld, '*Surface Area Loss of Supported Platinum in Polymer Electrolyte Fuel Cells*', Journal of the Electrochemical Society, **140** (10), 2872-2877, (1993).

[B20] T.E. Springer, T. Rockward, T.A. Zawodzinski, S.Gottesfeld, '*Model for Polymer Electrolyte Fuel Cell Operation on Reformate Feed - Effects of CO, H_2 Dilution, and High Fuel Utilization*', Journal of The Electrochemical Society, **148** (1), A11-A23, (2001).

APPENDIX C

C. Time-dependent Segmented PEFC Model with CO Pulsed Feed Stream (by T. E. Springer)

This is a preliminary report issued as Guido Bender finishes his work at Los Alamos. Our models need to be driven by experiment. At this point we can see several effects in his data that are not represented in the current model. These probably are due to humidity effects on downstream performance of cathode and anode. If further segmented cell experiments are to be carried out, the model discrepancies with observed data may suggest areas for further research.

C.1. Introduction

Previously we have modeled a steady-state PEFC anode that could predict fuel cell performance with reformate gases, high utilization of hydrogen, and CO poisoning [C1]. This was a complete fuel cell model, as we showed that the cathode could not be separated from the anode. The details of the cathode portion of the model were summarized in a user-supplied "standard" cathode performance curve of cell voltage vs. current density if neat hydrogen at 1 atm were used on the anode. Using this artifice implied that the cathode stream was well mixed and of high stoich so that the oxygen concentration was independent of position along the flow path. The model was isothermal, one-dimensional, but tracked the shift in concentration of hydrogen, CO, and inert gases along the flow path. Saturated water vapor was assumed present. The 1-D model included the anode gas diffusion layer (GDL), anode catalyst layer (CL) and the membrane/cathode. This last part was the user-supplied "standard" cathode potential. The boundary conditions were the anode feed stream component partial pressures at the flow channel/GDL interface and the total cell voltage. Equations described partial pressures of hydrogen and CO through both the GDL and the CL, and described the potential through the CL. The local current density and fuel flux were determined to be self-consistent with the cell potential.

This same model was applied repetitively along the flow channel and the local current density dropped along the flow channel as the H_2 concentration dropped, but the total cell voltage remained constant along the flow channel. The fuel cell utilization of hydrogen/CO is an input to this steady-state model. A priori, we do not know the feed rate necessary to achieve this utilization. By tracking utilization rather than position down the flow channel, we can determine the local current everywhere. When the local utilization u' has risen from 0 to the desired value u (say 0.9), the fractional position w along the flow channel must be at w = 1. From [C1] the following relation can be used to

determine the feed rate f_{in} in current density units (i.e. molar flow rate per unit cell area times 2F).

$$\frac{1}{\left(x_H^{IN}+x_C^{IN}\right)f_{IN}}\int_0^1 dw=\frac{1}{\left(x_H^{IN}+x_C^{IN}\right)f_{IN}}=\int_0^u\frac{du'}{I_H+I_C} \tag{1}$$

Once the feed rate was known the total current density could be calculated from the relation

$$I_{ave}(u)=(x_H^{IN}+x_C^{IN})f_{IN}(u)u \tag{2}$$

The feed rate is a function of the desired utilization and will be higher if u is lower. Likewise I_{ave} will be higher if u is lower.

We now desire a time dependent model to model the variation in concentrations and local current density following a shift in inlet CO concentration. A priori for this model we have to specify the inlet feed rate and inlet fuel gas component partial pressures. We cannot use utilization u' but must use fractional position w as the flow channel variable. However we can pick an initial steady state utilization and using the previously discussed steady state model integrate along the flow channel with respect to u' to get the feed rate. Then we reintegrate with respect to w to get the initial partial pressure distribution of H_2 and CO along the flow channel.

Time dependent elements of the model will cause a shift in the distribution of component compositions and local current density from their steady state values for a given set of inputs to the fuel cell system (feed rate, composition and cell load). The dynamic response is affected by various storage elements in the fuel cell such as the fractional coverage of hydrogen and CO on the anode (θ_H and θ_C), the storage of fuel reactants in the cathode and anode GDL, the anode and cathode double layer capacitance, the flow channel volume. The response time of θ_C turns out to be so much slower than the other storage elements that equilibrium with the input conditions can be assumed for the other storage elements.

Let us examine the time response expected for each of these portions of the model.

Fractional CO anode coverage. Assume a hydrogen stoich of 1.25 and 100 ppm CO at 2 atm. All compositions will be reduced by 0.7663 if saturated water vapor is present. Assume the catalyst site density is 0.04 C/cm^2 (mol/cm^2 x F) and the current density is 0.5 A/cm^2 before the addition of CO. At that flow rate the time to fill all the sites with CO is 640 s whereas it is only 0.064 s for hydrogen. Thus an equilibrium equation can be used to relate hydrogen adsorption/desorption.

GDL dynamics. The gas diffusion layer characteristic cathode diffusion time is

$$t_{dif}=\frac{\ell_B{}^2}{D_{ON}}=\tau\frac{P_A\ell_B{}^2}{D_{SON}}\left(\frac{T_S}{T}\right)^{1.823}\approx\frac{7\cdot2\cdot0.018^2}{0.4}\left(\frac{273}{353}\right)^{1.823}=0.071\,s \tag{3}$$

Here D_{ON} is the oxygen-nitrogen binary diffusion coefficient at laboratory conditions and D_{SON} at standard conditions. T and T_S correct the temperature shift from standard

conditions. The anode time is faster. Thus we can neglect any dynamics in both the anode and cathode GDL.

Double layer capacitance. The cathode double layer capacitance will typically be larger than that of the anode because the H^+ or H_3O^+ ions will be attracted to the negative cathode interface and repelled from the positive anode interface, thus shortening or lengthening the capacitor thickness. In the following table the second and third columns give the cathode potential and the corresponding double layer capacitance measured previously [C2]. Using a "standard" cathode potential and a membrane resistance of 0.15 $\Omega\,cm^2$ measured for the segmented cell, we calculated the current density, Col. 1, the differential resistance R_{dif}, $\Omega\,cm^2$, and the double layer charging time constant in seconds $\tau = R_{dif}\,C_{dl}$. We see the time constant is again negligible compared to the CO storage time.

$R_{mem} = 0.15$				
i $[A/cm^2]$	V_{cath} [V]	C_{dl} $[mF/cm^2]$	R_{dif} $[\Omega\,cm^2]$	τ [s]
0.1387	0.8100	8.1900	0.2514	0.0021
0.2501	0.7700	7.6800	0.1793	0.0014
0.4456	0.7100	9.8300	0.1420	0.0014
0.6896	0.6400	16.5000	0.1379	0.0023
0.9471	0.5600	18.4000	0.2083	0.0038
1.1285	0.4800	16.8000	0.4314	0.0072

C.2. Dynamic Model

Figure C1 is a picture of the model with the anode at the bottom and the cathode at the top. We will discuss first the equations describing the total flow and CO concentration along the flow channel, the fluxes through the GDL, the CO and hydrogen adsorption on the catalyst sites, and the local voltage and generated current.

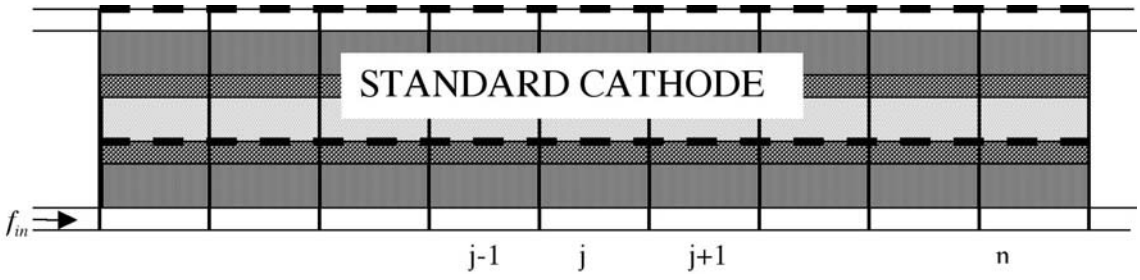

Figure C1: Model schematic showing computational blocks or nodes, j.

Assumptions:

Constant temperature, ideal gas
No pressure drop,
Perfect mixing across flow channel,
Only components are CO, H_2, and saturated water vapor,
Total inlet flow rate f_{IN} is constant. $x_{CO\ IN}$ may change with time
Hydrogen and CO compete for the same sites

var.	**definition**	**unit**
D_{SIJ}	binary gas diffusion coef. for components i and j at STP	cm^2/s
f	H_2+ CO molar channel flow per unit cell area times 2F	A/cm^2
f_{HA}	H_2 flow/area times 2F through GDL to be adsorbed in CL	A/cm^2
f_{CA}	CO flow/area times F through GDL to be adsorbed in CL	A/cm^2
h	thickness of flow channel	cm
$j_H\ j_C$	local current density source from H, CO	A/cm^2
ℓ_B	GDL thickness	cm
P_a	total pressure	atm
T_K	Cell Temperature	K
V_m	molar volume at STP - 22400	cm^3/mol
w	fractional distance along flow channel	-
x_1	dry hydrogen mole fraction	-
x_2	dry CO mole fraction = 1-x_1	-
x_w	mole fraction of water vapor	-
y	fractional distance through GDL	-
θ_H	fractional H coverage	-
θ_C	fractional CO coverage	-
ρ	molar site density x F	C/cm^2

Flow Channel. Subscript H refers to hydrogen, subscript C to CO. The molar flow is expressed in terms of the maximum current density that flow rate could produce. Thus f_H is the current density that 1 stoich hydrogen flow rate per unit cell area would produce. The molar continuity of CO and H_2 + CO along the flow channel requires:

$$2FC_0h(1-x_w)\frac{\partial x_C}{\partial t}+\frac{\partial(x_C f)}{\partial w}+f_{CA}=0,\ \text{where}\ C_0=\frac{P_a\cdot 273}{V_m\cdot T_K}. \tag{4}$$

$$\frac{\partial f}{\partial w}+f_{HA}+f_{CA}=0 \tag{5}$$

The quantity $h(1-x_w)$ is the volume per cell area available per unit cell area for the CO and hydrogen.

Gas Diffusion Layer. The Stefan-Maxwell equations allow us to determine the CO mole fraction in the catalyst layer as a function of the H_2 and CO flows through the GDL given the diffusion coefficients. This is discussed in [C1], Eq. 12-14 where now we have only H_2, CO, and water vapor. These equations account for water vapor being dragged through the hydrophobic part of the backing with the hydrogen and CO.

$$x_H=1-x_w-x_C \tag{6}$$

$$\frac{\partial x_C}{\partial y}=\alpha_{CH}\left(x_C f_{HA}-(1-x_w-x_C)f_{CA}\right)+\alpha_{Cw}\left(x_C f_w-x_w f_{CA}\right);\ \alpha_{ij}=\frac{\mathrm{V_S}\tau T\ell_B}{\varepsilon T_S D_{Sij}} \tag{7}$$

$$\frac{\partial x_w}{\partial z}=0;\quad f_w=x_w\left(\alpha_{Hw}f_{HA}+\alpha_{Cw}f_{CA}\right)/(\alpha_{Hw}(1-x_w-x_C)+\alpha_{Cw}x_C) \tag{8}$$

Three constants independent of operating conditions for the backing are needed in the equations for the CO concentration drop across the GDL.

$$k_{B1}=\alpha_{HC}-\alpha_{Cw}x_w;\ k_{B2}=\alpha_{HC}+\alpha_{Cw}x_w/(1-x_w);\ \mathrm{k_{B3}}=\alpha_{HC}+\alpha_{Cw}{}^2x_w/(1-x_w)/\alpha_{Hw} \tag{9}$$

Equation 7 may be solved to obtain x_{Ccat} where y=1 in terms of x_C in the flow channel where y=0 and the GDL fluxes f_{HA} and f_{CA}.

$$x_{Ccat}=\frac{-k_{B1}f_{CA}+e^{k_{B4}}\left(k_{B1}f_{CA}+x_C k_{B4}\right)}{k_{B4}};\ k_{B4}=k_{B2}f_{HA}+k_{B3}f_{CA}. \tag{10}$$

Catalyst Layer Kinetics

The following kinetic equations are found in [C1]. Hydrogen and CO are adsorbed on the catalyst sites and then electron transfer occurs

$$j_H=2k_{eh}\theta_H\sinh\left(\frac{V_a+V_{Nernst}}{b_h}\right),\ j_C=2k_{ec}\theta_C e^{\frac{V_a+V_{Nernst}}{b_c}} \tag{11}$$

$$\rho\frac{\partial\theta_H}{\partial t}=\mathrm{k_{fh}}x_H P_A\left(1-\theta_H-\theta_C\right)^2-b_{fh}\,\mathrm{k_{fh}}\theta_H^2-j_H \tag{12}$$

$$\rho\frac{\partial\theta_C}{\partial t}=k_{fc}x_C P_A\left(1-\theta_H-\theta_C\right)-b_{fc}k_{fc}\theta_C-j_C/2 \tag{13}$$

We initially tried to use both Eqs. 12 and 13 to track the quantity of hydrogen and CO adsorbed on the catalyst sites. However, this led to convergence problems in the

solution method described below. When we realized that, because the hydrogen concentration is so high, θ_H may be considered always in equilibrium and the right hand side of Eq. 12 may be set to zero. This sets the value of θ_H given θ_C and the anode potential V_a.

$$k_1 = k_{eh}\sinh\left(\frac{V_a + V_{Nernst}}{b_h}\right) + k_{fh}P_h(1-\theta_C);\ k_2 = k_{fh}(P_h - b_{fh})$$
$$\theta_H = \frac{k_1 - \sqrt{k_1^{\,2} - k_2 k_{fh} P_h (1-\theta_C)^2}}{k_2} \qquad (14)$$

Use of Eq. 14 in place of Eq. 12 allowed the computation to converge.

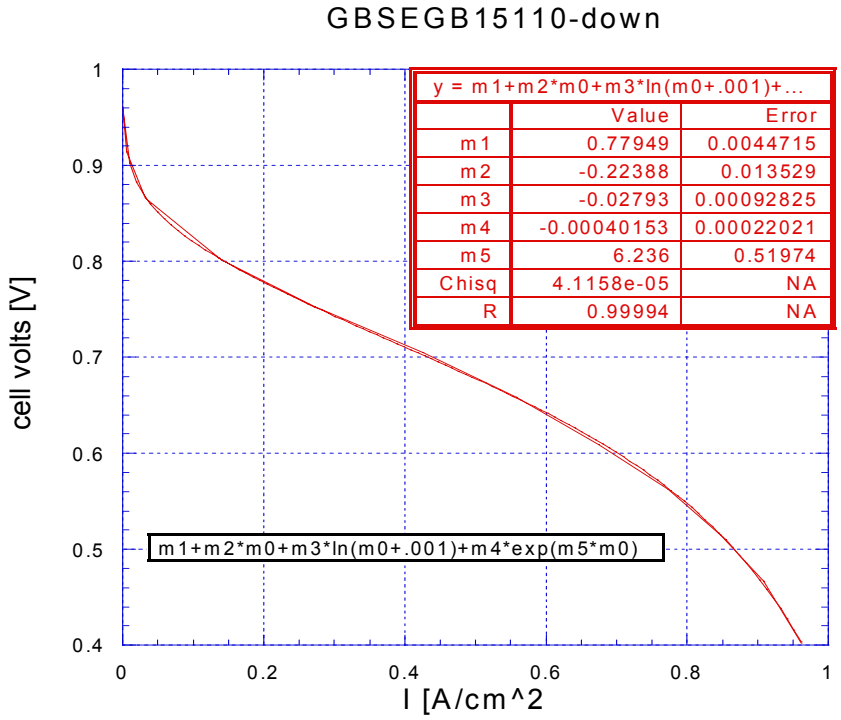

Figure C2: Standard cathode potential including fit and its variables.

C.3. Solution Method

The segmented PEFC model can be used under constant cell voltage V_{cell} or under constant cell current I_{cell} conditions as the CO inlet concentration varies through time. The model equations for the two conditions are slightly different. Figure C1 depicts the model with hydrogen entering the lower left channel with equivalent current density flow f_{in}. Above the anode flow we have the anode GDL and catalyst layer. The remaining membrane separator, cathode CL ,GDL, and flow field are enclosed in dashed lines and are represented as a "Standard Cathode", as was done in [C1]. This is essentially the VI or polarization curve corrected for anode loss for the cell when the anode is operated on neat hydrogen. The model assumption is that the cathode performance will maintain the same voltage-current relationship when the anode is poisoned. This function $V_{std}(I)$ is shown with its fitted equation in **Figure C2**.

The cell is divided into *nj* blocks along the flow path. We write a set of *ni* non linear implicit equations for each block in terms of the problem variables c_{ij}. In each block we have a flow channel with incoming total flow f_{j-1}, outgoing flow f_j, and component flows f_{HA} and f_{CA} through the GDL to the catalyst. We also have the CO mole fraction at the exit of each block both in the flow channel and at the center in the catalyst layer.

Of the previous equations 4 through14, Eqs. 4, 12 and 13 contain derivatives with respect to time. We have replaced Eq. 13 with an algebraic equation for θ_H. Equations 4 and 5 contain derivatives with respect to w, the fractional position down the flow channel. Because they are so thin, no coupling along the flow channel direction occurs in the catalyst layer and GDL, only in the flow channel. We have already solved the spatial equation across the GDL (Eq. 7, 10). Derivatives with respect to w along the flow channel may be expressed as difference equations between variables in the j^{th} and the $(j-1)^{th}$ blocks. Derivatives with respect to time use the Crank-Nicholson scheme. Let θ be such a variable. At each time step variables with time derivatives are incremented from their values the previous time step by the average of the derivative at the old and the new step multiplied by the time increment. That is:

$$\theta^{new} = \theta^{old} + \frac{1}{2}\left(\left.\frac{d\theta}{dt}\right|^{old} + \left.\frac{d\theta}{dt}\right|^{new} \right)\Delta t \qquad (15)$$

Table C1: Model variables and equations in constant voltage mode

i	c_{ij}	Equation $g_{ij} = 0$
1	x_C at flow path block output	$\theta_H(c_{2,j}) =$ Eq. 13. $f_{HA} = 2k_{eh}\theta_H \sinh\left(\left(c_{3,j} + V_{Nernst}\right)/b_h\right)/nj$ $f_{CA} = \left(k_{fc}(1-x_w)P_A\left(1-c_{2,j}-\theta_H\right)c_{5,j} - b_{fc}k_{fc}c_{2,j}\right)/nj$ $\Delta x_{C,j} = (c_{4,j-1}c_{1,j-1} - c_{4,j}c_{1,j} - f_{CA})\Delta t \cdot nj/\rho$ $g_{1,j} = c_{1,j} - c_{1,j}^{old} - (\Delta x_{C\,j} + \Delta x_{C\,j}^{old})/2 = 0$
2	θ_C in catalyst layer	$\Delta\theta_{C\,j} = \left(f_{CA} - j_C/n_j\right)\Delta t \cdot nj/\rho$ $g_{2,j} = c_{2,j} - c_{2,j}^{old} - (\Delta\theta_{C\,j} + \Delta\theta_{C\,j}^{old})/2 = 0$
3	V_a anode kinetics	$g_{3,j} = c_{3,j} + V_{cell} - V_{std}(j_H + j_C) = 0$
4	f flow outlet of block	$g_{4,j} = c_{4,j-1} - c_{4,j} - f_{HA} - f_{CA}$
5	x_C in catalyst layer	$k_{B4} = k_{B2}f_{HA} + k_{B3}f_{CA}$ $g_{5,j} = k_{B4}c_{5,j} + k_{B1}f_{CA} - e^{k_{B4}}\left(k_{B1}f_{CA} + k_{B2}c_{1,j}f_{HA} + k_{B3}c_{1,j}f_{CA}\right) = 0$

Table C2: Model variables and equations in constant current mode

i	c_{ij}	Equation $g_{ij} = 0$
1	x_C at flow path block output	$\theta_H(c_{2,j}) =$ Eq. 13. $f_{HA} = j_H/nj = 2k_{eh}\theta_H \sinh\left(\left(c_{3,j} + V_{Nernst}\right)/b_h\right)/nj$ $f_{CA} = \left(k_{fc}(1-x_w)P_A\left(1-c_{2,j}-\theta_H\right)(c_{1,j-1}+c_{1,j})/2 - b_{fc}k_{fc}c_{2,j}\right)/nj$ $j_C = 2k_{ec}c_{c,j}\exp((c_{3,j} + V_{Nernst})/b_c$ $\Delta x_{C,j} = (c_{4,j-1}c_{1,j-1} - c_{4,j}c_{1,j} - f_{CA})\Delta t \cdot nj/\rho$ $g_{1,j} = c_{1,j} - c_{1,j}^{old} - (\Delta x_{C\,j} + \Delta x_{C\,j}^{old})/2 = 0$
2	θ_C in catalyst layer	$\Delta\theta_{C\,j} = \left(f_{CA} - j_C/n_j\right)\Delta t \cdot n_j/\rho$ $g_{2,j} = c_{2,j} - c_{2,j}^{old} - (\Delta\theta_{C\,j} + \Delta\theta_{C\,j}^{old})/2 = 0$
3	V_a anode kinetics	$g_{3,j} = c_{3,j} + c_{6,j} - V_{std}(j_H + j_C) = 0$
4	f flow outlet of block	$g_{4,j} = c_{4,j-1} - c_{4,j} - f_{HA} - f_{CA} = 0$
5	Accumulated current from exit	$g_{5,j} = c_{5,j} - c_{5,j+1} - \left(j_H + j_C\right)/nj = 0$
6	V_{cell} is uniform	$g_{6,1} = c_{5,1} - I_{cell} = 0$ Total cell current = cumulated current $g_{6,j-1} - g_{6,j} = 0$ Each V_{cell} equals its neighbor's V_{cell}

Table C1 shows the five variables and the five corresponding implicit equations in each block that must be solved simultaneously for constant V_{cell}. This mode allows the CO concentration shift across the GDL to be included. We found it to be negligibly small, and dropped it in the constant current mode as it caused calculation instabilities. In the constant I_{cell} mode we added two variables (6 in all), one to accumulate the current in each block, which was forced to equal I_{cell}; the other to pass the uniform, but time varying V_{cell} to each block. **Table C2** shows the equations for this latter mode.

C.4. Modeled and Experimental Results

At this time all experiments on the segmented cell have been performed under constant voltage conditions. The segmented cell operating conditions for comparing model to experiment here are: P_A=2.78 atm, T_{cell}=353K, V_{cell}=0.6 V. After 1 minute of a 1.1 stoich flow of water saturated neat hydrogen, 100 ppm CO is added to the feed stream for 315 minutes, then removed. We will look separately at the poisoning and the recovery time segments. The model assumes the same cell parameters along the flow channel except for component concentrations and local current density. Because the experimental cell showed some differences in individual segments, the effective area of each segment was adjusted to give the same experimental current density for neat hydrogen as the observed average current density. As the model contains 40 nodes for greater spatial resolution, the current was combined in blocks of 4 to compare to the 10 experimental segments. Likewise the user supplied "standard cathode potential" is determined separately from experimental data with neat hydrogen on the 10 segments. Ten separate sets of 5 coefficients (see Figure C2) were fitted and used for the 40 nodes in blocks of 4.

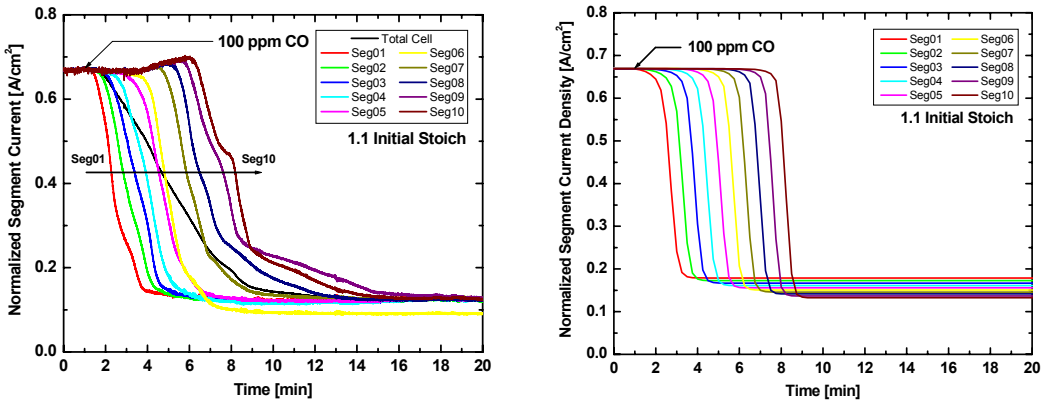

Figure C3: Experimental and modeled current density of 10 segments as function of time.

Figure C3 shows a comparison of experimental and modeled results. The measured currents take longer time to drop as the modeled currents. Likewise the cathode performance appears to improve as upstream poisoning occurs, an effect not represented in the model as yet. The model shows the current density to decrease more further along the flow channel because of increased CO concentration due to hydrogen consumption. If oxygen is allowed to diffuse across the cell, the current density with poisoning can be made to increase along the channel. This oxygen diffusion will also lengthen the step response time between the first and last segments. Further study is required before incorporating this effect in the model.

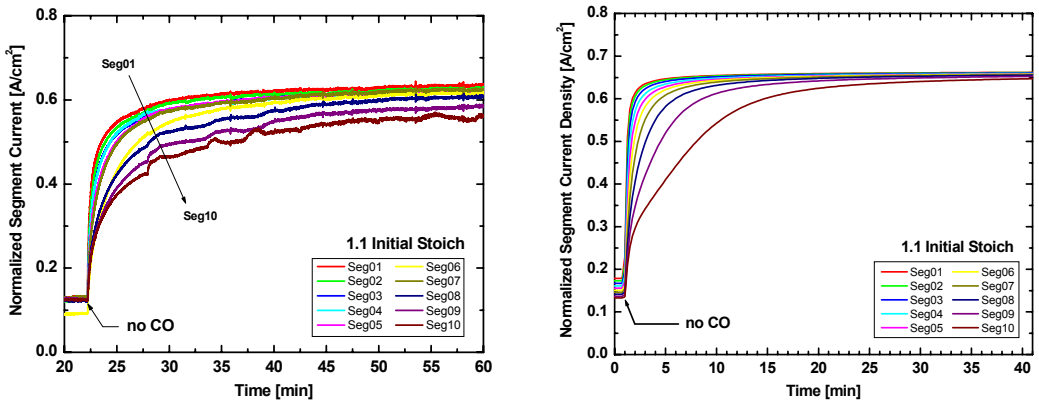

Figure C4: Measured and modeled current response following removal of CO from the feed stream.

Figure C4 shows the measured and modeled current recovery following removal of CO from the feed stream. The difference in recovery time between segment 1 and 10 in the model and during the experiment is similar, but we observed experimentally that recovery remained incomplete. The origin of this effect needs to be identified. Some of the internal variables in the model are shown in **Figure C5**. Although we have had no constant current experiments, **Figure C6** shows the same set of variables with the experiment run at a constant current density of 0.25 A/cm^2 instead of a constant voltage of 0.6 V. This mode forces the anode voltage to go much higher in the poisoning interval.

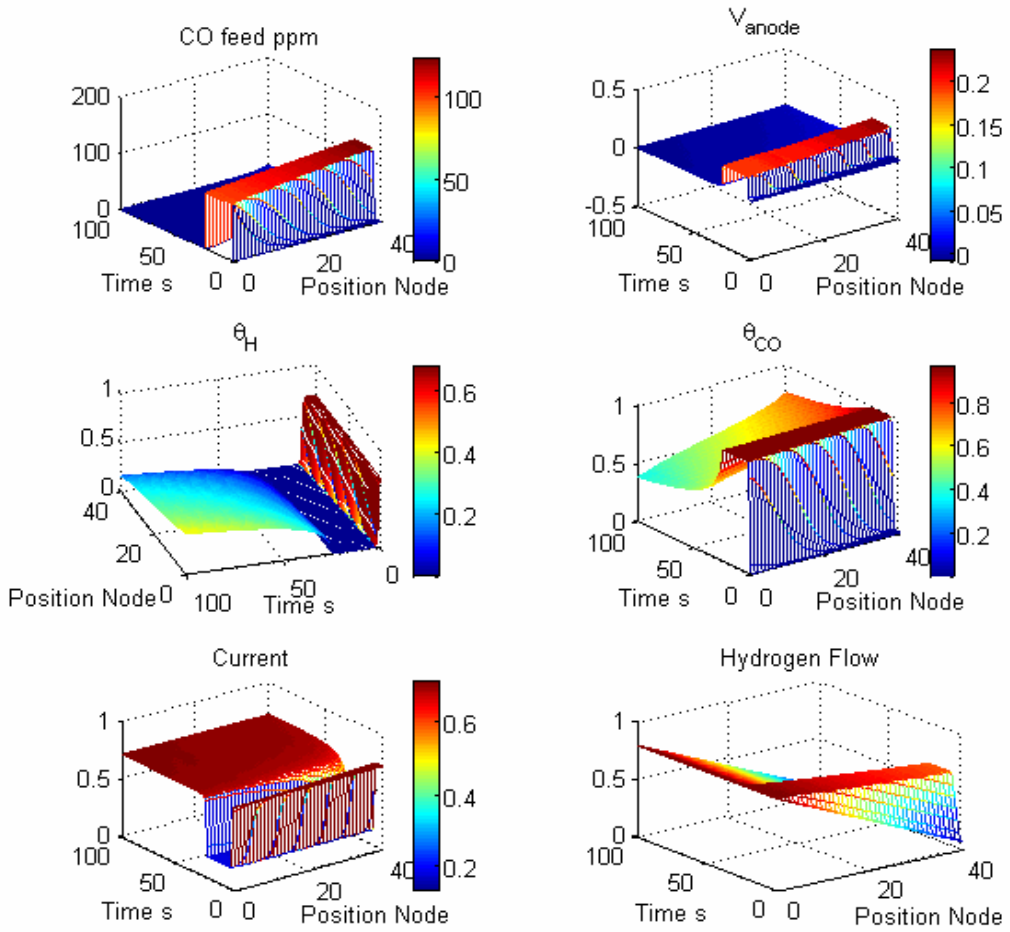

Figure C5: **Various model variables are shown as a function of the 40 node positions and time for the case shown in Figures 3 and 4. The model variables are CO mole fraction along the flow channel, anode voltage, fractional coverage of hydrogen and CO, local current density and local hydrogen flow down the flow channel.**

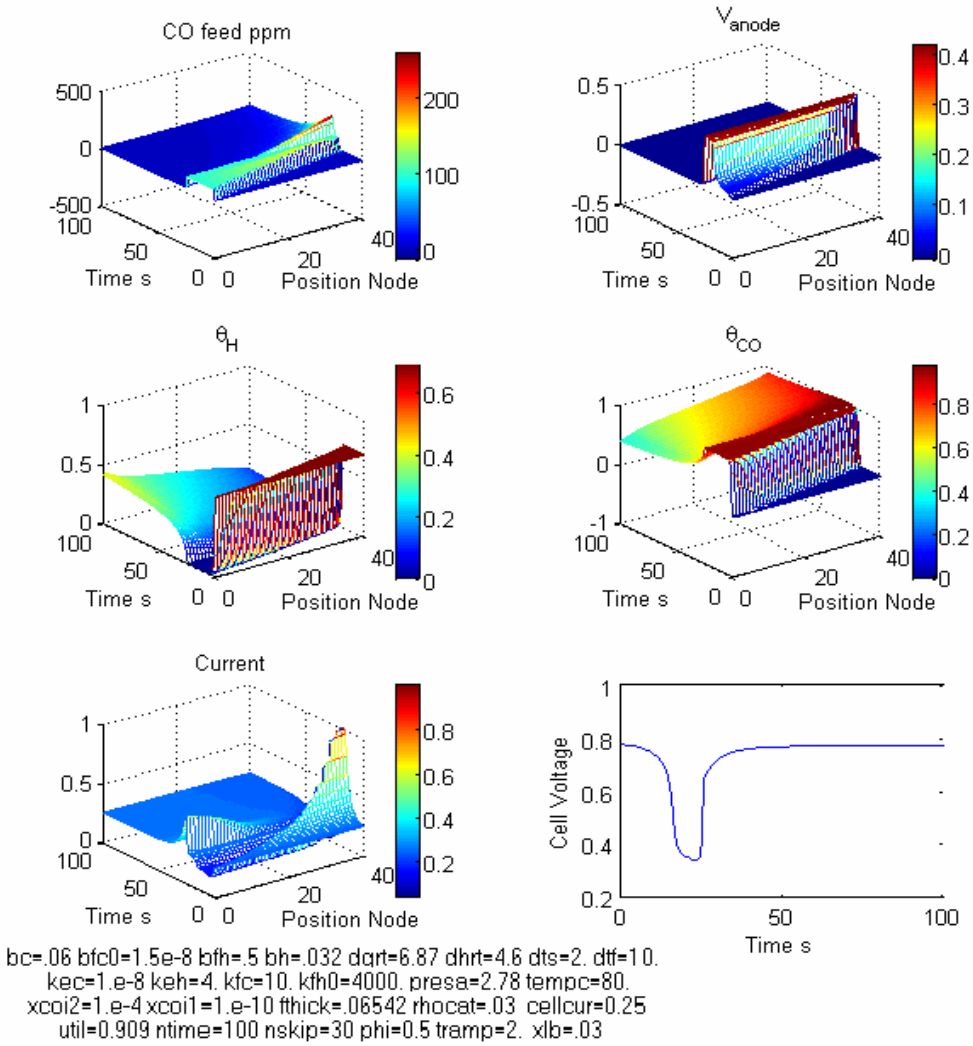

Figure C6: Same conditions as for the model in Figures 3 to 5 but at a constant current of 0.25 A/cm^2 instead of a constant voltage of 0.6 V.

C.5. Conclusion

This has been a quick review of the present model of the time response of a segmented PEM fuel cell following CO injection. Comparison of model with G. Bender's experiments have and can suggest possible future areas of model improvement and of new experiments.

References

[C1] Springer, et al, J. Electrochem. Soc. **148**, A11-23 (2001)

[C2] Springer, Zawodzinski, Wilson, and Gottesfeld, J. Electrochem. Soc. **143**, 587 (1996)

Acknowledgements

I would like to sincerely thank the institutions as well as the people involved for their support on this work.

Special thanks to: TomZ for dragging me “on board” and providing me with an interesting ever-changing project. Professor Stimming and Professor Wagner for supporting the external PhD adventure and trusting in the choices made oversea. Judith and Tommy, for their friendship, their knowledge and experience, and their smiles. Work will be different without you. Andrew, Bryan, Francisco, the three Johns, Mahlon, and the two Piotrs for countless discussions, scientific exchange and more. Nick and Avinash for keeping me mentally stable during my writing period. I will act in Terminator VII, you’ll see. Marla, for stepping into my life, and last not least my family and the rest of my friends for taking me as I am.